

1-1-2008

Optimization of subharmonic generation from ultrasound contrast agents at high frequency ultrasound

Sara Iradji
Ryerson University

Follow this and additional works at: <http://digitalcommons.ryerson.ca/dissertations>



Part of the [Physics Commons](#)

Recommended Citation

Iradi, Sara, "Optimization of subharmonic generation from ultrasound contrast agents at high frequency ultrasound" (2008). *Theses and dissertations*. Paper 561.

**OPTIMIZATION OF SUBHARMONIC GENERATION FROM
ULTRASOUND CONTRAST AGENTS AT HIGH
FREQUENCY ULTRASOUND**

By

Sara Iradji

**Bachelor of Science, Biomedical Engineering
Azad University of Tehran (Iran), 2001**

A thesis

presented to Ryerson University

in partial fulfillment of the

requirements for the degree of

Master of Science

in the Program of

Biomedical Physics

Toronto, Ontario, Canada, 2008

©Sara Iradji, 2008

Author's Declaration

I hereby declare that I am the sole author of this thesis.

I authorize Ryerson University to lend this thesis to other institutions or individuals for the purpose of scholarly research.

Sara Iradji

I further authorize Ryerson University to reproduce this thesis by photocopying or by other means, in total or in part, at the request of other institutions or individuals for the purpose of scholarly research.

Sara Iradji

OPTIMIZATION OF SUBHARMONIC GENERATION FROM ULTRASOUND CONTRAST AGENTS AT HIGH FREQUENCY ULTRASOUND

Master of Science, Biomedical Physics

Sara Iradji

Ryerson University, 2008

Abstract

The microcirculation can be differentiated from the surrounding tissue using high frequency ultrasound subharmonic imaging. This imaging technique relies on the detection of energy scattered from ultrasound contrast agents at half the transmit frequency due to their resonant oscillations. The current contrast agents and the subharmonic imaging parameters have not been optimized for high frequencies. Moreover, the origin of subharmonic generation from submicron bubbles is not well-understood. The size distribution of Definity™ phospholipid-shelled microbubbles was altered to find the optimal bubble size to be resonant over a wide range of high frequencies. The resonant behaviour of bubbles was investigated through in vitro attenuation measurements. The transmit frequency and pressure were varied to optimize the backscattered subharmonic signal. Alteration of Definity™ population significantly improved the scattering for subharmonic imaging at 20 MHz. A peak negative pressure between 400 to 600 kPa is suggested for this frequency range.

Acknowledgements

I would like to thank my supervisor, Dr. Michael Kolios, for his tremendous amount of support and patience, for his trust and confidence on me and for the great lessons he taught me about life. Many thanks to Dr. David Goertz, for his many suggestions and guidance. I would like to acknowledge the efforts of Arthur Worthington and Dr. Emmanuel Cherin who have aided me in this work. Thanks to Dr. Carl Kumaradas for his helpful advices, to Raffi Karshafian and Andrew Needles for answering my questions, to Dr. Jahan Tavakkoli for his guidance and for being in my exam committee, to everyone in the department of physics who makes these two years beautiful and memorable. I would like to take this opportunity to express my gratitude to Dr. Pedro Goldman, he gave me more courage in the days ahead.

Dedication

To Dr. Pedro Goldman and my family

Table of Contents

Author's Declaration	ii
Abstract.....	iii
Acknowledgements	iv
Dedication	v
Table of Contents	vi
List of Tables	x
List of Figures.....	xi
Chapter 1 Introduction.....	1
1.1 Blood flow in microcirculation	1
1.2 Angiogenesis and tumour microcirculation	3
1.3 Research Motivation	5
1.4 High frequency ultrasound.....	8
1.4.1 Limitations of conventional ultrasound imaging.....	10
1.4.2 Scattering of objects	11
1.4.3 Scattering from Blood	13
1.4.4 Nonlinear Propagation of Ultrasound.....	16
1.5 Ultrasound Contrast Agents	18
1.5.1 Applications of contrast agents in medical ultrasound imaging.....	18
1.5.2 History of ultrasound contrast agents	20
1.5.3 Scattering from ultrasound contrast agents	23
1.5.4 Attenuation	24
1.5.5 Multiple scattering.....	25
1.6 Behaviour of Ultrasound Contrast Agents	26
1.6.1 Linear and Nonlinear Systems.....	27
1.6.2 Linear oscillations of bubbles.....	29

1.6.3 Nonlinear bubble oscillations	31
1.7 Subharmonic imaging	33
1.8 Subharmonic Generation.....	37
1.8.1 Subharmonic threshold.....	37
1.8.2 Three stages of subharmonic generation	38
1.8.3 Transient subharmonic generation.....	39
1.9 Theories behind subharmonic generation	41
1.9.1 Transient cavitation	42
1.9.2 Subharmonic generation from resonating bubbles	43
1.9.3 Resonance of larger bubbles at their second harmonic	44
1.9.4 Surface wave theory	44
1.10 Summary	45
1.11 Hypothesis and objectives	46
1.12 Outline of Thesis	46
Chapter 2 Theory of Bubble Oscillation.....	48
2.1 Introduction	48
2.2 The Rayleigh-Plesset equation	48
2.3 Shell effects	52
2.4 The Minnaert Resonance Frequency.....	55
2.5 Scattering Cross-section	58
2.6 Damping of an Oscillating Bubble.....	60
2.6.1 Radiation Damping.....	61
2.6.2 Thermal Damping.....	61
2.6.3 Viscous Damping	62
2.7 Keller-Miksis Model	63
2.8 Simulation Results.....	64
2.8.1 Limitation of the pulse envelope to detect the subharmonics	66
2.8.2 Effect of bubble size on subharmonic generation	68

2.8.3 Subharmonic as a function of transmit frequency	70
2.8.4 Subharmonic as a function of transmit pressure.....	73
2.9 Validity of Keller-Miksis Model at High Frequency and High Pressure....	75
2.9.1 Validity at high frequency	75
2.9.2 Validity at high pressure.....	75
2.9.3 Validity for a bubble population.....	76
2.10 Summary and Conclusion	77
Chapter 3 Subharmonic Characterization of	
Microbubbles at High Frequencies	79
3.1 Introduction	79
3.2 Materials and Methods	80
3.2.1 Transducer Characterization.....	80
3.2.2 Agent Handling.....	82
3.2.3 Population Alteration.....	83
3.2.4 Size Distribution Measurements.....	84
3.2.5 Attenuation Coefficient Measurements	85
3.2.6 Backscatter Measurements	90
3.2.7 Subharmonic generation under varying transmit conditions.....	94
3.3 Experimental Results.....	95
3.3.1 Size Distribution Measurements.....	95
3.3.2 Attenuation Coefficient Measurements	96
3.3.3 Backscatter Measurements	98
3.3.4 Subharmonic as a function of transmit frequency	99
3.3.5 Subharmonic as a function of transmit pressure at 20 MHz and 40 MHz	
.....	101
3.4 Discussion of Results	104
3.4.1 Attenuation Coefficient Measurements	105
3.4.2 Backscatter Measurements	107

3.4.3 Subharmonic as a function of transmit Frequency	109
3.4.4 Subharmonic as a function of transmit Pressure at 20 MHz and 40 MHz	110
3.5 Summary	113
Chapter 4 Discussion and Future Work	115
4.1 Optimization of Subharmonic Imaging	116
4.2 Future Contrast Agent	117
4.3 In vivo Subharmonic Imaging	119
4.4 Conclusion	120
Appendix A: Equations required for derivation of Keller-Miksis Model	122
Appendix B: Output pressure characterization of the RMV-710B™ and RMV-708™	126
Bibliography	130

List of Tables

Table 1-1 Commercial Ultrasound Contrast Agents (replicated from Szabo 2004)	22
Table 1-2 The values represent the contribution of the densities and bulk moduli terms (Equation 1.4) of various Rayleigh scatterers assuming water as the medium (ρ_0 and K_0) (replicated from Kinsler et al. 1982).....	24

List of Figures

Figure 1-1 Microcirculation looks like a network; Blood velocity increases in the large vessels (replicated from Karchakdjian 2001).	2
Figure 1-2: A Scanning Electron Microscopic (SEM) image of the microvessels of normal tissue and angiogenic vessels. The normal tissue has organized arrangement of arterioles, capillaries and venules (Left). The tumour microvasculature shows an unregulated complex pattern (replicated from McDonald and Choyke 2003).....	5
Figure 1-3 A comparison of ultrasound backscatter coefficients for different tissues over 20 to 100 MHz. At lower frequencies, the backscatter from blood with a low shear rate of 0.16 s^{-1} is higher than that with a high shear rate 32 s^{-1} . At higher frequencies, the differentiation between the backscatter signal of blood and that of other tissues becomes very difficult (replicated from Foster, Pavlin et al. 2000).....	16
Figure 1-4 Harmonics are generated due to the distortion of a sinusoidal pulse. After traveling a certain distance, the waveform becomes saw-tooth and its energy will be absorbed in the medium (replicated from Muir 1980).....	18
Figure 1-5 Different regimes of bubble behaviour as a function of the Mechanical index (replicated from Cobbold 2007).	27
Figure 1-6 At lower amplitude acoustic excitation, a bubble can be compared to a mechanical mass-spring system, which experiences the simple harmonic motion (replicated from Hoff 2001).	30
Figure 1-7 Asymmetrical bubble expansions and contractions make the pressure versus time response of the bubble asymmetric and cause harmonics to appear in the frequency response of bubbles (replicated from Szabo 2004).	33

Figure 1-8 <i>In vivo</i> B-mode imaging of the left ventricle of a mouse heart a) in fundamental at 20 MHz and b) subharmonic at 10 MHz, shows a higher contrast to surrounding tissue ratio (replicated from Goertz et al. 2005).....	35
Figure 1-9 The subharmonic generation from Levovist™ exhibiting the three stages: a) the onset, b) rapid growth and c) saturation. d) shows the subharmonic response versus the transmit pressure (adapted from Shi et al. 1999).....	41
Figure 2-1 The pressures exerted by liquid on the bubble wall at equilibrium is balanced with the internal gas pressure inside the bubble (adapted from Leighton 2007).	49
Figure 2-2 The radial stresses at the inner and outer shell, T1 and T2, respectively. The difference in these stresses is due to the elastic and viscous forces in the shell (replicated from Hoff 2001).....	55
Figure 2-3 The scattering cross section of a bubble and a Rayleigh scatterer as a function of their size when excited at 20MHz (Left) and as a function of the transmit frequency for the scatterers of 1 μm diameter (Right).	60
Figure 2-4 Damping constant versus varying transmit frequency for a 1 μm bubble. At higher frequencies, the radiation damping dominates where the viscous damping becomes less significant (replicated from Hoff 2001).....	63
Figure 2-5 Bubblesim graphical user interface.....	66
Figure 2-6 Subharmonic detection is more challenging using rectangular-enveloped pulses; the arrows show the difference between the energy scattered at the fundamental and half the center frequency of the transmit pulse.....	67
Figure 2-7 Resonance frequency versus bubble diameter. 1.2 and 2 μm bubbles are resonant at 20 MHz and 10MHz, respectively, using Equation 2.24.	69
Figure 2-8 The radial displacements and the power spectra of 1.2 and 2 μm bubbles excited using a 20 MHz rectangular pulse.	69

Figure 2-9 The radial displacements and the power spectra of 1.2 and 2 μm bubbles excited using a 40 MHz rectangular pulse.	70
Figure 2-10 When the subharmonic pressure threshold is exceeded, the bifurcation happens in the radial oscillation of bubble. This threshold is minimum for the 2 μm bubble of 10 MHz resonance frequency, excited at 20 MHz (replicated from Cheung et al. 2007).....	72
Figure 2-11 The simulated ratio of subharmonic to fundamental as a function of the transmit frequency with the transmit pressure of 1.5 MPa which is normalized to the subharmonic to fundamental of the transmit pulse.....	72
Figure 2-12 The simulated amount of subharmonic versus varying transmit pressure at 20 MHz (left) and 40 MHz (right).....	74
Figure 2-13 The simulated subharmonic to fundamental ratio as a function of transmit pressure at 20 MHz (left) and 40 MHz (right) which is normalized to the subharmonic to fundamental of the transmit pulse.....	74
Figure 3-1 In Microtrac™, switching the lasers on, one at a time, multiplies the number of sensors used to detect the scattered light from the sample.	85
Figure 3-2 In this custom-made container for the attenuation measurements, ultrasound beam was reflected off a quartz plate, located at the focus of the transducer.....	87
Figure 3-3 Setup for the attenuation measurements of the bubble suspension. The beam is reflected off the surface of the quartz plate.....	88
Figure 3-4 A typical 20-cycle pulse at 25 MHz, used in all the experiments, in time and frequency domain.	90
Figure 3-5 Setup for the backscatter measurements.	91
Figure 3-6 Schematic of the setup for the backscatter measurements. The beam is focused 2 mm behind the Saran membrane.....	92
Figure 3-7 Display of the Vevo770™ in RF mode during a typical backscatter experiment. The region of interest which was selected in the B-mode image	

(on the top) is shown separately on the bottom left corner. The time (red line) and frequency (blue line) domain representation of each line within the region of interest can be presented in the bottom right graph.	93
Figure 3-8 A typical received spectrum of a native bubble population which is integrated in two frequency bands: subharmonic (0.46 to 0.54 of the transmit frequency) and fundamental (0.96 to 1.04 of the transmit frequency).	95
Figure 3-9 The size distributions of a) native b) 2 μm and c) 1.2 μm filtered populations show a successful removal of the majority of bubbles larger than the filter pore size.	96
Figure 3-10 The narrowband attenuation coefficient measurements of a) native b) 2 μm and c) 1.2 μm filtered populations, using two transducers the RMV-710B and RMV-708. It demonstrates an increase in the resonance frequency (peak of the attenuation coefficient) of each population due to the alteration of bubble populations.	97
Figure 3-11 The averaged power spectra (average of 200 lines) from each of three bubble populations excited at 20 MHz with a 20-cycle rectangular-enveloped pulse of 400 kPa. The power spectra were normalized to the fundamental of each bubble population.	99
Figure 3-12 The normalized subharmonic to fundamental ratio versus varying transmit frequency, using 20-cycle rectangular-enveloped pulses at the peak negative transmit pressure of 400 kPa.	100
Figure 3-13 The absolute values of subharmonic and fundamental energies at 20 MHz and 40 MHz normalized to the lowest fundamental amplitude of each bubble population.	103
Figure 3-14 The normalized ratios of subharmonic to fundamental for each bubble populations at a) 20 MHz and b) 40 MHz.	104

Chapter 1

Introduction

1.1 Blood flow in microcirculation

The mammalian microcirculation is a network, consisting of many arterioles and its major branches, the metarteriols (Figure 1-1). The metarteriols are connected to capillaries through precapillary sphincters. The capillaries, forming an extensive network, are 5 to 10 μ m in diameter and less than 1mm in length. These are located close enough to cells (less than 60-80 μ m) to enable the diffusion of gas and nutrients through the single layer of epithelial cells of their wall. Small venules are formed when these capillaries reach together and then become the collecting venules (Li 2004).

Blood is a suspension of erythrocytes (Red Blood Cells, RBCs), leukocytes (White Blood Cells, WBCs) and thrombocytes (platelets) in plasma. The viscosity of blood is 4.5 to 5 times that of water which changes with shear flow rate (Szabo 2004). The blood flow in the microcirculation depends on the overall function of the organ, containing these microvessels. Reynolds number is used to identify the different flow regimes such as laminar (characterized by smooth, constant fluid motion) with a low Reynolds number and turbulent

(characterized by random eddies, vortices) with a high Reynolds number.

Reynolds number is defined by:

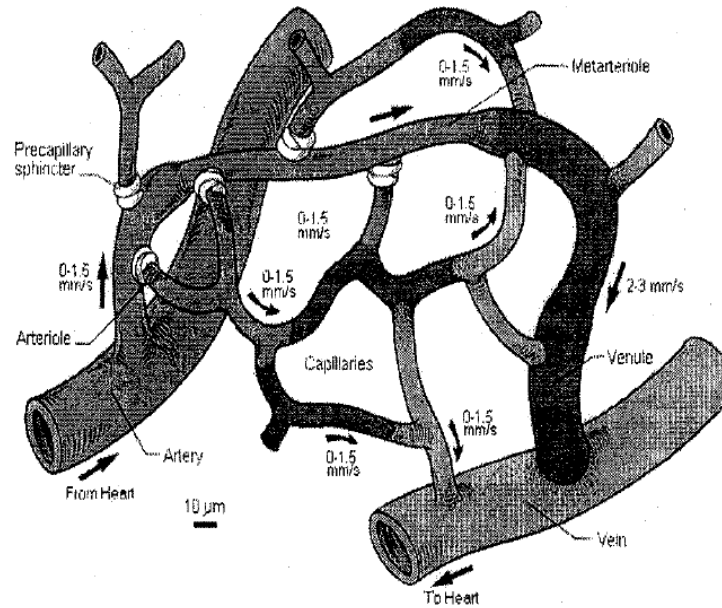


Figure 1-1 Microcirculation looks like a network; Blood velocity increases in the large vessels (replicated from Karchakdjian 2001).

$$R_e = \frac{\rho v d}{\eta} \quad (1.1)$$

ρ , is the density of blood, v , is the mean blood velocity (ms^{-1}), d , is the diameter of the blood vessel (m) and η is the blood viscosity (m^2s^{-1}) (Li 2004). Reynolds number ranges from 0.003 in capillaries compared to 0.03 for a 100 μm arteriole. Blood flow in the microcirculation is assumed to be steady. In order to simplify a

model for veins, they can be modeled as long rigid tubes with a changing diameter in which blood circulates with a steady flow as an incompressible¹ Newtonian fluid². Under these assumptions, the fluid velocity increases by a ratio of the squared radii. Figure 1-1 shows the blood velocities ranges from less than 1mm/s in the capillaries to 20 mm/s in the large vessels (Karchakdjian 2001).

1.2 Angiogenesis and tumour microcirculation

Tumour angiogenesis research has become one of the most attractive areas of clinical oncology since 1980. The term “tumour angiogenesis”, first used by Shubik (Greenblatt and Shubik 1968), means simply the unregulated development of new vasculature. Folkman was the first person who hypothesized that the tumour angiogenesis has a critical role in the development and metastatic spread of tumours. He also believed that tumours can be treated with antiangiogenic drugs (Folkman 1971). Research in treating tumours by blocking tumour

¹ The density of the fluid does not change. Liquids can often be modeled as incompressible fluids, whereas gases cannot.

² For a Newtonian fluid, the viscosity depends only on temperature and pressure (and also the chemical composition of the fluid if the fluid is not a pure substance), not on the forces acting upon it.

angiogenesis or targeting endothelial cells of newly developed vasculature has been a topic of increasing interest (Skalak 2005).

The chaotic growth of tumour vessels can be characterized by abnormal branching, loops, large avascular areas, irregularity in the diameters of tortuous vessels and dead ends (Jain 1988). The microvessel density is high and non uniform in a given microscopic area of tumour growth. The complex pattern of blood flow is temporally and spatially heterogeneous and even oscillating in these newly-developed vessels. This allows the tumour vessels to be distinguished from the vasculature of healthy tissues (Figure 1-2).

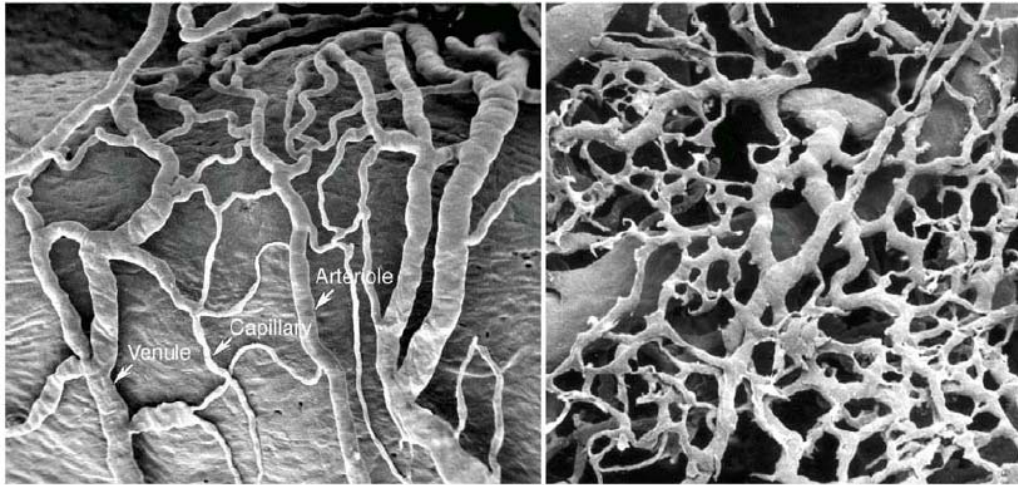


Figure 1-2: A Scanning Electron Microscopic (SEM) image of the microvessels of normal tissue and angiogenic vessels. The normal tissue has organized arrangement of arterioles, capillaries and venules (Left). The tumour microvasculature shows an unregulated complex pattern (replicated from McDonald and Choyke 2003).

1.3 Research Motivation

It is thought that the study of blood flow in tumours can be used to assess the success of tumour treatments. Antiangiogenic and antineovascular therapies target abnormal tumour blood vessels. Changes in the blood flow and volume can be considered as positive clinical responses to therapy. This is a better alternative diagnostic biomarker compared with monitoring the tumour shrinkage as a response to therapy. The reason is that the tumour shrinkage is believed to be a

slower response to the antiangiogenic therapy compared with chemotherapy (Hlatky 2002).

High microvessel density as a result of tumour angiogenesis is a sign of many cancers. This sign is typically found at the surface of the tumour since the center of the tumour can become necrotic as the tumour grows. Therefore, invasive techniques such as taking biopsy samples to monitor the vessels density which requires comparable samples may not be reliable. Imaging modalities such as x-ray computed tomography (CT), magnetic resonance imaging (MRI), positron emission tomography (PET), single photon emission computed tomography (SPECT), ultrasound and near-infrared optical imaging can image the tumour vessels not only noninvasively but also over larger volumes (Miller 2005 and Miles 1999).

MRI is usually limited by the instrument availability and expenses. MRI estimate of hemodynamic data is not quantitative since the signal strength changes nonlinearly with the concentration of MRI contrast agents. Moreover, one of the major problems with MRI contrast agents (for instance, gadolinium GD-DTPA) is that they can pass through the vasculature and leak to surrounding tissues.

CT has the advantage of the best spatial resolution images amongst all the current imaging modalities. Its image intensity changes linearly with the concentration of the contrast agent. However, a high concentration of CT contrast

agent is usually required because of poor sensitivity of CT imaging. A relatively high dose of radiation and CT contrast agents limit the use of this modality because of its associated toxicities (Miller 2005).

PET and SPECT can detect and provide quantitative data using very low concentration of the tracer molecules. However, both techniques have lower resolutions compared with MRI and CT. In addition, PET can only be used at locations, having specialized facilities such as cyclotron and chemical laboratories. The reason is that PET tracers are radionuclides of very short half-life (Rohren 2004 and Miller 2005).

Optical imaging is still new and has not become widely accepted. Orthogonal polarization spectroscopy, one of the optical techniques, uses Indocyanine green that fluoresces at near infrared wavelength to image tumour vessels (Ntziachristos 2000, Cuccia 2003 and Miller 2005). Optical Coherent Tomography (OCT) which can provide a resolution of 1 to 15 μ m but only within a depth of 2 to 3 mm has not become a common imaging modality yet (Huang et al. 1991).

Ultrasound is portable, safe and inexpensive. Its soft tissue contrast which is generally lower than CT and MRI, can be improved using Ultrasound Contrast Agents (UCAs) and new imaging techniques. Ultrasound contrast agents do not leak to the surrounding tissue (unlike MRI contrast agents). These agents are insonified by nonionizing ultrasound beams and they do not cause any toxicity (as

opposed to CT). Ultrasound contrast microbubbles can be labelled with an agent in order to bind to angiogenic markers for molecular imaging of tumour microvasculature (Ellegala 2003).

1.4 High frequency ultrasound

Ultrasound has been widely used as a reliable diagnostic tool since the 1970s. Medical ultrasound imaging is based on the transmission of sound (typically 1-15MHz) into the body and the reception, processing and display of returning echoes from tissues. The clinical popularity of ultrasound is because it provides high resolution images of soft tissues using contrast agents (as well as being real-time, safe, portable and inexpensive). The imaging resolution increases with ultrasound frequency, although there is a trade-off with the depth of penetration.

The use of high frequency ultrasound (10MHz up to 100MHz) to image tissues and cellular microstructures dates back to Sokolov in the 1930s, when he proposed the first acoustic microscope (Sokolov 1935). Imaging living tissue at microscopic resolution (as small as 15 μ m) has a great benefit of noninvasively studying the tissue growth as a function of time. The penetration of ultrasound allows visualization of subsurface planes which are inaccessible to optical

techniques. Three important clinical applications of high frequency B-mode imaging are in ophthalmology at 40- to 60-MHz range (Pavlin et al. 1990; Sherar et al. 1989), dermatology (Hoffmann et al. 1989 and 1990) and intravascular ultrasound at 20-MHz range (Bom et al. 1989, Meyer et al. 1988, Nissen et al. 1990 and Yock et al. 1989).

Research on applications of high frequency ultrasound in the fields of developmental and cancer biology has attracted a great deal of attention. Direct manipulation of mouse embryos *in utero* is now possible with ultrasound guided injection techniques. Moreover, the mouse provides a system for studying mammalian development. Animal studies can provide extensive genetic information. Transgenic and gene targeting techniques also have been developed to manipulate the mouse genome (Foster 2000).

Studying the blood flow in microcirculation is very promising at high frequencies; with a resolution of 50 μm at 50 MHz, the blood flow in the microvessels can be distinguished using color flow imaging (Kruse and Ferrera 2002) and integrated pulsed-wave Doppler (PWD)/color flow imaging (Goertz et al. 2000 and 2002).

1.4.1 Limitations of conventional ultrasound imaging

Ultrasound echocardiography is one of the main applications of ultrasound which can be done using B-mode and Doppler imaging. In B-mode imaging of heart, the goal is to identify the boundaries of blood and the wall of cavities. Identification of the margins of the endocardium in the left ventricle and microvessels of the myocardium has a great clinical importance. However, this identification becomes impossible because the reverberations of ultrasound between the transducer, the chest wall and ribs cause some artefacts³ to appear within the cavity. Ultrasound contrast agents can be used to increase the echoes from the blood above these artefacts. However, the conventional use of contrast agents to enhance the echoes from small blood volumes is not beneficial (for instance, in the myocardial vessels). The reason is that the heart muscle itself produces a strong acoustic backscatter signal. This problem can be overcome by using subharmonic and pulse inversion imaging techniques (Becher and Burns 2000), which is described below.

One of the major limitations of echocardiography using Doppler imaging techniques is that there must be sufficient velocity or signal strength of the blood flow in the vessel to detect the vessels. It means that as the blood flow decreases with the increasing rate of bifurcation in the microvasculature network, the vessels become invisible. Therefore, it produces a lower Doppler shift. If the flow

is fast but the blood volume is small (e.g. in a stenotic jet) or when there is a fast tissue motion around the vessel (e.g. fast motion of myocardium) the Doppler shift can not be detected.

The conventional Doppler imaging with or without using contrast agent relies on using the high pass (wall) filters in order to separate the relative high velocity of blood flow compared to the tissue motion. A new Doppler modality must be developed based on the harmonic imaging techniques such as subharmonic imaging in order to detect the fast movements of the myocardium and its slow microcirculation (Becher and Burns 2000).

1.4.2 Scattering of objects

There are three categories of scattering based on the relative scale of incident ultrasound wavelength, λ , compared to the size of objects: specular, diffusive and diffractive scattering. When the scatterer is much larger than the wavelength, specular scattering occurs in which the wave is reflected due to the acoustic impedance mismatch between the surrounding medium and the object. Acoustic impedance of materials is defined by the product of their density by the speed of sound:

$$Z = \rho.c \quad (1.2)$$

³ Spurious echoes

where Z is the acoustic impedance, c is speed of sound and ρ is the density of the object. The reflected wave is a replica of the incident wave but reduced in amplitude by a reflection factor (RF). The reflection factor can be calculated as follows:

$$RF = \frac{Z_2 - Z_1}{Z_2 + Z_1} \quad (1.3)$$

where Z_1 and Z_2 are the acoustic impedances of the surrounding medium and the scatterer respectively (Szabo 2004).

“Rayleigh” scatterers which are much smaller than the wavelength of incident wave cause diffusive scattering. In this regime, the scattering cross section which is a ratio of the total power scattered divided by the incident intensity is defined by Lord Rayleigh (Rayleigh 1945):

$$\sigma_s = 4\pi a^2 (ka)^4 \left[\left(\frac{K - K_0}{3K} \right)^2 + \frac{1}{3} \left(\frac{\rho - \rho_0}{2\rho + \rho_0} \right)^2 \right] \quad (1.4)$$

where a is the radius of the scatter, $k = 2\pi/\lambda$ is the acoustic wavenumber, ρ and ρ_0 , and K and K_0 are the densities and bulk moduli of the object and the medium respectively. The bulk modulus is defined by:

$$B = -V \frac{dp}{dV} \quad (1.5)$$

where V is the volume of the object, and dp , is the change in pressure from the equilibrium value as a result of volume changes, dV . The reciprocal of the bulk

modulus is termed the “compressibility”. The most compressible materials are gases. The scattering cross section of Rayleigh scatterers increases with the 4th power of transmit frequency and the 6th power of the object diameter.

The last category of scattering regimes is called Mie or diffractive scattering in which the size of objects is comparable to the incident wavelength. This scattering regime results in certain frequencies being scattered preferentially compared to the other frequencies (Szabo 2004). While the mathematical formulation is complex, solutions exist for simple geometries (Falou 2006).

1.4.3 Scattering from Blood

There are about 5×10^6 RBCs ($\sim 95 \mu\text{m}^3$), ~ 6000 WBCs ($\sim 300 \mu\text{m}^3$) and 300,000 platelets ($\sim 15 \mu\text{m}^3$) in one millilitre of human blood. Plasma contains some large-molecular weight proteins. Scattering from blood is demonstrated by the contribution of scattering from RBCs because of small number of WBCs and small scattering volume of platelets compared with the number and volume of RBCs. In mammalian species, the red blood cells are of the same size and less than $10 \mu\text{m}$. The sizes of their capillaries are in the same order of magnitude. RBCs look like discs, concave on the top and bottom and are of about $7 \mu\text{m}$ in diameter and $2 \mu\text{m}$ in thickness. Considering the small size of RBCs compared with the wavelength of clinical ultrasound, they can be modeled as Rayleigh

scatterers with the backscattering proportional to the fourth power of the transmit frequency (Cobbold 2007).

RBCs can aggregate and group as rouleaux, which are long chains of stacked cells. This kind of cell arrangement increases the degree of anisotropy and the directional dependence of backscatter. Furthermore, backscattering is flow dependent (Fontaine and Cloutier 2003). The backscatter was found to be lower in the vena cava than in the aorta in which blood flow is faster (Wang 1997 and Szabo 2004).

Backscattering is a frequency dependent phenomenon. Most tissues have $f^{1.0-2.0}$ frequency dependence (Cobbold 2007). Arterial walls exhibit $f^{1.1}$ to $f^{1.4}$ dependence in the clinical range (Lockwood, Ryan et al. 1991), while the myocardium has an f^3 dependence (Shung and Thieme 1993). In the clinical frequency range, the scattering from disaggregated blood is very weak, -30dB below the scattering signal from soft tissue (Cobbold 2007). At 7.5 and 10 MHz, blood echogenicity is increased as shear rate decreases and consequently, as the blood viscosity increases (Shung et al. 1984 and Sigel et al. 1982). RBCs aggregate at decreasing shear rate, showing $f^{1.2}$ frequency dependence. These rouleaux disperse when increasing the shear rate, showing f^4 frequency dependence for frequencies below 65MHz (Fung 1997, Foster, Pavlin et al. 2000). Cyclic changes of echogenicity during the cardiac cycle were observed by De

Kroon et al. and were related to changes in the shear rate dependent state of RBC aggregation (De Kroon et al. 1991).

At higher frequencies, absorption of blood approaches to that of tissue as the wavelength (40 to 20 μm for 35 to 65 MHz) approaches the dimension of RBCs. Figure 1-3 shows ultrasound backscatter coefficients for a variety of tissues in the 20 to 100 MHz range. High echogenicity of blood at high frequencies causes difficulties in differentiation lumen from arterial wall. Therefore, it complicates imaging the morphology of the arterial wall (Lockwood et al. 1991).

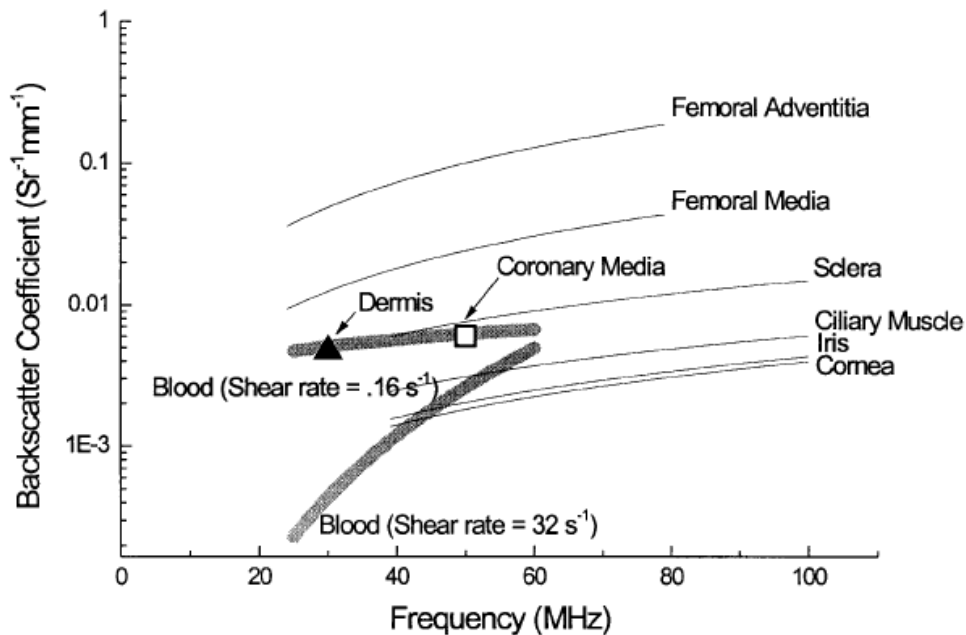


Figure 1-3 A comparison of ultrasound backscatter coefficients for different tissues over 20 to 100 MHz. At lower frequencies, the backscatter from blood with a low shear rate of 0.16 s^{-1} is higher than that with a high shear rate 32 s^{-1} . At higher frequencies, the differentiation between the backscatter signal of blood and that of other tissues becomes very difficult (replicated from Foster, Pavlin et al. 2000).

1.4.4 Nonlinear Propagation of Ultrasound

Ultrasound is a longitudinal wave which propagates in the same direction as the regions of compression (positive pressure) and rarefaction (negative pressure). The linear wave equation assumes a linear propagation of ultrasound with a constant speed of sound in the medium. However, the density and pressure

of the medium only satisfy the linear wave equation⁴ in the limit of very low transmit pressure amplitude. In fact, the speed of sound is not constant and depends on the pressure at each spatial point. Sound travels faster in regions of high pressure and slower in regions of low pressure. Therefore, a continuous sinusoidal wave will be distorted and cause the harmonics of the transmit frequency to propagate in the medium (Figure 1-4). After traveling a certain distance, the waveform becomes saw-tooth, generating even stronger harmonics (Duck 2002).

The interest in harmonic imaging based on the nonlinear propagation of ultrasound has increased since 1996. Images are formed by using the second harmonic of the transmit frequency (Averkiou 1997).

⁴ Any parameter ε , a function of position x and time t , which satisfies $\frac{\partial^2 \varepsilon}{\partial t^2} = c^2 \frac{\partial^2 \varepsilon}{\partial x^2}$ propagates as a wave at a speed c in x -direction.

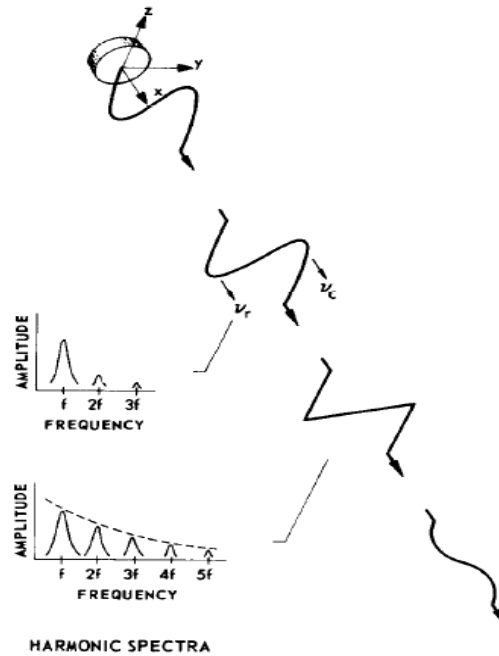


Figure 1-4 Harmonics are generated due to the distortion of a sinusoidal pulse. After traveling a certain distance, the waveform becomes saw-tooth and its energy will be absorbed in the medium (replicated from Muir 1980).

1.5 Ultrasound Contrast Agents

1.5.1 Applications of contrast agents in medical ultrasound imaging

Ultrasound contrast agents are preliminary designed as blood tracers that enhance the backscatter signals in small vessels and tissues at greater depths. At low frequencies, the echoes coming from blood are much weaker than the

scattered sound from the surrounding tissues, typically 30 to 60 dB weaker. Using contrast agents can increase the information content of echoes from underlying blood. Whereas, the intensity of backscattered signals from tissues and blood are the same at higher frequencies (as described in section 1.4.3). Therefore, differentiating between tissues with similar properties and blood is very challenging at higher frequencies. This problem can be overcome by injection of ultrasound contrast agents in vessels (Becher and Burns 2000). Increasing the signal from the blood to surrounding tissue ratio can improve the quality of ultrasound imaging. Studying the motion of blood-filled cavities and blood flow in small vessels and volumes is not feasible without using contrast agents.

In addition, one of the main applications of ultrasound contrast agents is to study blood perfusion or the amount of blood delivered into a local volume of tissue per unit time. Any abnormalities in blood supply to an organ, caused by occluded vessels, can cause a serious disease (Becher and Burns 2000 and Hoff 2001). Recently, developing a new generation of contrast agent, known as targeted agents has been a focus of great attention. The targeted agents contain tiny particles that can bind to pathological tissue in order to enhance and image the echoes coming from these tissues (Lanza 1996 and 1998).

1.5.2 History of ultrasound contrast agents

For the first time, Gramiak and Shah used free air microbubbles to image the aorta. These bubbles which were produced following the injection of saline into aorta had very short lifetime, poor efficacy and safety (Gramiak and Shah 1968). Free air bubbles are the most efficient sound scatterers. However, they can not survive in the body long enough to image the structures. Therefore, an important design goal for microbubbles is to have them persist and not to dissolve quickly. There are two means to stabilize the bubbles: to encapsulate them with shells which prevent dissolution of the gas across the gas-liquid interface; to fill the bubbles with a gas of higher molecular weight with low solubility and diffusivity (Szabo 2004). The encapsulated agents have been developed since 1980. Carroll et al. imaged tumours in the rabbit thigh using encapsulated nitrogen bubbles in gelatine. However, these bubbles were too large for the intravenous administration (Carroll et al. 1980).

Current ultrasound contrast agents are microbubbles filled with gas and shelled with a biodegradable material (Table 1-1). The shell is made of protein, lipid or a polymer. These agents are injected intravenously and they are small enough to mimic the size of red blood cells in order to pass through the capillaries of lungs and microvessels, usually ranging from 1-7 μm . Alunex™ (Mallinckrodt Medical Inc., St. Louis, MO) was developed as the first commercial encapsulated agent with the comparable size to the diameter of a red blood cell.

These air bubbles were encapsulated by the human serum albumin. They could survive passage through the vessels and were made based on Feinstein's work in 1984 (Feinstein et al. 1984). Echovist™ (Schering AG, Berlin, Germany) was the first contrast agent which was approved by the health care authorities in 1991. Levovist™ which is a suspension of Galactose microparticles in sterile water was made by the same company.

The second generation of microbubbles are filled with low solubility gases such as perfluorocarbon with a longer life time. A typical amount of gas injected clinically is on the order of 20-100 μl (Cosgrove 1998). This gas will diffuse out depending on the solubility of the gas shortly after the injection and be carried along by blood and will be filtered out by lungs. Optison™ (Mallinckrodt Medical Inc., St. Louis, MO) is a perfluoropropane-filled albumin-shelled agent. Echogen™ (Son US Inc. Bothell WA) is filled with dodecafluoropentane and stabilized by a surfactant. More recently, phospholipid-shelled agents have been developed such as Sonovue™ (Bracco Inc., NJ) filled with sulphur hexafluorane. Definity™ (Dupont Inc., Boston MA) is filled with perfluoropropane and shelled with phospholipid shell of three different phospholipids. The mean bubble size of Definity™ is 1.5 μm with a range of 1 μm to 10 μm (>90% of the population is of less than 1 to 2 μm diameter). This agent contains a significant subpopulation of submicron bubbles which make it suitable for imaging at higher frequencies.

Polymer-shelled agents have been recently developed; A study by Wheatley and Forsberg was shown that a polymer-shelled agent (Poly Lactic-co-Glycolic Acid, PLGA) can be manufactured with a narrow size distribution of 1.2 μ m. Using this novel agent, power Doppler images of rabbit kidney were taken *in vivo* (Wheatley et al. 2006). biSpheres™ (Point Biomedical, San Carlos, CA) are thick-shelled bubbles whose inner polymer layer is intended for structure stability and the outer layer is included for biocompatibility. These bubbles are resistant to the acoustic pressure and therefore, they can be used to carry their contents to a specific site. Then high acoustic pressures can be used to disrupt these bubbles for localized drug delivery purposes.

Table 1-1 Commercial Ultrasound Contrast Agents (replicated from Szabo 2004)

Manufacturer	Name	Gas	Shell
Acusphere	AI-700	Decafluorobutane	Polymer
Alliance/Photogen	Imagent	Perfluorohexane	Surfactant
Bracco	Sonovue	Sulfurhexafluoride	Phospholipid
Bracco	BR14	Perfluorocarbon	Phospholipid
Byk-Gulden	BY963	Air	Lipid
BMS	Definity	Octafluoropropane	Liposome
Mallinckrodt	Albunex	Air	Albumin
Amersham	Optison	Octafluoropropane	Albumin
Amersham	Sonazoid	Perfluorocarbon	Lipid
Point Biomedical	CardioSphere	Air	Polymer bilayer
Porter	PESDA	Perfluorocarbon	Albumin
Quadrant	Quantison	Air	Albumin
Schering	Echovist	Air	No
Schering	Levovist	Air	Fatty acid
Schering	Sonavist	Air	Polymer
Sonus (withdrawn)	Echogen	Dodecafluoropentane	Surfactant

1.5.3 Scattering from ultrasound contrast agents

Although the size of bubbles (1-7 μm) is much smaller than the wavelength of ultrasound ($\sim 40\ \mu\text{m}$ at 40 MHz), Rayleigh scattering is not a suitable model to describe a bubble in an acoustic field. Yet it can be used to show that bubbles are extremely strong scatterers. Table 1-2 shows the contribution of densities and bulk moduli of various objects which are modeled as Rayleigh scatterers (Kinsler et al. 1982). The difference in densities of the medium and the object cause the scatterer to undergo a back and forth motion, called dipole scattering. The contribution of the difference between the bulk moduli is greater for gas-filled bubbles than that between the densities. This results in oscillations of bubbles in volume which in turn, radiates the sound in a spherically symmetric pattern known as the monopole scattering. The bubbles can be simply modeled as oscillators which resonate at their natural frequencies. Therefore, bubbles have a resonance peak in their scattering cross section. The Rayleigh model ignores the resonance phenomena and the sound absorption by bubbles. In other words, it can predict only the scattering of bubbles below their resonance frequency. For frequencies above the resonance, the scattering cross section is independent of the transmit frequency (Hoff 2001).

Table 1-2 The values represent the contribution of the densities and bulk moduli terms (Equation 1.4) of various Rayleigh scatterers assuming water as the medium (ρ_0 and K_0) (replicated from Kinsler et al. 1982).

Scatterer	$\left(\frac{K - K_0}{3K}\right)^2$	$\frac{1}{3}\left(\frac{\rho - \rho_0}{2\rho + \rho_0}\right)^2$
Air	2.9×10^7	0.33
Water	0	0
Glass	0.10	0.018

1.5.4 Attenuation

In ultrasound contrast imaging, underlying structures can be obscured due to the shadowing effect of microbubbles. Shadowing is a result of an increase in the attenuation due to the presence of microbubbles. The attenuation in a bubble population is the summation of the absorption and scattering of sound from microbubbles. Absorption is caused by damping mechanisms such as viscous, thermal and radiation damping. Absorption from particles smaller than 10 μm in diameter have been studied experimentally and theoretically and attributed to the size and concentration of microbubbles (Uhlendorf 1994, Soetanto and Chan 2000).

At a very low concentration of contrast agents, each microbubble can be treated as an individual scatterer. In this case, the power of backscattered signal is

proportional to the agent concentration (de Jong et al. 1992). Above a certain concentration the attenuation and multiple scattering (section 1.5.5) effects dominate the backscattered signal. Therefore, the backscattered signal does not change linearly with the bubble concentration (de Jong et al. 1992 and Uhlendorf 1994).

The attenuation coefficient measurement is a basic method to characterize contrast agents. A peak in the attenuation coefficient spectrum is an estimate of the resonance frequency of a bubble population. At their resonance frequency, bubbles oscillate with their maximum amplitude and therefore, scatter most of the sound energy. The position of this peak and the curvature of the attenuation response on the frequency axis depend on the shell properties. In addition, damping of the shell can be calculated from the attenuation spectra (Church 1995). If bubbles are driven below their resonance frequency, attenuation is dominated by absorption. While if the transmit frequency is above the bubble resonance frequency, the attenuation is mostly due to the scattering (Simpson 2001).

1.5.5 Multiple scattering

Multiple scattering can happen in a bubble population when the bubble inter-spacing is not sufficiently large. At high concentration of bubbles, the

distance between bubbles is small so that sound can be rescattered from neighbouring bubbles. Previous studies have examined the multiple scattering in suspensions of free gas bubbles (Commander and Prosperetti 1989; Kargl 2002, Goertz et al. 2007). In recent studies, the previous approaches have been modified in order to include the shell effects (Stride and Saffari 2005; Chan and Zhu 2006). The secondary scattering ratio describes the ratio between the primary and secondary scattering from a single bubble. Ignoring the shell effects and assuming a monodisperse bubble population, the secondary scattering ratio can be calculated as follows:

$$SS_r = \frac{4\pi\sigma N^{2/3}}{(0.554)^2} \quad (1.6)$$

where σ is the scattering cross section in m^{-1} , N is the number of bubbles per unit volume. A secondary ratio of 10% is considered significant (Chin 2001).

1.6 Behaviour of Ultrasound Contrast Agents

The behaviour of ultrasound contrast agents depends on the surrounding medium, the acoustic pressure and the shell characteristics. The Mechanical Index (MI), a standard measure of the acoustic output, is defined as a ratio of the

ultrasound peak negative pressure to the square root of the center frequency of transmit pulses. The relation between contrast agent behaviour and the mechanical index shows the importance of improving acoustic parameters for imaging purposes. Figure 1-5 shows the changes in bubble behaviour as the mechanical index increases (Cobbold 2007).

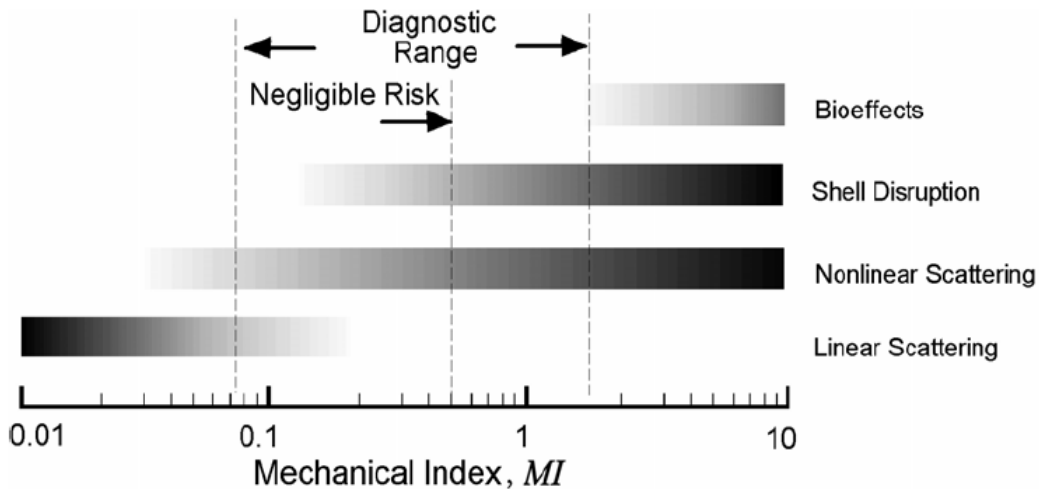


Figure 1-5 Different regimes of bubble behaviour as a function of the Mechanical index (replicated from Cobbold 2007).

1.6.1 Linear and Nonlinear Systems

To understand the linear and nonlinear behaviour of bubble oscillations, a differentiation between linear and nonlinear systems should be considered. For a linear system, the magnitude of the system output is proportional to that of the

system input; so that if input x to the system results in output X , then an input of $2x$ will produce an output of $2X$. A linear system will not produce any frequencies in the output that does not exist in the input. Many actual systems are almost linear in response to small inputs, but become non-linear at higher levels of excitation.

Sometimes a definite threshold exists that only a little above which the input level results in a gross non-linearity. An example of this phenomenon is the “clipping” of an amplifier when its input signal level exceeds the voltage of its power supply. The response of a nonlinear system can be related to the transmit force through a power series expansion:

$$Y(t) = s_0 + s_1.\dot{h}(t) + s_2.\dot{h}^2(t) + s_3.\dot{h}^3(t) + s_4.\dot{h}^4(t) + \dots \quad (1.7)$$

where Y is the general response of the system (e.g. it can represent the bubble wall displacement) and \dot{h} is the transmit force; s_0, s_1 etc. are coefficients. If the system is linear then s_2, s_3 and higher coefficients are zero (Leighton 1994).

The response of a nonlinear system contains new frequency components which do not exist in the input. This response depends not only on the input at those frequencies but also on the input on other frequencies. The magnitude of the response to the input is not proportional to the system input (Hoff 2001).

1.6.2 Linear oscillations of bubbles

If the mechanical index is low, the bubble oscillates in a linear regime and scatters the acoustic energy at the transmit frequency. At lower amplitude acoustic excitation, a bubble can be modeled as a linear oscillator and compared to a mechanical mass-spring system, which experiences simple harmonic motion (Figure 1-6) (de Jong et al. 2002, Hoff 2001). The huge mass of surrounding liquid compared with the negligible mass of gas acts as the mass of system, m . The gas pressure inside the bubble with a high compressibility corresponds to the spring with the spring constant of k . The mechanisms by which the bubble oscillations are damped (details in section 2.6) can be modeled as the damping of the system with a real positive constant of b . The damping force is proportional to the velocity of the surrounding liquid but in the opposite direction to the velocity. In this linear system, the system response is directly proportional to the transmit force, F_{drive} . Applying Newton's Second Law to the system and rearranging the terms give the equation of motion of bubble:

$$m\ddot{\varepsilon} + b\dot{\varepsilon} + k\varepsilon = F_{drive} \quad (1.8)$$

where ε is the small displacement of the bubble wall or the spring from its equilibrium position. The resonance frequency of the system can be found by Equation (1.9) as follows:

$$f_r = \frac{1}{2\pi} \sqrt{\frac{k}{m}} \quad (1.9)$$

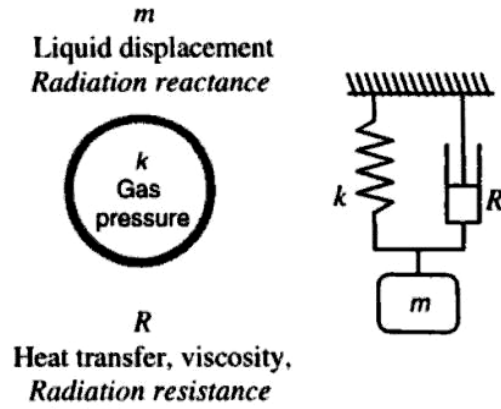


Figure 1-6 At lower amplitude acoustic excitation, a bubble can be compared to a mechanical mass-spring system, which experiences the simple harmonic motion (replicated from Hoff 2001).

The equivalent values for the mass, the damping coefficient and the stiffness has been previously derived as follows (Medwin 1977):

$$m = 4\pi R_0^3 \rho \quad (1.10)$$

$$b = \delta_{tot} \omega m \quad (1.11)$$

$$k = 12\pi\gamma PR_0 \quad (1.12)$$

where ρ is the density of the surrounding medium, δ_{tot} is the total damping, ω is the angular frequency, γ is the heat capacity ratio⁵, and P is the ambient pressure. Therefore, the linear resonance frequency of a free gas bubble can be expressed by:

$$f_r = \frac{1}{2\pi R_0} \sqrt{\frac{3\gamma P}{\rho}} \quad (1.13)$$

This is the frequency at which bubbles can scatter a large amount of energy due to their maximum radial oscillation (known as the Minnaert frequency, details in section 2.4).

1.6.3 Nonlinear bubble oscillations

Bubble oscillation is a nonlinear phenomenon for large mechanical excitations. The bubble can not contract as much as it expands because of the limited compressibility of the gas, entrapped inside the shell. The asymmetrical bubble expansions and contractions make the pressure versus time response of the bubble asymmetric and cause harmonics to appear in the frequency response of bubbles (Figure 1-7). The scattered energies at multiple integers (2, 3 ...) of the transmit frequency are called harmonics (2nd harmonic, 3rd harmonic ...), respectively. The oscillations on integer fractions of the driven frequency, f , are

⁵ The heat capacity ratio or adiabatic index, denoted by γ (gamma), is the ratio of the heat capacity

called subharmonics, $1/2 f$, $1/3 f$, $1/4 f$,... and ultraharmonics, which are the harmonics of the subharmonics: $3/2 f$, $5/3 f$, $2/3 f$,...(Lauterborn 1976). The most well-known subharmonic is the energy at half of the incident frequency.

Considering the physics of nonlinear oscillations, it is possible to establish a relationship between the transmit force (the time-varying transmit acoustic pressure) and the response of the bubble (the bubble wall displacement) which is predicted by the Rayleigh-Plesset equation (Equation (2.11), explained in section 2.2).

at constant pressure (C_p) to the heat capacity at constant volume (C_V).

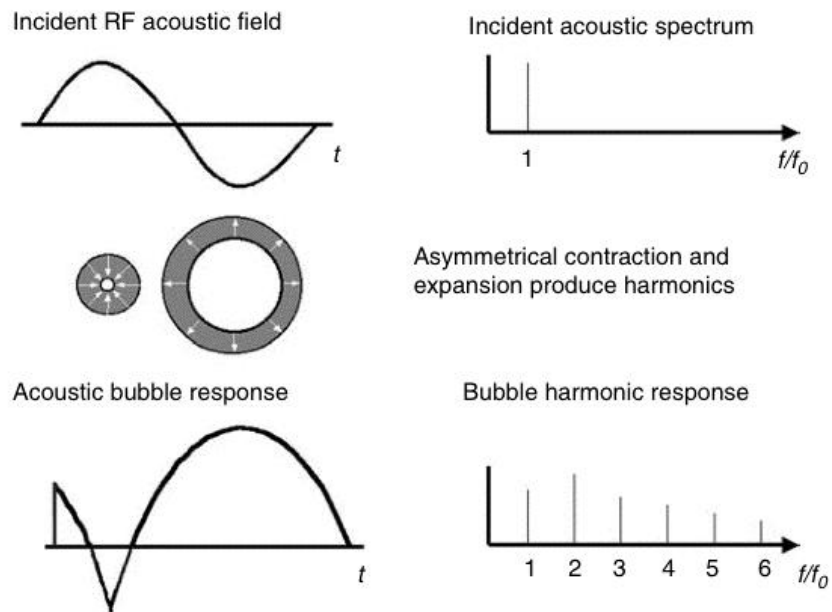


Figure 1-7 Asymmetrical bubble expansions and contractions make the pressure versus time response of the bubble asymmetric and cause harmonics to appear in the frequency response of bubbles (replicated from Szabo 2004).

1.7 Subharmonic imaging

One of the disadvantages of using ultrasound contrast agents with the linear imaging methods is “shadowing”. This occurs because the contrast agent attenuates the signal intensity behind the cavities filled with the agent. Nonlinear imaging techniques with higher sensitivity allow the use of a low concentration of bubbles and, therefore, reduce the effect of shadowing (Uhlendorf and Volkmar

1994). Moreover, when the ratio of blood to tissue volume is small, the contrast obtained with fundamental B-mode imaging using contrast agents is poor (Frinking et al. 2000). For instance, the blood volume ratio for the myocardium is about 10% and using contrast agents with clinical concentrations can only provide a few decibels of enhancement. In this case increasing ultrasound intensity to increase the contrast may cause the bubble destruction and generation of a temporary backscattered signal with no clinical advantage and can cause cardiac arrhythmias (Shi et al. 2000).

The idea behind harmonic imaging is the use of nonlinear scattering from ultrasound contrast agents to generate harmonics of the transmit frequency in order to differentiate between blood and the surrounding tissue. One of major limitations in harmonic imaging is that the second harmonic signal is attenuated more than the fundamental. Moreover, the tissue, itself, produces a significant second harmonic signal due to the nonlinear propagation of ultrasound, as described in the previous section. This reduces the image contrast from the contrast agents (Shankar et al. 1998; Frinking et al. 2000).

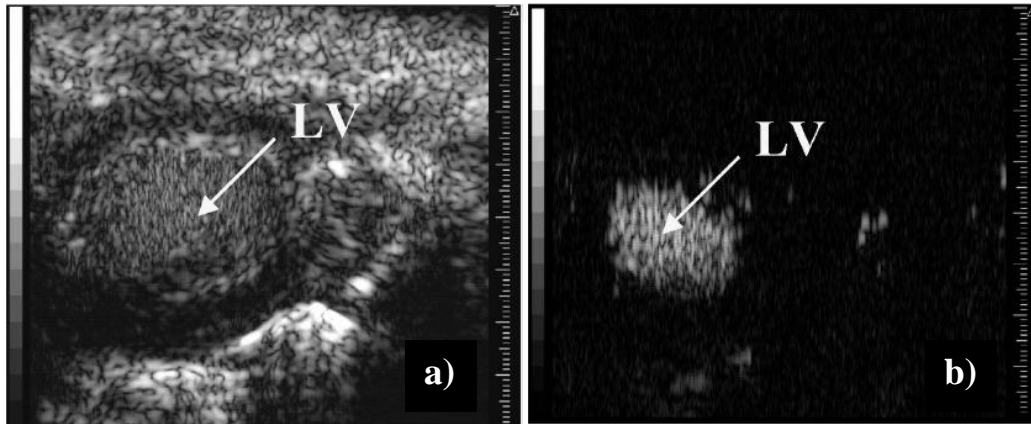


Figure 1-8 *In vivo* B-mode imaging of the left ventricle of a mouse heart a) in fundamental at 20 MHz and b) subharmonic at 10 MHz, shows a higher contrast to surrounding tissue ratio (replicated from Goertz et al. 2005).

Subharmonic imaging has the advantage of higher contrast to surrounding tissue ratio. Subharmonics can not be generated by nonlinear propagation in tissue. Therefore, if microbubbles generate the subharmonic signal, it can be differentiated from tissues. It means that blood and vessels which contain the contrast agent can be detected more easily using this imaging technique. Goertz et al. demonstrated the feasibility of subharmonic imaging to improve the contrast to surrounding tissue ratio, as shown in Figure 1-8 (Goertz et al. 2005). The bubble subharmonics can even exceed the strength of the backscattered tissue echoes at the fundamental. Moreover, since subharmonics are attenuated less than the fundamental and second harmonics, the imaging depth will increase. Although the

transmission of long pulses, required to generate subharmonics, worsens the axial resolution, the contrast enhancement can outweigh this disadvantage (Shankar 1998).

The efficiency of subharmonic imaging technique depends on the transmit parameters, including pressure, bandwidth and frequencies. These parameters have not been optimized for the high frequency range. Investigating the effects of these parameters on the subharmonic signal from microbubbles of various sizes can optimize this imaging technique.

The current commercial ultrasound contrast agents have been designed for use in clinical ultrasound frequencies (up to 10 MHz). It has been shown previously (Goertz 2003) that only a subpopulation of small bubbles resonate at high frequency. Understanding the behaviour of microbubbles can help in developing new contrast agents which are more efficient at high frequency, especially since theoretical models developed have not been able to predict bubble response at higher frequencies.

1.8 Subharmonic Generation

1.8.1 Subharmonic threshold

Subharmonics were first observed by Esche at higher pressure (Esche 1952). Subharmonic generation depends on the transmit conditions as well as the damping in bubble oscillations. The subharmonic needs time and therefore, longer pulses to develop (Shankar 1998). Higher harmonics can be generated for all levels of acoustic excitation. A pressure threshold has to be exceeded for bubbles to emit the subharmonics. This threshold for free gas bubbles was first derived by Eller and Flynn in 1969 and measured experimentally by Neppiras (Neppiras 1968, Eller and Flynn 1969). They found that the subharmonic generation depends also on the transmit frequency. For a free gas bubble, the pressure threshold is minimum at the transmit frequency around twice the resonance frequency of the bubble (Eller and Flynn 1969).

Smaller bubbles and bubbles with thicker shell have higher resonant frequency. Therefore, a higher pressure threshold and frequency is required for these bubbles to initiate the subharmonics. Subharmonic signals from Albunex microbubbles were studied by Chang et al. in 1995 (Chang et al. 1995). Lotsberg et al. found no sharp pressure threshold for Albunex (Lotsberg et al. 1996). Shi studied a surfactant-shelled agent (Shi et al. 1997). Shankar and his coworkers

derived a relationship between physical shell parameters of encapsulated microbubbles and the pressure threshold (Shankar et al. 1999). They also found the subharmonic pressure threshold for shelled bubble to be minimum at twice their resonance frequencies. Definity microbubbles (of 10MHz resonance frequency) are easily driven into subharmonic oscillation when excited at 20MHz (Goertz 2002, Cheung et al. 2008). In all these experiments, the subharmonic threshold was observed at much lower pressure than the theoretical predictions based on the current shell models and damping constants (Shankar et al. 1999).

1.8.2 Three stages of subharmonic generation

The previous studies showed that the subharmonic signal generation can be divided into three stages, depending on the pressure of the incident wave: the onset or occurrence, rapid growth, and saturation (Schrope et al. 1993 and Shi et al. 1999). Figure 1-9 demonstrates the experimental results of subharmonic response of the Levovist™ agent as a function of the transmit pressure (Shi et al. 1999).

The onset stage is where the subharmonic signal is insignificant (Figure 1-9, a). This stage was not observed in the subharmonic response of a free gas bubbles (Eller and Flynn 1968, Neppiras 1968).

The rapid growth occurs when the subharmonic signal grows as the transmit pressure increases and shows a pronounced peak at half the transmit frequency above the noise floor (Figure 1-9, b). The rapid growth stage of subharmonic with pressure was hypothesized to be a promising tool for noninvasive detection of pressure changes in heart cavities and major vessels for early diagnosis of heart and vascular diseases (Shapiro et al. 1990, de Jong 1993b and Brayman 1996).

As the transmit pressure is increased further, the backscattered fundamental increases while the growth of subharmonic becomes slower. This is where the saturation stage happens (Figure 1-9, c).

1.8.3 Transient subharmonic generation

At low mechanical index, the subharmonic emission is stable. The acoustic pressure is low enough for bubbles to maintain a long lifetime, suitable for contrast imaging. If the transmit pressure is increased further, the broadband emission in the received signal will be substantially raised due to the bubble destruction. Therefore, the signal to noise ratio of subharmonic signal is significantly reduced (Shi et al. 1999).

The destruction mechanism is responsible for transient subharmonic emission. Biagi et al. studied the difference between stable and transient

subharmonic emission for an encapsulated microbubble during the destruction event (Biagi et al. 2007). Bubble destruction mechanisms are classified as (Chomas et al. 2001):

- Fragmentation: a shelled microbubble is fragmentized into smaller microbubbles.
- Static diffusion: the gas inside the bubble diffuses from the core of bubble into the surrounding medium.
- Acoustically driven diffusion: the ultrasound driven oscillation increases the rate of gas diffusion.

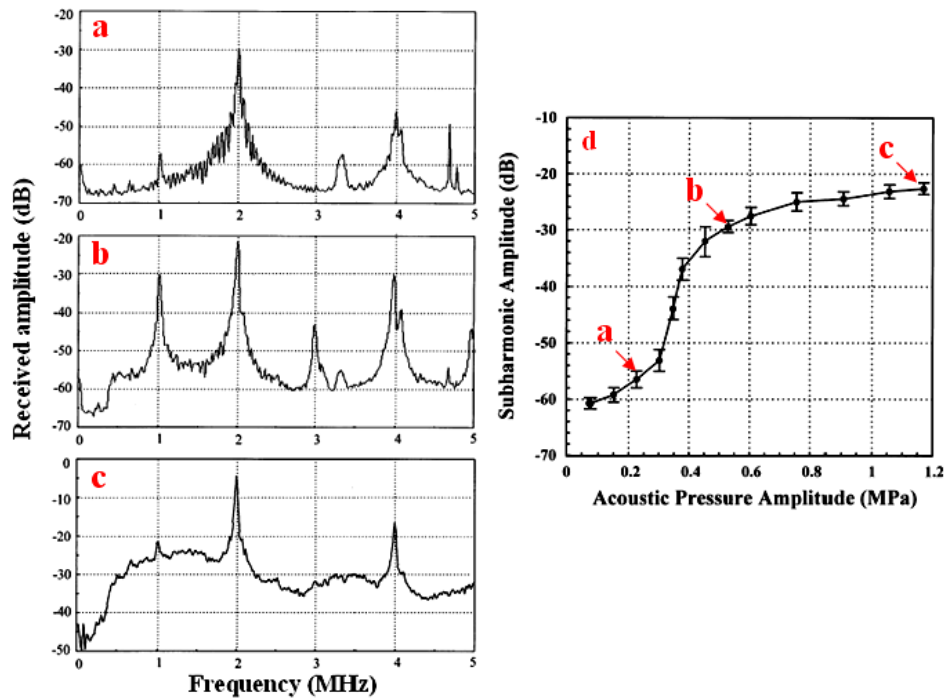


Figure 1-9 The subharmonic generation from Levovist™ exhibiting the three stages: a) the onset, b) rapid growth and c) saturation. d) shows the subharmonic response versus the transmit pressure (adapted from Shi et al. 1999).

1.9 Theories behind subharmonic generation

Subharmonic imaging can be a promising tool to study the microcirculation, although, it is far from an optimized imaging technique. One of the obstacles to optimizing this technique is that the origin of subharmonics has not yet been understood. This fact emphasises a great need to perform

fundamental studies in order to understand the physics of subharmonic oscillations. There exist some theories which try to explain the subharmonic generation as described in the following sections. However, none of them has been proven to be valid over a range of higher frequencies.

1.9.1 Transient cavitation

Transient cavitation is the rapid growth and violent collapse of a bubble which is a threshold event depending on the acoustic pressure and excitation frequency. The shock waves are generated at the collapse of transient cavities and hypothesised to cause the subharmonic generation (Niemczewski 1980). Shock waves are sawtooth waveforms which have frequencies at harmonic multiples of the fundamental. There are some facts that do not support this theory; the experiments with shock waves generated by the sources other than bubble activities did not result in subharmonic oscillations. These observations led to the statement that “the generation of subharmonic is a general characteristic of nonlinear bubble oscillations and does not have to be due to the occurrence of the transient cavitation” (Vaughan and Leeman 1986).

1.9.2 Subharmonic generation from resonating bubbles

Bubbles are most easily driven into nonlinear oscillations when maximal radial displacement happens at their resonance frequency. For a given transmit pressure, the radial oscillation is larger when exciting bubbles below their resonance, compared with when insonifying them above their resonance. However, the off-resonant oscillations are still much smaller than the resonant oscillations (Hoff 2001). Subharmonics and ultraharmonics are developed in a strongly nonlinear system, when bubbles oscillate nonlinearly (Bohn 1957, Walton 1984 and Leighton et al. 1991). As the subharmonic pressure threshold is exceeded, there is a potential for the volumetric pulsations to bifurcate as the oscillations become more chaotic (Lauterborn et al. 1994). The bubble radius displacement reaches two different maxima, one at the transmit frequency and the other one at half of the transmit frequency or the subharmonic. The period doubling is the first step towards a chaotic response (Phelps and Leighton 1997). Subharmonic generation as a result of chaotic response of bubbles was measured experimentally (Lauterborn and Cramer 1981) and the chaos theory was applied to describe this behaviour (Parlitz 1990).

1.9.3 Resonance of larger bubbles at their second harmonic

Subharmonic emission might be due to the activity of the bubbles which are driven at twice their resonance frequency. Eller and Flynn derived an equation for the subharmonic generation of free gas bubbles. This equation predicts a minimum pressure threshold to generate subharmonic from larger bubbles with a natural resonance frequency of half the transmit frequency (Eller and Flynn 1969). This theory was verified experimentally for free gas bubbles at low frequencies (Neppiras 1969). These bubbles are not resonant; however, their backscatter signal might be stronger than that of small resonant bubbles due to their larger size (Leighton et al. 1991).

1.9.4 Surface wave theory

Bubbles can depart from their spherical forms by buoyancy⁶, asymmetries in the environment due to the proximity of other bubbles or boundary walls, gravity, shock waves, and pressure gradients on small scales (compared with the bubble size). As a result of bubble shape oscillations, Faraday waves on the surface of bubbles are generated at half the excitation frequency, first discovered by Faraday (Faraday 1831). Faraday waves are standing waves which are

⁶ the upward force on an object produced by the surrounding medium due to the pressure difference of the fluid between the top and bottom of the bubble

hypothesised to be the origin of subharmonics. However, this hypothesis is blurred by the fact that the observed intensity of subharmonics is stronger than the predicted intensity due to surface waves. The bubbles undergoing the shape oscillation are not good sound scatterers since the velocity potential of surface modes decreases rapidly with the distance from bubbles (Neppiras 1980 and Strasberg 1956). Therefore, only when the bubble approaches close enough to the transducer, subharmonics generated by surface modes can be detected.

1.10 Summary

This chapter presented an introduction on ultrasound scattering and high frequency ultrasound. Current ultrasound contrast agents were introduced and their importance in high frequency ultrasound imaging was explained. Also, the behaviour of these agents was described in linear and nonlinear regimes. The feasibility of subharmonic generation from microbubbles was discussed under various transmit parameters and finally, the theories behind the subharmonic generation was introduced.

1.11 Hypothesis and objectives

The purpose of this work is to optimize the subharmonic signal from Definity™ (lipid-shelled) contrast agents at high frequency. We hypothesized that the alteration of the Definity population is required for more efficient subharmonic generation at high frequency. This alteration causes the majority of the bubble population to have a resonance at the transmit frequency. This may mean that the main source of the subharmonic generation is considered to be either the activity of resonant bubbles excited at their resonance frequency or the resonance of larger bubbles, excited at twice their resonance frequency.

1.12 Outline of Thesis

In this work I investigate the optimization of the subharmonic signal from Definity™ (lipid-shelled) contrast agents at high frequency. Chapter 2 gives an introduction on the theory of bubble oscillations and discusses the theoretical limitations of current microbubble models to predict the optimized transmit parameters at high frequency. Chapter 3 explains the experimental procedures and the results from the attenuation measurements of various Definity™ populations in order to find the resonance frequency as well as the backscatter measurements

to probe the feasibility of optimizing the subharmonic signal. Changes in backscatter signal from the bubbles as a function of incident pressure and frequency are investigated. Chapter 4 discusses the future work in subharmonic imaging and in the development of new contrast agents for high frequency ultrasound imaging.

Chapter 2

Theory of Bubble Oscillation

2.1 Introduction

The nonlinear behaviour of a single bubble in an acoustic field can be predicted by numerically solving a set of differential equations. The purpose of this chapter is to explain the theory of bubble oscillation and to investigate the generation of subharmonic from a single lipid-shelled bubble at high frequencies. This provides a guideline to interpret the experimental results of Chapter 3. The subharmonic signal depends on the transmit conditions. These conditions were varied theoretically to investigate their effects on optimizing the subharmonic signals. The limitations of the current theoretical models to predict the scattered signal from a bubble population at high frequency are highlighted.

2.2 The Rayleigh-Plesset equation

The Rayleigh-Plesset equation, Equation (2.11), is a second order ordinary differential equation which models the radial oscillation of a free air bubble in an

infinite, inviscid⁷ and incompressible⁸ liquid (Rayleigh 1917; Plesset 1949). The bubble diameter is assumed to be much smaller than the incident wavelength. Therefore, the bubble oscillates in a uniform pressure field and remains spherical. The surface tension is neglected. Plesset, Noltingk, Neppiras and Poritsky modified this equation to include the effect of viscosity, surface tension and incident sound wave (Neppiras and Noltingk 1950 and 1951; Poritsky 1952). This equation was further modified to account for damping of the shell (de Jong and Cornet et al. 1994) and acoustic radiation damping (Hoff 2001).

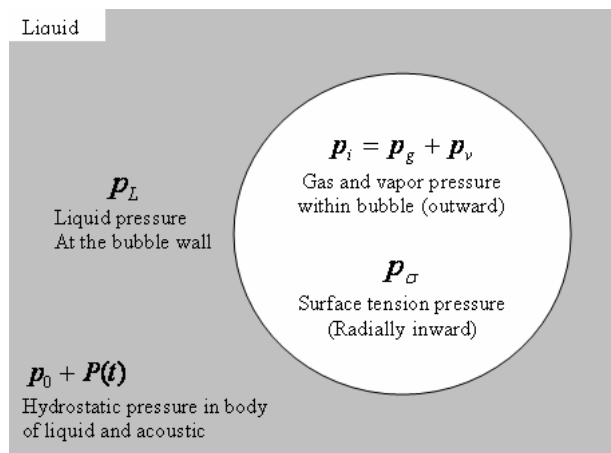


Figure 2-1 The pressures exerted by liquid on the bubble wall at equilibrium is balanced with the internal gas pressure inside the bubble (adapted from Leighton 2007).

⁷ Inviscid liquid is a medium where viscous (friction) forces are small in comparison to inertial forces.

⁸ There is no propagation of sound in an incompressible liquid. The speed of sound is assumed to be infinite.

At time $t > 0$, a bubble of radius R_0 is at equilibrium in an incompressible fluid of density ρ (Figure 2-1). A small-amplitude time-varying acoustic pressure, $P(t)$, is superimposed on the constant hydrostatic pressure, p_0 , so that the liquid pressure far from the bubble is $p_\infty = p_0 + P(t)$. These pressure changes the bubble radius during which the kinetic energy of the liquid is found by integrating the energy over the spherical shell of liquid (of thickness Δr , mass of $4\pi\rho r^2 dr$ and speed of \dot{r}):

$$\frac{1}{2} \rho \int_R^\infty \dot{r}^2 4\pi r^2 dr \quad (2.1)$$

Because the liquid is assumed incompressible, the rate of liquid mass flowing through any spherical surface equicentric with the bubble does not change as a function of time, Δt . Equating the mass of liquid with the radius of r outside the bubble $4\pi r^2 \rho \dot{r} \Delta t$ to the flow at the bubble wall gives:

$$\dot{r} / \dot{R} = R^2 / r^2 \quad (2.2)$$

By substituting Equation (2.2) in Equation (2.1), the kinetic energy is integrated to give $2\pi\rho R^3 \dot{R}^2$. Assuming the bubble oscillation as a simple harmonic motion, this energy is equal to the difference in work done far from the bubble by p_∞ and by the liquid pressure at the surface of the bubble wall p_L :

$$\int_{R_0}^R (p_L - p_\infty) 4\pi R^2 dR = 2\pi\rho R^3 \dot{R}^2 \quad (2.3)$$

Differentiation of Equation (2.3) with respect to R , gives:

$$\frac{p_L - p_\infty}{\rho} = R\ddot{R} + \frac{3\dot{R}^2}{2} \quad (2.4)$$

The internal pressure of the bubble, p_i , is the summation of the gas pressure, p_g , and the pressure of liquid vapour, p_v . This internal pressure at equilibrium is equal to the summation of the pressure of liquid at the surface of the bubble wall, p_L (equal to the hydrostatic pressure, p_0 , when the bubble is at equilibrium) and surface tension, p_σ . The pressure throughout the liquid is assumed to be spatially uniform and equal to p_L . When the bubble radius changes from R to R_0 , assuming the gas obeys a polytropic⁹ law, the gas pressure inside the bubble will be:

$$p_g = p_{g0} \left(\frac{R_0}{R} \right)^{3\kappa} \quad (2.5)$$

where κ is the polytropic constant, p_{g0} is the gas pressure at equilibrium which is obtained by:

$$p_{g0} = p_0 + p_\sigma - p_v \quad (2.6)$$

$$p_i = p_g + p_v = p_L + p_\sigma \quad (2.7)$$

$$p_\sigma = \frac{2\sigma}{R_0} \quad (2.8)$$

$$p_{\infty} = p_0 + p(t) \quad (2.9)$$

$$p_L = \left(p_0 + \frac{2\sigma}{R_0} - p_v \right) \left(\frac{R_0}{R} \right)^{3\kappa} + p_v - \frac{2\sigma}{R} \quad (2.10)$$

Replacing Equations (2.9) and (2.10) in Equation (2.4), the Rayleigh-Plesset equation will be obtained as follows:

$$R\ddot{R} + \frac{3\dot{R}^2}{2} = \frac{1}{\rho} \left\{ \left(p_0 + \frac{2\sigma}{R_0} - p_v \right) \left(\frac{R_0}{R} \right)^{3\kappa} + p_v - \frac{2\sigma}{R} - p_0 - p(t) \right\} \quad (2.11)$$

This equation ignores the effects of viscosity, thermal and radiation damping and assumes radially symmetric oscillation of the microbubble.

2.3 Shell effects

The shell increases the stiffness and viscous damping which in turn, dampens the motion of bubble wall and limits its compressibility. Therefore, it decreases the scattering ability of bubbles and increases the resonance frequency. The Rayleigh-Plesset equation was originally derived for a free air bubble. de

⁹ Polytropic law states that the pressure and volume of a gas are inversely proportional. It is based on the assumption of small amplitude bubble oscillation to maintain the gas pressure uniform inside the bubble.

Jong et al. extended this equation by adding a linear shell of an elastic solid. They tried to model the shell of Albunex™ by introducing the shell elasticity and shell friction (de Jong and Hoff 1993a; de Jong and Cornet 1994). Church assumed an incompressible elastic solid shell model of constant thickness (Church 1995). Modeling of the shell as a viscoelastic solid with a thickness inversely proportional to the bubble diameter which accounts for the shell stiffness and viscosity was first proposed by Hoff et al. (Hoff, Sontum et al. 1996). Frinking et al. suggested a nonlinear model for the contrast agent Quantison™. Based on their work, the shell can be modelled as particles with a constant bulk modulus (Frinking et al. 1998 and 1999).

The shell model used to simulate the bubble oscillations in this chapter, is known as the exponential shell model. This model which is developed by Angelsen et al. can account for the shell softening during the bubble expansions (Angelsen et al. 1999). Figure 2-2 shows the radial stresses at the inner and outer shell, T1 and T2, respectively. The difference in these stresses is due to the elastic and viscous forces in the shell which can be calculated as follows:

$$T2 - T1 = 12 \frac{d_{se}}{R_0} (G_s x_0 (1 - e^{-x/x_0}) + \eta_s e^{-x/x_1} \dot{x}) \quad (2.12)$$

$$x = \frac{R}{R_0} - 1 \quad (2.13)$$

where d_{se} is the steady state thickness of the shell which is considered as a thin uniform viscoelastic solid. G_s and η_s are shear modulus and viscosity, respectively. x , is a ratio between the bubble radius and its equilibrium radius. The shell is assumed to be a linear elastic solid with a varying thickness. Therefore, x_0 and x_l are 0.125 and 0.25, respectively (Hoff 2001).

The estimation of shell parameters can be done experimentally. Most of these experiments were done at low frequencies with low amplitude pulses. Typical shell parameters for Definity™ microbubbles, used in this work, are the shear modulus of 190 MPa, the shell viscosity of 0.07 Pas and the constant shell thickness of 1.5 nm over a frequency range of 10 to 30 MHz (Goertz et al. 2007).

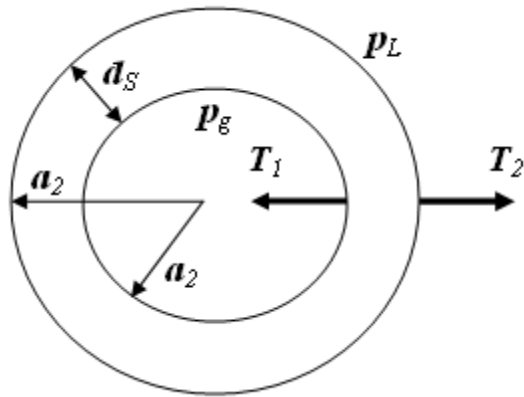


Figure 2-2 The radial stresses at the inner and outer shell, T_1 and T_2 , respectively. The difference in these stresses is due to the elastic and viscous forces in the shell (replicated from Hoff 2001).

2.4 The Minnaert Resonance Frequency

Minnaert found the natural frequency of an oscillating bubble by considering the exchange of energy between the potential and the inertial energies (Minnaert 1933). The bubble radius undergoing a wall motion of $R_\varepsilon = -R_{\varepsilon_0} e^{i\omega_0 t}$ about a mean radius R_0 with the resonance frequency of ω_0 , is:

$$R = R_0 + R_\varepsilon(t) = R_0 - R_{\varepsilon_0} e^{i\omega_0 t} \quad (2.14)$$

It should be noted that an increase in pressure decreases the bubble radius. The kinetic energy of the liquid is obtained by Equation (2.1) which takes its maximum value at the equilibrium position when $R=R_0, |\dot{R}|^2 = (\omega_0 R_{\varepsilon_0})^2$:

$$\Phi_{K,\max} = 2\pi R_0^3 \rho (R_{\varepsilon_0} \omega_0)^2 \quad (2.15)$$

The kinetic energy is zero when the bubble is stationary at maximum displacement where the potential energy of the gas inside the bubble with the pressure of p_g , takes its maximum value:

$$\Phi_{P,\max} = - \int_{R_0}^{R_0 - R_{\varepsilon_0}} (p_g - p_0) 4\pi r^2 dr \quad (2.16)$$

Assuming the gas behaves polytropically, $p_g V^\kappa = \text{constant}$, the pressure and volume conditions at equilibrium are equal to those when the bubble is compressed:

$$p_g (R_0 + R_{\varepsilon})^{3\kappa} = p_0 R_0^{3\kappa} \quad (2.17)$$

$$\frac{p_g}{p_0} = \left(1 + \frac{R_{\varepsilon}}{R_0} \right)^{-3\kappa} \quad (2.18)$$

Substituting binomial expansion of Equation (2.18) into Equation (2.16) with the use to first order of $R_{\varepsilon} = R - R_0$ coordinates gives:

$$\Phi_{P,\max} = \int_0^{R_{\varepsilon_0}} \frac{3\kappa p_0 R_{\varepsilon}}{R_0} 4\pi R_0^2 dR_{\varepsilon} = 6\pi\kappa p_0 R_0 R_{\varepsilon_0}^2 \quad (2.19)$$

Since the model chosen for the oscillation of bubble is simple harmonic motion, the maximum kinetic energy, Equation (2.15), can be equated to the maximum potential energy. Therefore, the linear resonance frequency for the bubble pulsation is:

$$\omega_0 \approx \frac{1}{R_0} \sqrt{\frac{3\kappa p_0}{\rho}} \quad (2.20)$$

which shows that at small amplitude oscillations, the bubble can be modeled as a simple harmonic oscillator. In Minnaert's calculations, the effects of surface tension, viscosity and thermal damping are ignored.

The equation of motion for the linear oscillation of a bubble (as described in section 1.6.2) can be modified to include the shell effects. Equation 1.8 can be rewritten with the following new parameters (replacing the terms in Equations 1.10 and 1.12):

$$m = 4\pi\rho R_0^3 \quad (2.21)$$

$$b = 4\pi R_0 \left(3\kappa p_0 + 12G_s \frac{d_{se}}{R_0} \right) \quad (2.22)$$

$$k = 4\pi R_0 \left(4\eta_L + 12\eta_s \frac{d_{se}}{R_0} \right) \quad (2.23)$$

which η_L is the viscosity of surrounding liquid. Therefore, the linear resonance frequency, f_0 of the shelled-bubble is calculated as follows:

$$f_0 = \frac{\omega_0}{2\pi} = \frac{1}{2\pi R_0} \sqrt{\frac{1}{\rho_L} \left(3\kappa P_0 + 12G_s \frac{d_{se}}{R_0} \right)} \quad (2.24)$$

Without a shell ($d_{se}=0$) and under adiabatic conditions, the Minnaert resonance frequency can be retrieved from Equation 2.20.

For shelled bubbles, the shell dampens the oscillations of the bubble and reduces the amplitude of the scattered signal. The bubble resonance frequency is increased as well.

2.5 Scattering Cross-section

The scattering cross-section σ_s of a bubble is expressed as (Hoff 2001):

$$\sigma_s(a, \omega) = 4\pi R_0^2 \frac{\Omega^4}{(1 - \Omega^2)^2 + (\Omega\delta)^2} \quad (2.25)$$

$$\Omega = \frac{\omega}{\omega_0} \quad (2.26)$$

where R_0 , is the bubble radius at the equilibrium, ω is the angular excitation frequency, δ is the total damping, and Ω is the ratio of the angular excitation frequency and the angular resonance frequency.

It is worthwhile to compare the scattering cross section of Rayleigh scatterers (as described in section 1.4.2) with that of bubbles. Figure 2-3 compares the scattering cross sections of a bubble and a Rayleigh scatterer as a function of the size when excited at 20MHz and also as a function of the transmit frequency for the scatterer of 1 μm diameter. The scattering cross section of the Rayleigh scatterer was calculated for a glass bead with shear modulus of 39000 MPa and density of 2300 kg/m^3 . For the frequencies below the bubble resonance frequency, $\Omega \ll 1$, $\sigma_s = 4\pi R_0^2 \Omega^4$. This is equivalent to the oscillation of bubbles whose diameters are smaller than the resonance diameter and these bubbles behave as Rayleigh scatterers. However, the significant difference between the compressibility and the density of the gas inside the bubble and those of the surrounding medium (usually water) causes the scattering from the bubbles to be much greater than the Rayleigh scatterer. When bubbles are excited above the resonance frequency, $\Omega \gg 1$, σ_s does not depend on the excitation frequency and it increases with R_0^2 . Bubbles scatter more efficiently when excited at their resonance frequency, where their scattering cross section is maximum.

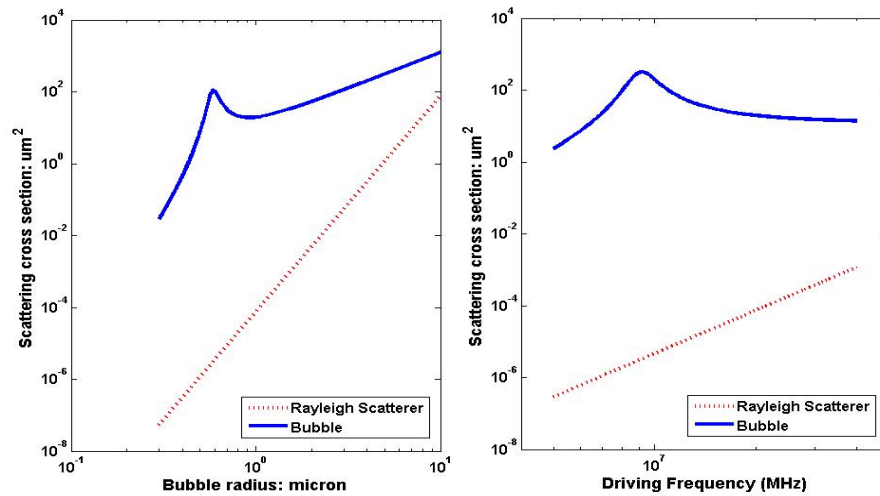


Figure 2-3 The scattering cross section of a bubble and a Rayleigh scatterer as a function of their size when excited at 20MHz (Left) and as a function of the transmit frequency for the scatterers of 1 μm diameter (Right).

2.6 Damping of an Oscillating Bubble

The nonlinear behaviour of bubbles is directly affected by the pressure at the surface of the bubble. This pressure is equal to the summation of the gas pressure inside the bubble and the total damping. There are three main mechanisms of damping in the oscillations of a bubble: Radiation, liquid viscosity and thermal conduction in the entrapped gas. Total damping is the summation of thermal, viscous and radiation damping. These mechanisms reduce the resonance

frequency of the bubble (Leighton 2007). The total damping of a 1 μm diameter bubble is presented in Figure 2-4 and each term is also discussed briefly.

2.6.1 Radiation Damping

Bubbles when driven by the acoustic pressure reradiate a portion of the energy. At lower frequencies when the wavelength is much larger than the bubble size, the radiation damping is small (de Jong, Bouakaz et al. 2002). The radiation damping can be calculated by:

$$\delta_{rad} = \frac{\omega^2 r}{\omega_0 c} \quad (2.27)$$

where c is the speed of sound. r is the bubble radius, ω and ω_0 are the angular transmit and resonant frequency, respectively.

2.6.2 Thermal Damping

The thermal damping depends on the motion of the bubble surface and on the properties of the gas. Expansions and compressions of the bubble cause an increase of the temperature of the gas, which results in a net flow of energy outwards into the surrounding medium. The thermal damping is formulated by Devin and Eller, assuming the same constant temperature for the shell and the surrounding liquid (Devin 1959 and Eller 1970):

$$\delta_{th} = \frac{3p_0}{\omega\omega_0\rho r^2} \text{Im}\left(\frac{1}{\Phi(r, \omega)}\right) \quad (2.28)$$

$$\Phi(r, \omega) = \frac{1}{\gamma} \left(1 + \frac{3(\gamma-1)}{\Psi^2} (\Psi \coth \Psi - 1)\right) \quad (2.29)$$

$$\Psi(r, \omega) = \frac{1}{2}(1+i) \frac{r}{\sqrt{\frac{K_g}{2\omega\rho_g C_p}}} \quad (2.30)$$

where K_g and ρ_g are the thermal conductivity and the density of the gas inside the bubble, respectively. C_p is the heat capacity at constant pressure.

2.6.3 Viscous Damping

Viscous forces in the shell dampen the bubble oscillations. The mechanical resistance from viscous forces in the liquid depends only on the bubble diameter and on the viscosity of the surrounding fluid. Viscous damping δ_η , is calculated by Equation 2.31 (Hoff 2001):

$$\delta_\eta = \frac{4\eta}{\omega_0\rho a^2} \quad (2.31)$$

where η is the viscosity of the liquid. When the 1 μm bubble is excited below 35MHz, viscous damping is the main source of damping.

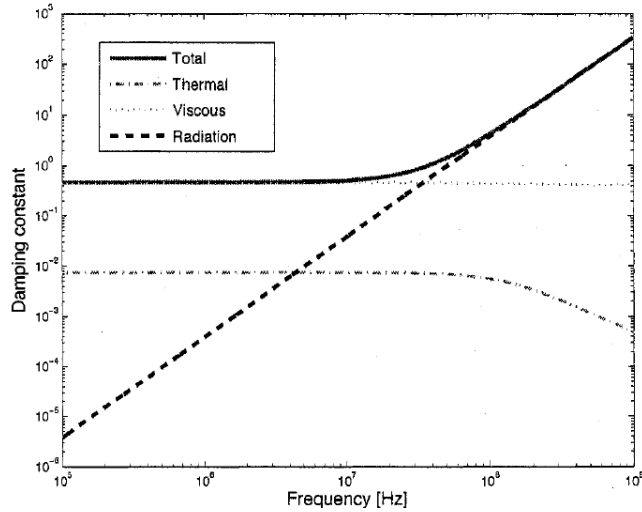


Figure 2-4 Damping constant versus varying transmit frequency for a 1 μm bubble. At higher frequencies, the radiation damping dominates where the viscous damping becomes less significant (replicated from Hoff 2001).

2.7 Keller-Miksis Model

In addition to Rayleigh-Plesset equation, the Keller-Miksis model has been used commonly. This model combines Bernoulli equation, Equation (A.9) (described in Appendix A) with the linear wave equation under the assumption of a constant speed of sound in the medium (Keller and Kolodner 1956; Keller and Miksis 1980). Thus, the equation of motion for the bubble wall is obtained as follows:

$$R\ddot{R}\left(1-\frac{\dot{R}}{c}\right)+\frac{3}{2}\dot{R}^2\left(1-\frac{1}{3}\frac{\dot{R}}{c}\right)-\left(1+\frac{\dot{R}}{c}\right)\frac{p_L-p_0-p_i(t+R/c)}{\rho}-\frac{R}{\rho c}\dot{p}_L=0$$

(2.32)

Assuming linear compressibility and finite constant speed of sound, this model does not have the assumption of small amplitude limitation of Rayleigh-Plesset equation. It takes account of the effects of viscosity, surface tension, incident sound wave and acoustic radiations.

The Rayleigh-Plesset equation, Equation (2.11), can be regenerated from Equation (2.32) if c is infinite based on the assumption of incompressibility of the medium. The solution of this equation can become unstable for high Mach-numbers, which is defined by $\frac{\dot{R}}{c}$. The term \dot{p}_L accounts for the radiation damping. The Rayleigh-Plesset equation ignores the radiation damping. One of the consequences of ignoring the radiation damping in the theoretical calculation of bubble oscillations is obtaining unreasonably large oscillations.

2.8 Simulation Results

The simulations were done in order to investigate the effects of the transmit conditions and the bubble size on the subharmonic signal generation of

an individual bubble. However, since the validity of the model has not been established for the conditions used in the experiments, presented in chapter 3, a direct comparison between the theoretical and experimental results has not been done. Moreover, all the models predict radial oscillations of a single bubble which can not be applied to a polydisperse population of microbubbles.

In order to numerically solve the Keller-Miksis equation, Bubblesim™ which is a program written in Matlab™ was used (Hoff 2001). Bubblesim™ solves the ordinary differential equations of bubble oscillations using an embedded Runge-Kutta algorithm of order 4 and 5 (Kincaid and Cheney 1996). Figure 2-5 shows its graphical user interface which can take the equation, the shell and pulse parameters from the user.

For all the simulations, the Definity™ shell parameters used have been estimated by Goertz et al. over a frequency range of 10 to 30 MHz (Goertz et al. 2007). Based on their measurements, the shear modulus of 190 MPa, the shell viscosity of 0.07 Pas and the constant shell thickness of 1.5 nm were used to solve the Keller-Miksis equation.

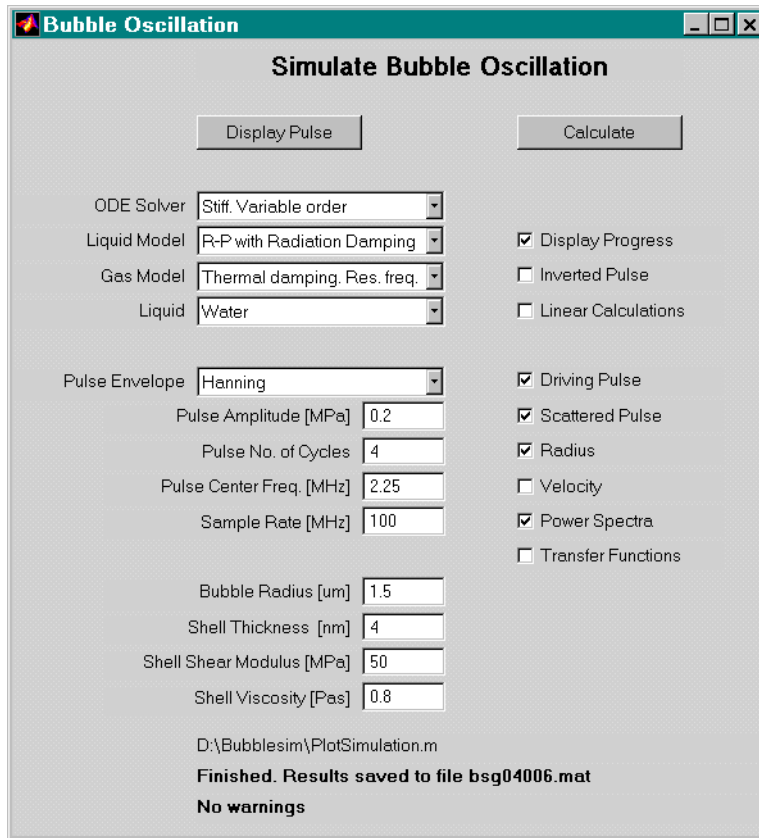


Figure 2-5 Bubblesim graphical user interface.

2.8.1 Limitation of the pulse envelope to detect the subharmonics

Figure 2-6 represents the power spectra of gaussian-enveloped and rectangular-enveloped pulses. The arrows in the figure show the difference between the energy scattered at the fundamental and half the center frequency of the transmit pulse. The higher level of energy observed outside the desired bandwidth for the rectangular-enveloped pulse limits the detection of

subharmonic. The Vevo770™ can not generate the Gaussian-enveloped narrowband pulses. A reference signal which represents the power spectrum of the transmit pulse and the response of the transducer, was always subtracted from the scattered signal of bubbles. In the simulations also, the ratio of subharmonic to fundamental was normalized to that of the rectangular-enveloped transmit pulse.

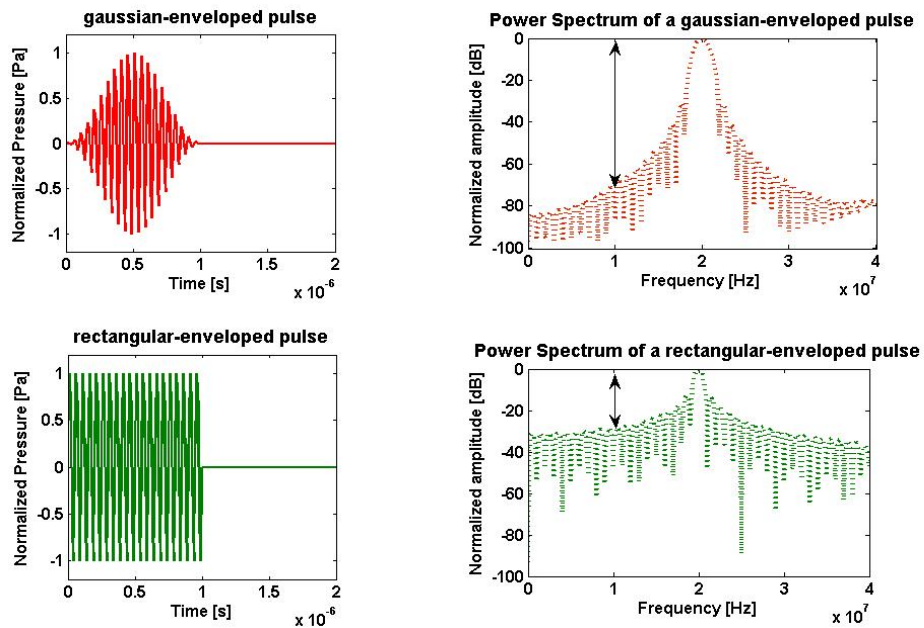


Figure 2-6 Subharmonic detection is more challenging using rectangular-enveloped pulses; the arrows show the difference between the energy scattered at the fundamental and half the center frequency of the transmit pulse.

2.8.2 Effect of bubble size on subharmonic generation

For all the simulations, the bubble sizes of 1.2 and 2 μm in diameter were chosen since previous studies demonstrated the efficiency of scattering from these bubble populations at high frequencies (Goertz et al. 2003). Figure 2-7 shows the undamped resonance frequency versus the bubble diameter. 1.2 and 2 μm bubbles are resonant at 20 MHz and 10MHz, respectively. The radial displacements and the power spectra of these two bubble sizes were simulated at 20 MHz and 40 MHz and presented in Figures 2-8 and 2-9, respectively. The transmit pulse of 20 MHz excites the 1.2 μm bubble at its resonance frequency and the 2 μm bubble at twice its resonance frequency. The numerical solution of Keller-Miksis model predicts that the larger bubbles excited at twice their resonance frequency are more easily driven into subharmonic oscillation. As shown in Figures 2-8 and 2-9, the 2 μm bubble with the resonance frequency of 10 MHz and the 1.2 μm bubble with the resonance frequency of 20 MHz produced the greatest amount of subharmonic signal at 20 MHz and 40 MHz, respectively. Therefore, it can be concluded that a suitable bubble size must be chosen based on the resonance behaviour of bubbles in order to improve the subharmonic generation.

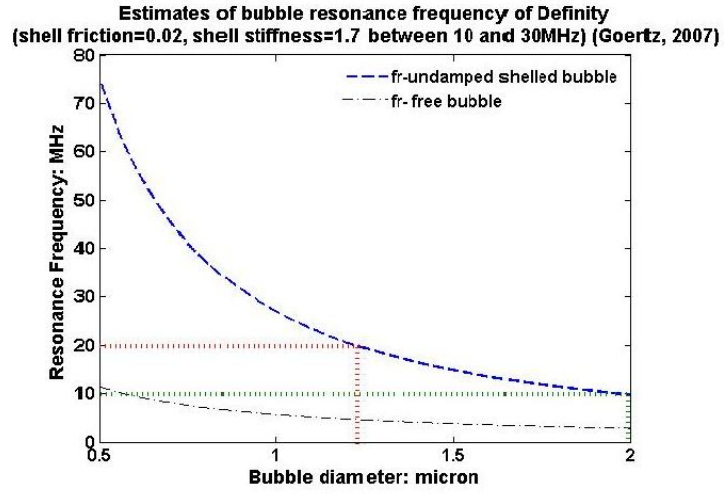


Figure 2-7 Resonance frequency versus bubble diameter. 1.2 and 2 μm bubbles are resonant at 20 MHz and 10MHz, respectively, using Equation 2.24.

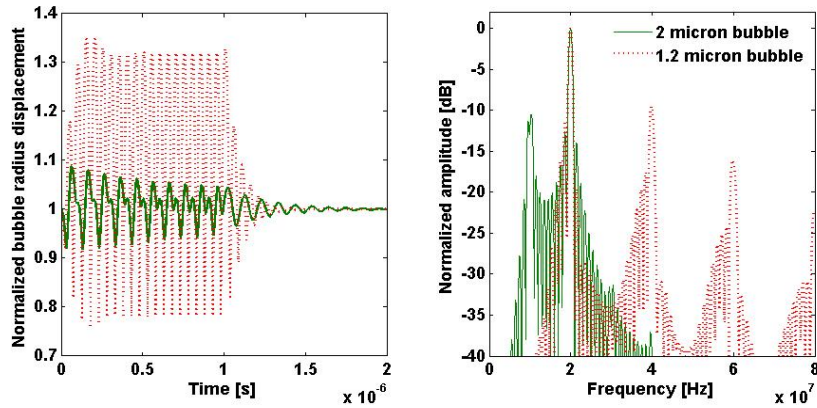


Figure 2-8 The radial displacements and the power spectra of 1.2 and 2 μm bubbles excited using a 20 MHz rectangular pulse.

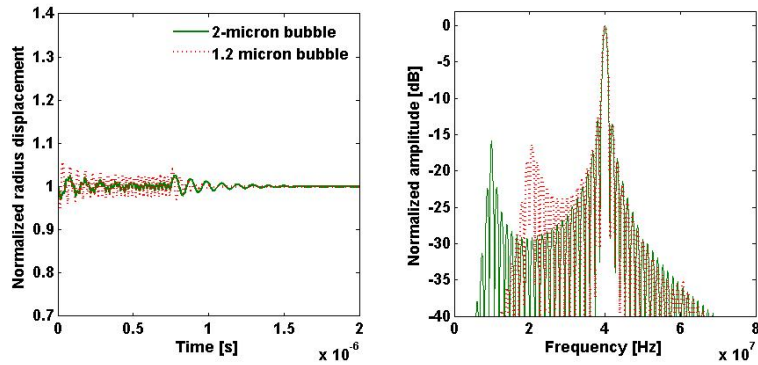


Figure 2-9 The radial displacements and the power spectra of 1.2 and 2 μm bubbles excited using a 40 MHz rectangular pulse.

This model also predicts the maximum oscillations for the smaller bubbles excited at their resonance frequency which can be observed for a 1.2 μm bubble at 20 MHz (Figure 2-6). The scattering from these bubbles is more efficient at 20 MHz, compared with the scattering at 40 MHz.

2.8.3 Subharmonic as a function of transmit frequency

A bubble of any size can produce subharmonics if the transmit pressure is increased above the subharmonic threshold of the bubble (Cheung et al. 2007); Figure 2-10 demonstrates the subharmonic generation for two bubble sizes. The theoretical models always predict a higher threshold for the subharmonic generation, compared with what observed experimentally (Shankar et al. 1999). It

should be noted that it is very difficult to isolate a monodisperse population of bubbles and that these models all assume radially symmetric oscillations of an individual bubble. Therefore, the growth of subharmonics versus transmit frequencies was simulated with the higher pressure than what used in the experiments (1.5 MPa).

For the simulations, the level of subharmonic was calculated from the simulated bubble responses at each incremental frequency step. Then, the ratio of subharmonic to fundamental is calculated and normalized to that of the transmit signal (Figure 2-11). Figure 2-11 shows when the transmit pressure exceeded the subharmonic threshold of both 1.2 and 2 μm bubbles (1.5 MPa), the greatest subharmonic to fundamental occurs within a limited frequency range (Hoff 2001). This frequency range moved towards higher frequencies as a function of the bubble resonance frequency, which increases with a decrease in the bubble diameter.

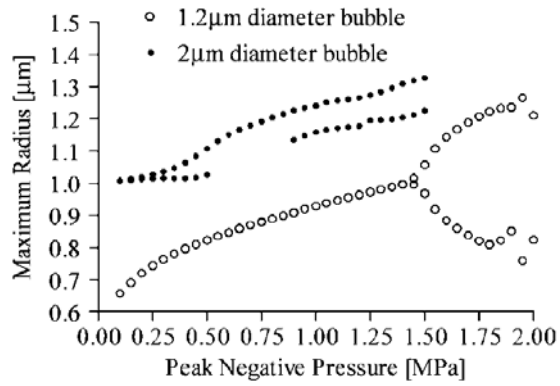


Figure 2-10 When the subharmonic pressure threshold is exceeded, the bifurcation happens in the radial oscillation of bubble. This threshold is minimum for the 2 μm bubble of 10 MHz resonance frequency, excited at 20 MHz (replicated from Cheung et al. 2007).

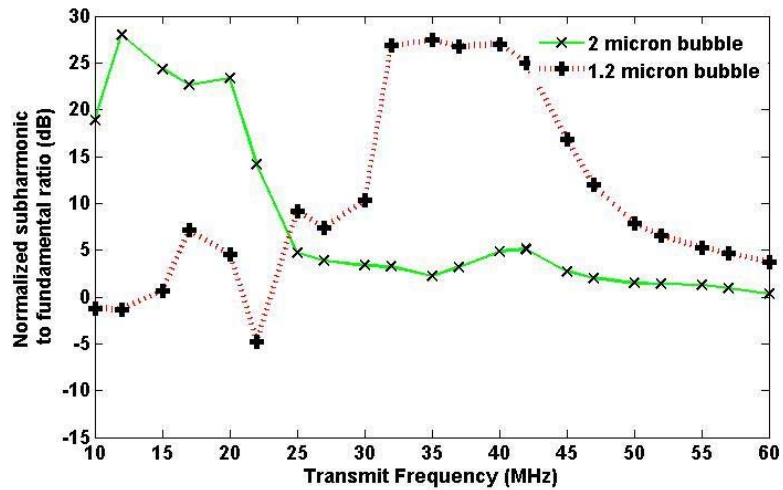


Figure 2-11 The simulated ratio of subharmonic to fundamental as a function of the transmit frequency with the transmit pressure of 1.5 MPa which is normalized to the subharmonic to fundamental of the transmit pulse.

2.8.4 Subharmonic as a function of transmit pressure

The pressure dependency of subharmonic generation was evaluated for two transmit frequencies of 20 and 40 MHz. Figure 2-12 shows that the subharmonics needed higher transmit pressure to develop for the 1.2 μm bubble, (resonant at 20 MHz). The subharmonic to fundamental ratio of each bubble which was normalized to that of the transmit pulse is demonstrated in Figure 2-13. The very rapid onset of subharmonic was not observed for 1.2 and 2 μm bubbles excited at twice their resonance frequencies, 40 MHz and 20 MHz respectively. The reason is that the subharmonic generation from the larger bubbles initiates at very low pressure, as mentioned in section 2.8.3. For these larger bubbles, the maximum subharmonic to fundamental ratio was observed at 600 kPa and 1.2 MPa for the 2 μm bubble at 20 MHz and the 1.2 μm bubble at 40 MHz, respectively.

At 20 MHz, when the pressure threshold for the subharmonic saturation is exceeded, the level of subharmonic depends no longer on the bubble size. At 40 MHz, the subharmonic to fundamental ratio were insignificant for the 2 μm bubble and varied only about 5 dB over the entire pressure range. This implies that when the larger bubbles are excited far above their resonance frequency, the subharmonic to fundamental ratio remains small with varying the transmit pressure.

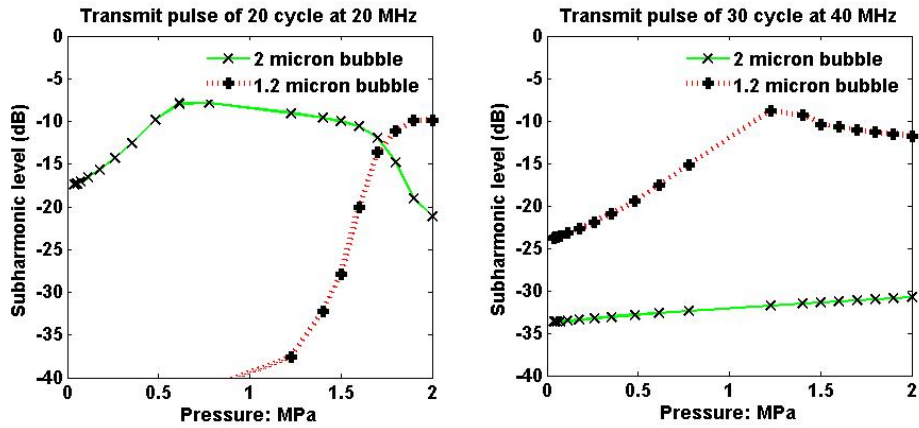


Figure 2-12 The simulated amount of subharmonic versus varying transmit pressure at 20 MHz (left) and 40 MHz (right).

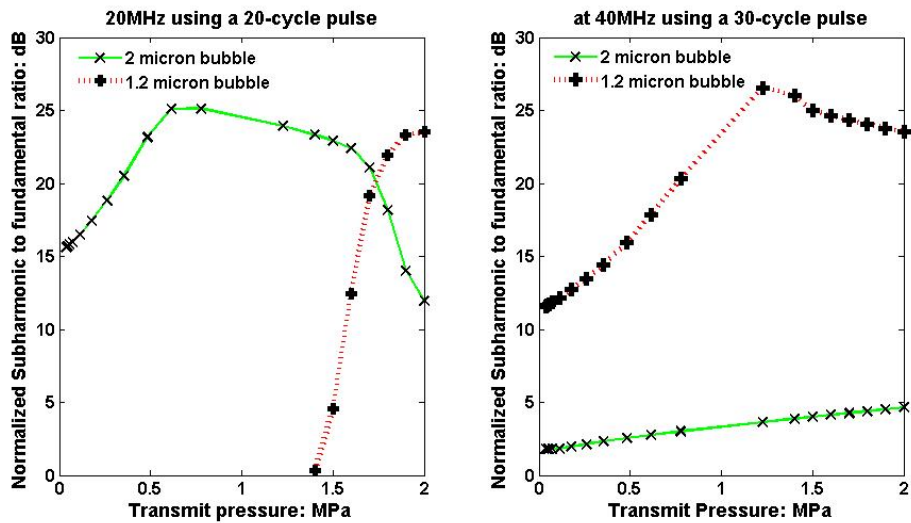


Figure 2-13 The simulated subharmonic to fundamental ratio as a function of transmit pressure at 20 MHz (left) and 40 MHz (right) which is normalized to the subharmonic to fundamental of the transmit pulse.

2.9 Validity of Keller-Miksis Model at High Frequency and High Pressure

2.9.1 Validity at high frequency

The validity of the Keller-Miksis model has not been verified at higher frequencies. Although the important assumption of the small bubble size compared with the incident wavelength is satisfied, the smallest wavelength in the present work is calculated about 25 μm for a 60 MHz pulse. This wavelength is still 10 to 20 times greater than the bubble sizes considered for the purpose of simulations. However, the model can not be used to verify the experiments which involve using the native population with larger bubble sizes ($<12 \mu\text{m}$, Figure 3-9) and does not take into account non-radial oscillations.

The validity of the exponential shell model at higher frequencies, which was used for the simulations in the present chapter, is also questionable. This shell model has only been tested for the shear modulus and shear viscosity measured at 2 MHz (Hoff 2001).

2.9.2 Validity at high pressure

The Keller-Miksis model was developed based on the assumption that the bubble wall velocity is smaller than the speed of sound. Although at higher transmit pressures, when the wall velocity exceeds half the speed of sound, the

model becomes invalid. The assumption of constant speed of sound also ignores the nonlinear propagation of ultrasound which occurs at high pressure amplitude, as described in section 1.4.4.

The mechanisms that can change the size distribution of bubbles are more likely to happen under higher pressures. Bubble destruction is not predicted by this model which has been experimentally observed at high pressures. The bubble dissolution as a result of the gas diffusion can be accelerated under high transmit pressures. This phenomenon shifts down the size distribution of bubbles which in turn, increases their resonance frequency.

A reduction in the resonance frequency of bubbles (as large as 40%) has been observed due to an increase in the transmit pressure (MacDonald et al. 2002). However, there is no term to account for the effect of transmit pressure in the equation of the linear resonance frequency (Equations (2.24) and (2.25), presented in section 2.4). This indicates that the estimation of bubble resonance frequency by the linear approximation is no longer valid at higher pressures.

2.9.3 Validity for a bubble population

Relying on the theoretical simulations of scattering from a single bubble and the feasibility of comparing them with the experimental results for a polydisperse population of bubbles are blurred by the invalidity of the underlying assumptions. Populations of bubbles would produce backscatter spectra that are a

weighted average of the contributions of all bubbles in the irradiated region. One other of these assumptions is that the backscatter from a bubble would be independent of scattering from the neighbouring bubbles. Therefore, the received signal from a bubble population would be equal to the summation signals from each bubble within the beam. In a polydisperse population of bubbles, this assumption is an oversimplification by ignoring the effect of multiple scattering (as described in section 1.5.5).

Moreover, the validity of considering the theoretical simulations of a bubble to explain the behaviour of a bubble population would be based on the assumption of each bubble experiencing the same transmit pressure, regardless of its location in the sound beam. In reality, the transmit pressure changes for each bubble, depending on its spatial location within the beam. This can be due to the combined effects of the complex spatial beam pattern, nonlinear propagation of ultrasound and the bubble attenuation effects (as described in section 1.5.4).

2.10 Summary and Conclusion

The simulations illustrated the importance of transmit conditions to improve the subharmonic generation. An appropriate bubble size must be selected

by considering the resonance behaviour of bubbles, according to the Keller-Miksis model. The simulations supported the theory of subharmonic generation due to the off-resonance oscillation of bubbles excited at twice their resonance frequency. However, the validity of the current models has not been proven at high transmit frequencies and for a polydisperse bubble population. Therefore, these simulations are presented to guide the reader to general trends that can be expected by changing the transmission parameters and bubble size distributions and will not be directly compared to the experimental results.

Chapter 3

Subharmonic Characterization of Microbubbles at High Frequencies

3.1 Introduction

Based on the theory of nonlinear bubble oscillations, bubbles of any size can produce some backscattered energy at half the transmitted frequency, providing a frequency-dependent pressure threshold is exceeded (Eller and Flynn 1969). The origin of subharmonics is not well understood for a population of bubbles at high frequencies. The two most established theories are the subharmonic generation due to either the nonlinear oscillations of resonant bubbles excited at their resonance frequencies (Bohn 1957, Walton 1984 and Leighton et al. 1991) or the off-resonant oscillations of larger bubbles excited at twice their resonance frequencies (Eller and Flynn 1969). In both cases, the formation of subharmonic signal is dependent on the resonance frequency of bubbles as well as the transmit frequency and the resonance frequency of a bubble population increases as the bubble size distribution shifts down to the smaller bubble sizes.

The experiments in this chapter test the hypothesis that the alteration of microbubble population is required to optimize the subharmonic generation at high frequencies. The population alteration shifts the bubble population so that they will be resonant around the transmit frequency of interest. The resonant behaviour of each population was investigated over a wide range of high frequencies. The backscatter experiments were done to characterize the subharmonic signal through changing the following parameters:

- I. Size distribution of bubble population: the three Definity™ bubble populations of 1.2 and 2 μm filtered and native (unfiltered) were examined.
- II. Transmit frequency: the subharmonic signal was measured over a transmit frequency range of 12 to 60 MHz.
- III. Transmit pressure: the changes in subharmonic generation observed with increasing transmit pressure within 35 kPa to 1.2 MPa.

3.2 Materials and Methods

3.2.1 Transducer Characterization

The Vevo770™ (Visualsonics, Toronto, ON, Canada) is a commercially available small animal imaging system which has been widely used in pre-clinical research at high ultrasound frequencies. Two broadband focused PVDF

transducers, the RMV-710B (f-number 2.1; aperture 7.14 mm; focal length 15 mm) and the RMV-708 (f-number 2.25; aperture 2 mm; focal length 4.5 mm) (Visualsonics, Toronto, ON, Canada) were used in pulse-echo mode for all the experiments. The transducers were characterized by a 40-micron needle hydrophone (Precision Acoustics, Dorset, UK), calibrated up to 60 MHz by the NPL (National Physical Laboratories, Teddington, UK). All the hydrophone measurements are illustrated in Appendix B. The narrowband output peak negative pressure of the transducers was measured from 35 kPa up to 1.2 MPa for a frequency range of 10 to 60 MHz.

The Vevo770™ has been originally designed to produce broadband pulses (~100% nominal bandwidth) for high resolution imaging. However, the transmit parameters such as number of cycles, transmit frequency and pressure were altered through the access to the software engineering mode. Longer pulses with a narrowband power spectrum are required for the subharmonic signal to develop (Eller and Flynn 1969). In addition, the technique chosen to do the attenuation coefficient measurements is narrowband, having a better signal to noise ratio compared with that of the broadband measurements. The digital RF-Mode of Vevo770 provides the operator with the ability to record, digitize and export the raw RF data at the sampling frequency rate of 420MHz. The received RF lines were hanning-windowed in a window of 3mm (width) ×2mm (length) for RMV-710B and 2mm (width) ×1mm (length) for RMV-708. The power spectra of the

200 recorded RF lines (20 lines, 10 frames) are calculated and averaged in Matlab™ (The MathWorks Inc., Natick, Mass., USA).

The presence of nonlinear propagation and energy transmitted within or outside of the intended bandwidth which is not due to the nonlinear oscillation of bubbles was investigated. For this purpose, a reference signal is obtained by the reflection from the surface of oil (Dow Corning® 710 Fluid). Subtracting the reference signal from the bubble responses can account for these effects. For all the experiments, the ratio of subharmonic to fundamental scattered by microbubbles was normalized to that of the reference signal in order to account for the response of the transducer and the electronics.

3.2.2 Agent Handling

Definity™ (Bristol-Mayers Squibb Medical Imaging, Montreal, Canada) was kept refrigerated and brought to room temperature 10 minutes before use. The agent was activated using a Vialmix™ agent activator (Bristol-Mayers Squibb Medical Imaging, North Billerica, MA, USA) at room temperature. The process of activation involves mechanical agitation of the vial for 45 seconds. The vial was left for 10 minutes to return to the room temperature. After remixing by hand, the vial was inverted for 30 seconds before the extraction of the contrast agent. Agent was extracted using an 18 gauge needle (PercisionGlide® Needle,

Becton Dickinson & Co.) into a 1-ml Tuberkulin syringe (Norm-Ject®, Henke Sass Kronens, Germany) from the inverted vial while venting with a second 18 gauge needle. Venting is done to stabilize the pressure inside the vial. For the native experiments, 60 µl of extracted agent was gently mixed with Isoton II (Coulter Electronics, Luton, UK). Isoton II is a standardized diluting liquid, used in laboratories. It consists of a 0.9% saline solution with a phosphate PH-buffer and a detergent to reduce the surface tension (Hoff 2001). For the filtration experiments, higher concentrations of the agent were used in order to compensate for the loss of volume fraction due to the population manipulation.

3.2.3 Population Alteration

Mechanical filtration was done by using Isopore™ polycarbonate membranes of 1.2 and 2 µm size (Millipore Corporation). The extracted contrast agent was mixed with 30mL of Isoton II at room temperature. This suspension was gently pushed through each filter at an approximate rate of 6mL/min. After the filtration of 15mL, the filter was replaced to reduce clogging of the filter micropores. The filtered agent was then further diluted with Isoton II to the concentration of interest. The success of agent filtration procedure was verified through the size distribution measurements of the bubbles using a particle analyzer.

3.2.4 Size Distribution Measurements

Size distributions were measured with particle size analyzer, Microtrac™ S3500 (Microtrac Inc., FL, USA) with a measurable size range of 0.02 to 2000 μm . The measuring range of instrument is divided into fixed “channels” or particle sizes. As shown in Figure 3-1, Microtrac™ uses three lasers to illuminate the sample to be measured. The particles inside the samples scatter the light in an angular pattern, depending on their sizes. The two detectors allow light scattering measurements to be made from approximately zero to 160 degree. Switching the lasers on, one at a time, multiplies the number of sensors used to detect the scattered light from the particles. The particle size distribution is regenerated from the resultant scattered light data of all three lasers.

For each bubble population, the concentration was 0.1% by volume and the measurements were repeated three times. The percentage of bubbles present in each channel was calculated and presented versus the bubble diameters.

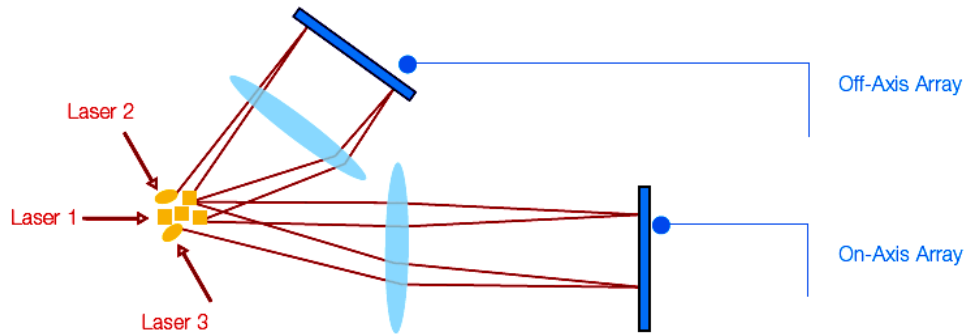


Figure 3-1 In Microtrac™, switching the lasers on, one at a time, multiplies the number of sensors used to detect the scattered light from the sample.

3.2.5 Attenuation Coefficient Measurements

When ultrasound passes through a medium, it undergoes energy losses. These losses are resulted from the absorption, which causes the heat generation and scattering due to changes in the compressibility and density. The attenuation in a suspension of bubbles can be measured by comparing the received signal without and with contrast agent in the sound path (known as substitution method) (de Jong et al. 1992). It means that the signal from the agent is compared with a reference in order to compensate for the frequency response of the transducer and for the characteristics of the sound path. The attenuation coefficient, defined in terms of a combined effect of absorption and scattering, is expressed in dB per unit length as:

$$\alpha_{dB} = -\frac{20}{x} \log(p_M / p_R) \quad (3.1)$$

where x is the thickness of the sample whose attenuation coefficient is to be calculated; p_M is the amplitude of the received signal with the sample. The reference signal of amplitude p_R is chosen to be measured in water or in saline solution (Hoff 2001).

The resonance response of microbubbles was investigated by measuring the frequency-dependent attenuation coefficient of bubble suspensions. This, in turn, determines the best transmission frequencies for each bubble population as the attenuation coefficient is largest at the most effective resonant frequencies. Agent characterization was done by the narrowband pulse-echo attenuation coefficient measurements using the substitution method.



Figure 3-2 In this custom-made container for the attenuation measurements, ultrasound beam was reflected off a quartz plate, located at the focus of the transducer.

Two broadband focused PVDF transducers (RMV-710B and RMV-708) were used to cover a frequency range of 10MHz to 60MHz. The agent was diluted in a custom-made container in which ultrasound beam was reflected off a quartz plate, located at the focus of the transducer (Figure 3-2). Figure 3-3 illustrates a schematic of the setup for the attenuation measurements. The suspension was mixed gently within the container during the entire time of the experiments in order to minimize the bubble floatation effects. The mixing ensures different populations of bubbles to be interrogated with transmit pulses.

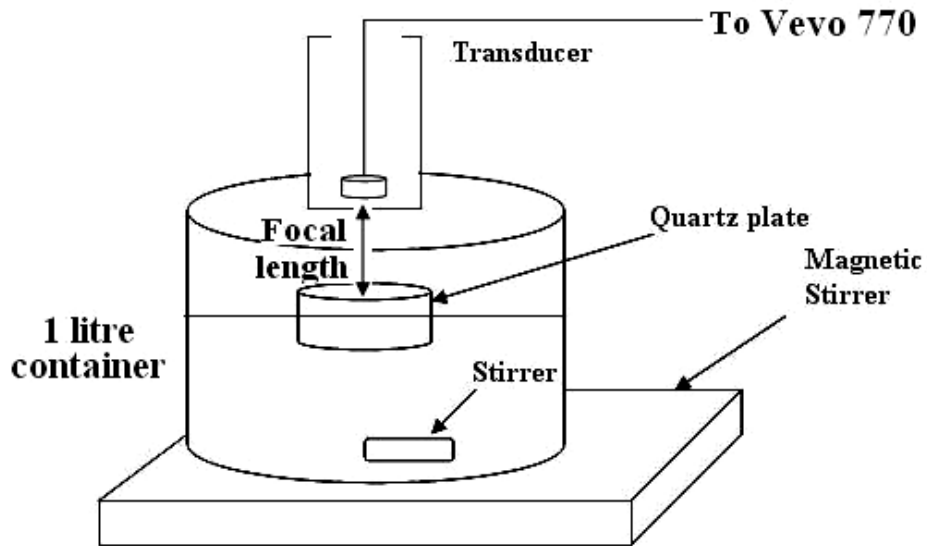


Figure 3-3 Setup for the attenuation measurements of the bubble suspension. The beam is reflected off the surface of the quartz plate.

A sequence of narrowband pulses (30 cycles) was transmitted to sweep the bandwidth of each transducer (10 MHz to 35 MHz for RMV-710B and 30 MHz to 60 MHz for RMV-708) in steps of 2 or 3 MHz (i.e. 10 MHz, 12 MHz, 15MHz,...). Figure 3-4 shows a typical narrowband pulse, used in the experiments, in time and frequency domain. Narrowband attenuation measurements allow for the use of low transmit pressure in order to avoid the pressure-dependent attenuation effects and to enable the comparison with the linearized bubble models (Goertz et al. 2007). The potential pressure-dependent attenuation effects cause the attenuation coefficient to resemble the transmit

pressure amplitude, which depends on the transmit frequency (Chen et al. 2002). Moreover, longer pulses have a higher energy at their center frequency, which also results in a better signal to noise ratio. The peak negative pressure level of 40 kPa was used for the attenuation measurements, measured with the method described in section 3.2.1.

The agent was handled according to the agent handling instruction (section 3.2.2). A concentration of 1:3600, 1:9100 and 1:15000 was used for 1.2 and 2 μm filtration and the native experiment, respectively, in order to maintain a good sensitivity in the attenuation measurements. The measurements started 1 minute after diluting and mixing the agent in the container (Goertz et al. 2007). For each population, six measurements at each frequency were performed on the two samples for each population which were prepared separately. The total time of data acquisition was approximately 10 minutes for each sample.

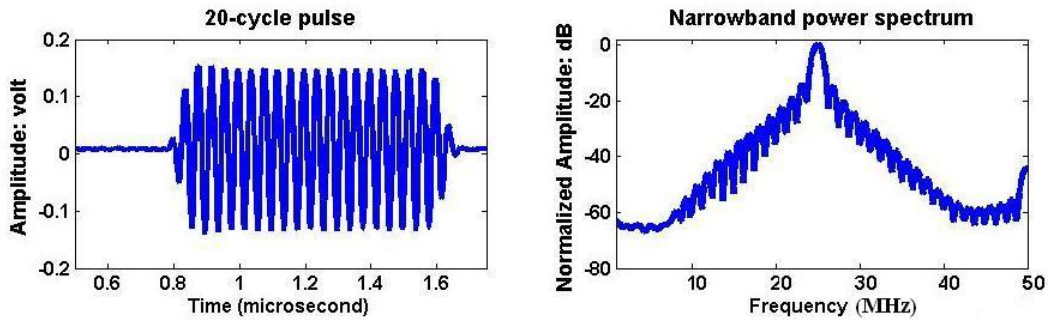


Figure 3-4 A typical 20-cycle pulse at 25 MHz, used in all the experiments, in time and frequency domain.

3.2.6 Backscatter Measurements

The RMV-710B and RMV-708 transducers were used in pulse echo mode to cover a frequency range of 12MHz to 60MHz. Figure 3-5 illustrates the setup for the backscatter measurements. Agent was handled as described in section 3.2.2. A 500 ml vessel containing the microbubble suspension was sealed by a Saran™ membrane and immersed in a water tank. This container has a small angle of 20 degree with the bottom of the water tank in order to prevent the air bubbles which might be entrapped behind the membrane and interfere with the beam path (Figure 3-6). The beam was focused 2 mm behind the membrane and microbubbles were stirred continuously in the container during the experiments. Figure 3-7 demonstrates the display of the Vevo770™ in RF mode during a typical backscatter experiment.



Figure 3-5 Setup for the backscatter measurements.

Concentrations of 1:2000, 1:1500 and 1:1000 were used for native population, 2 and 1.2 μm filtered microbubbles, respectively. A low frame rate of 10Hz ensured scanning slowly enough in order to obtain a good representation of bubble population, being insonified at the transmit frequency of interest. The power spectra of 200 independent RF lines were averaged. Electronic noise also was recorded and only the data from the received power spectra which were above the noise were taken into account. The spectra were integrated in two frequency bands: subharmonic (0.46 to 0.54 times the transmit frequency) and fundamental (0.96 to 1.04 times the transmit frequency) as shown in Figure 3-8. The same integration was done for the reference signal, reflected from the surface

of the oil, at each frequency or pressure step. Then, the ratio of the subharmonic to fundamental of the reference signal was calculated and subtracted from that of each bubble population for each transmit parameter. Six trials were performed for each data point for two independent samples. The error bars represent the standard error of all the 6 trials, unless otherwise stated.

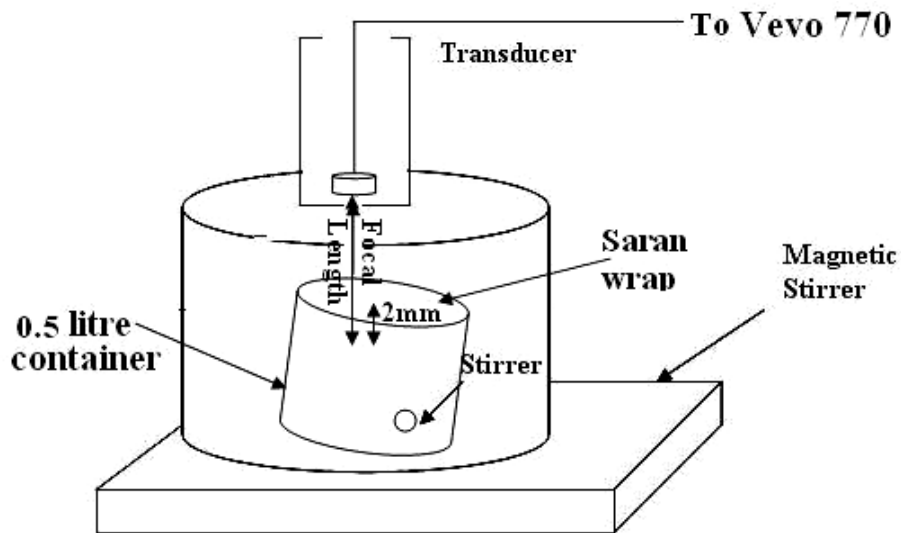


Figure 3-6 Schematic of the setup for the backscatter measurements. The beam is focused 2 mm behind the Saran membrane.

The subharmonic signal and the subharmonic to fundamental ratio for three bubble size distributions of native, 1.2 μm filtered and 2 μm filtered were measured for a range of transmit pressures and frequencies. In all the results, the

subharmonic to fundamental ratio was normalized to that of a reference signal which was obtained from the oil interface as described earlier.

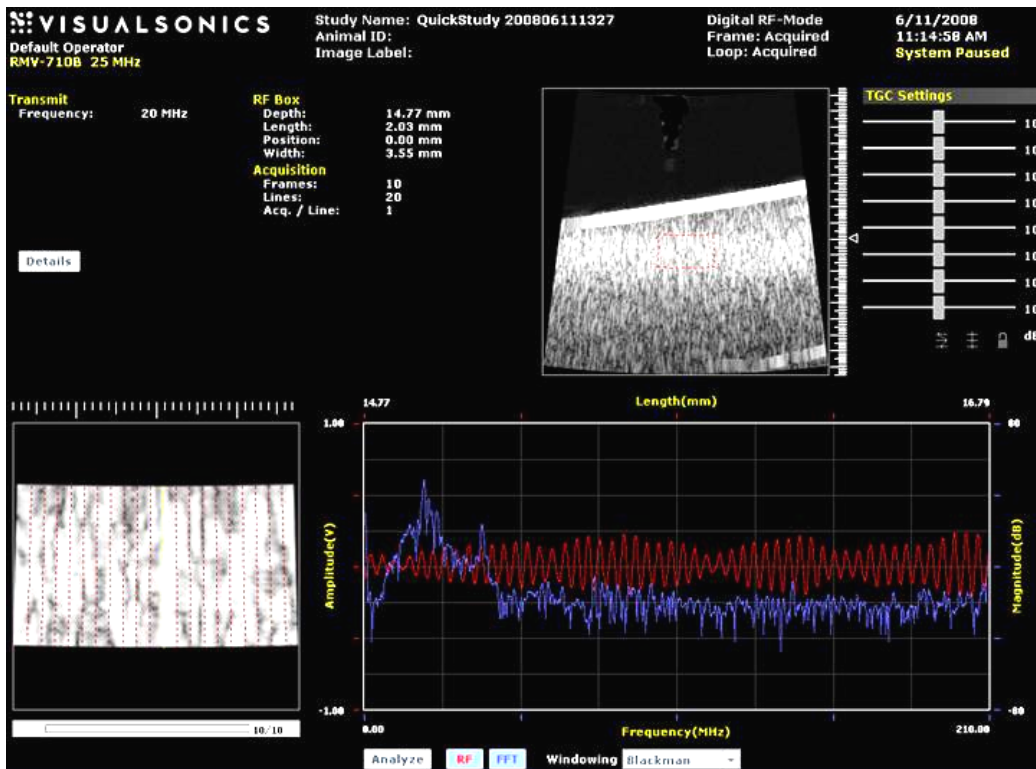


Figure 3-7 Display of the Vevo770™ in RF mode during a typical backscatter experiment. The region of interest which was selected in the B-mode image (on the top) is shown separately on the bottom left corner. The time (red line) and frequency (blue line) domain representation of each line within the region of interest can be presented in the bottom right graph.

3.2.7 Subharmonic generation under varying transmit conditions

As described in section 3.1, the transmit frequency and pressure were changed in order to characterize the subharmonic signal from various Definity™ bubble populations. In order to find the optimal frequency at which bubbles in each population can emit the maximum subharmonic signal, the subharmonic signal was measured over a frequency range of 12 to 60MHz. 20-cycle rectangular-enveloped pulses were used to excite the bubbles at incremental frequency steps. The peak negative transmit pressure was kept at 400 kPa over the entire frequency range through the engineering software mode. This pressure level is considered enough to generate the subharmonic from the selected bubble size distributions in the present work.

The subharmonic generation was studied with varying the transmit pressure at 20 MHz and 40MHz. 20-cycle and 30-cycle rectangular-enveloped pulses were used to excite the bubbles over a pressure range of 35 kPa to 1.2 MPa at 20 MHz and 40 MHz, respectively.

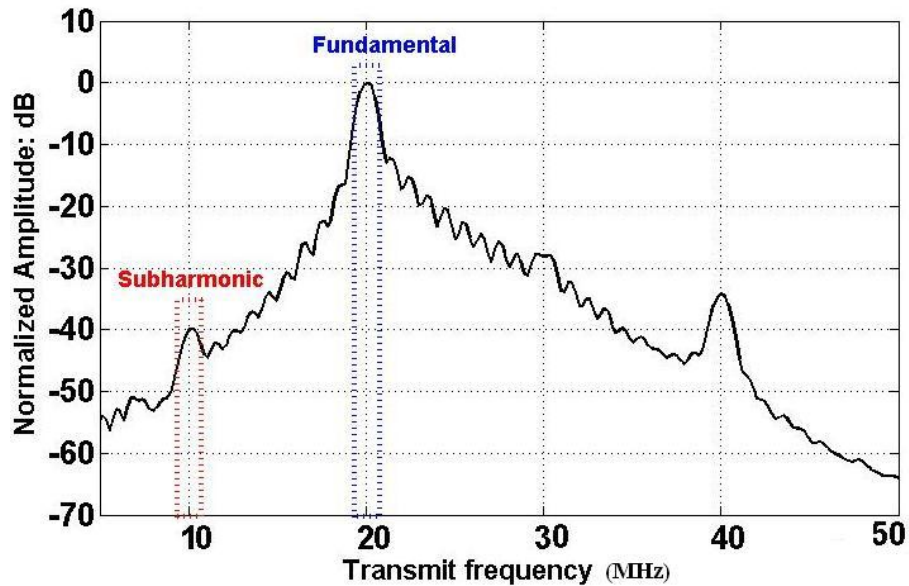


Figure 3-8 A typical received spectrum of a native bubble population which is integrated in two frequency bands: subharmonic (0.46 to 0.54 of the transmit frequency) and fundamental (0.96 to 1.04 of the transmit frequency).

3.3 Experimental Results

3.3.1 Size Distribution Measurements

The size distributions of 1.2 μm and 2 μm filtered and native populations measured by the particle analyser are shown in Figure 3-9. A bimodal distribution was measured with a large number of submicron bubbles observed in the native size distribution. The size distributions of 1.2 μm and 2 μm filtered populations

demonstrated a successful removal of the majority of bubbles larger than the filter pore size.

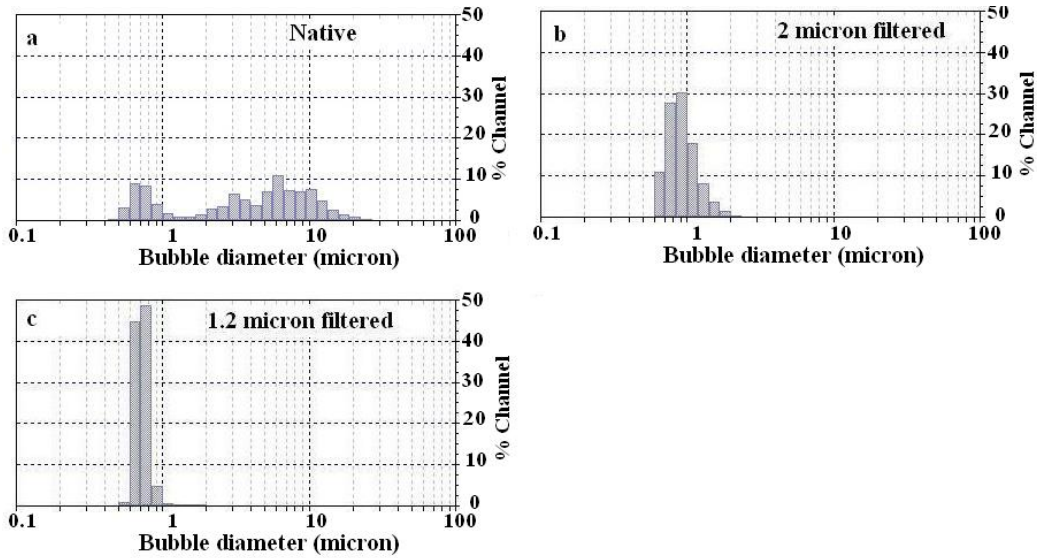


Figure 3-9 The size distributions of a) native b) 2 μm and c) 1.2 μm filtered populations show a successful removal of the majority of bubbles larger than the filter pore size.

3.3.2 Attenuation Coefficient Measurements

The results of narrowband frequency-dependent attenuation measurements are shown in Figure 3-10. The error bars represent the standard errors of 6 measurements, collected from the 2 independent samples. For the native Definity™, a peak in the attenuation measurements occurred around 12 MHz and it decreases to half of its peak value at about 50MHz. the attenuation rises up to 15-22 MHz for 2 μm filtered bubbles, followed by a gradual decrease at higher

frequencies. For 1.2 μm filtered bubbles, the peak is shifted up to 30 to 40MHz and the attenuation coefficient remains high up to 60 MHz.

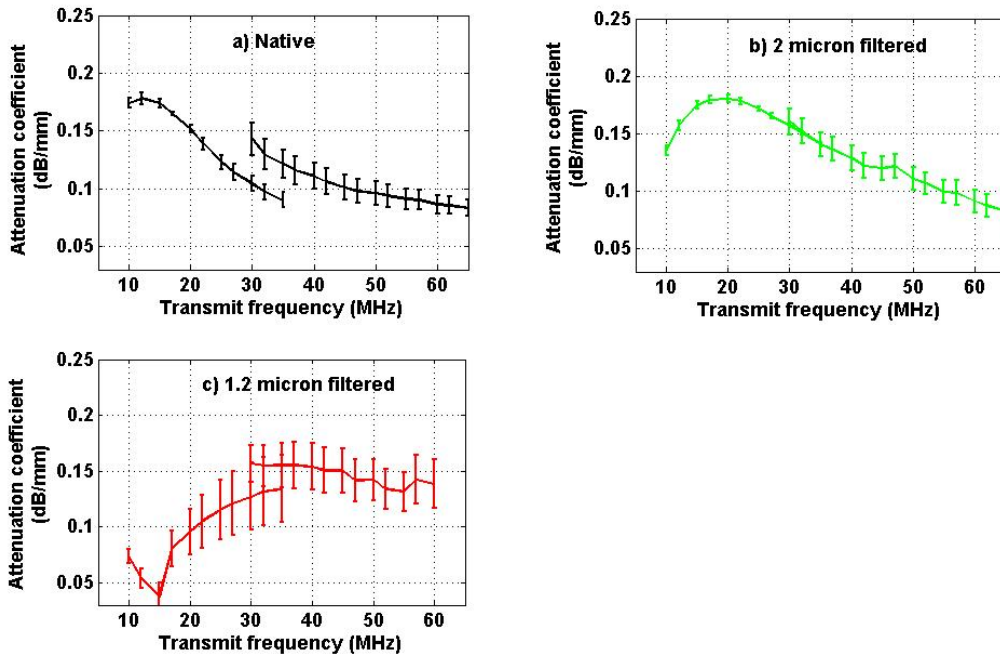


Figure 3-10 The narrowband attenuation coefficient measurements of a) native b) 2 μm and c) 1.2 μm filtered populations, using two transducers the RMV-710B and RMV-708. It demonstrates an increase in the resonance frequency (peak of the attenuation coefficient) of each population due to the alteration of bubble populations.

3.3.3 Backscatter Measurements

The averaged power spectra from each of three bubble populations excited at 20 MHz with a 20-cycle rectangular-enveloped pulse of 400 kPa are shown in Figure 3-11. The power spectra were normalized to the 20 MHz fundamental of each bubble population. The subharmonic energy at half of the transmit frequency was observed above the noise floor for all three bubble populations. The 1.2 μm filtered population generated the greatest amount of subharmonic energy relative to the fundamental, -36 dB. The 2 μm filtered and native populations exhibited the subharmonic to fundamental ratios of -39 and -40 dB, respectively.

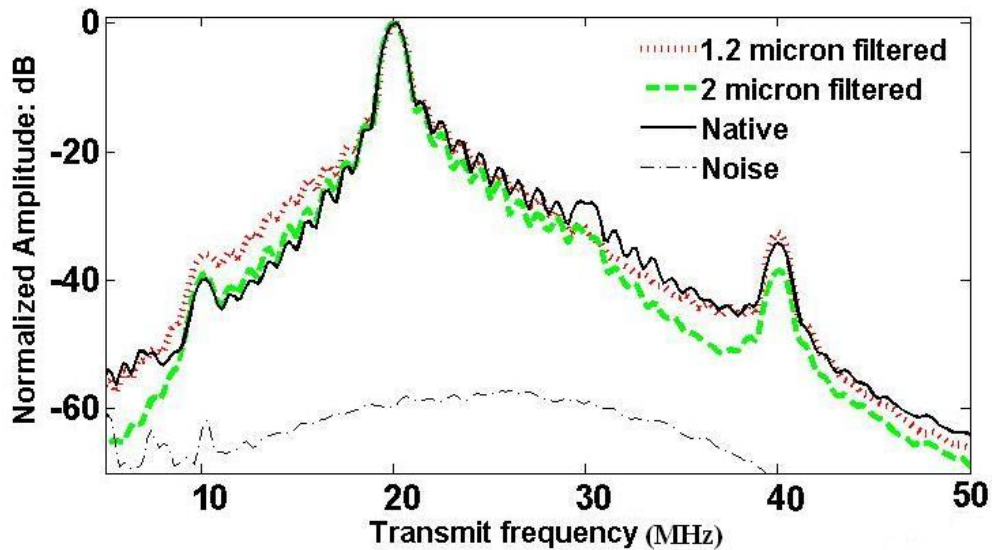


Figure 3-11 The averaged power spectra (average of 200 lines) from each of three bubble populations excited at 20 MHz with a 20-cycle rectangular-enveloped pulse of 400 kPa. The power spectra were normalized to the fundamental of each bubble population.

3.3.4 Subharmonic as a function of transmit frequency

The subharmonic to fundamental ratio was measured over a wide range of transmit frequencies, 12 to 60 MHz. This was normalized to the subharmonic to fundamental ratio of a reference signal which was obtained from the oil interface (section 3.2.6). Since the ratio of subharmonic to fundamental of the reflected signal from oil interface is a larger negative number (compared with that of the bubble population) the normalized ratio was calculated as a positive number. The

peak negative transmit pressure was 400 kPa for all the transmit pulses. 20-cycle rectangular-enveloped pulses were used. The result in Figure 3-12 shows the greatest subharmonic energy relative to the fundamental for 1.2 μm filtered bubbles around 20 MHz. This ratio is almost constant over the entire frequency range. 2 μm filtered and native population exhibited the maximum ratio at around 12 MHz, followed by a drop of approximately 8 dB at 20 MHz. For frequencies above 20 MHz, there are small changes in the subharmonic to fundamental ratio.

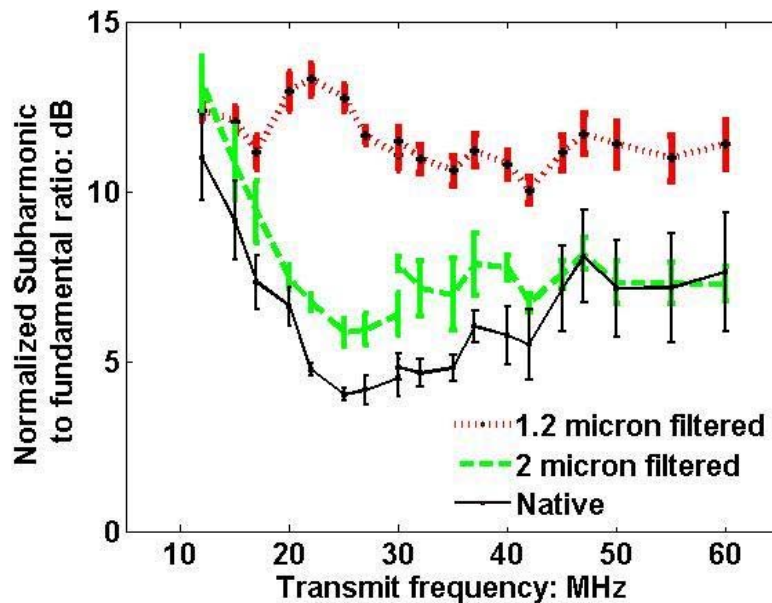


Figure 3-12 The normalized subharmonic to fundamental ratio versus varying transmit frequency, using 20-cycle rectangular-enveloped pulses at the peak negative transmit pressure of 400 kPa.

3.3.5 Subharmonic as a function of transmit pressure at 20 MHz and 40 MHz

Subharmonic generation from various bubble populations was investigated as a function of transmit pressure at two transmit frequencies of 20MHz and 40 MHz. All the graphs were normalized to the fundamental of the scattered pulse at the lowest transmit pressure for each bubble population. The peak negative pressure of transmitted pulses was varied between 35 kPa and 1.2 MPa for 20-cycle pulses at 20 MHz and for 30-cycle pulses at 40 MHz.

The absolute values of subharmonic and fundamental energies at 20 MHz and 40 MHz are presented in Figure 3-13. The error bars represent the standard errors of 6 measurements, collected for the 2 independent samples with 3 trials for each sample. Regardless of bubble size distributions, scattering at fundamental and subharmonic energies seem to be more efficient at 20 MHz, compared with those at 40 MHz. The fundamental and subharmonic energies continue to increase with the transmit pressure for the three bubble populations at 20 MHz and 40 MHz. The growth of the subharmonic and fundamental signals are slower for 1.2 μm filtered bubbles as the transmit pressure increases.

At 20 MHz, the regions of subharmonic generation, onset and rapid growth followed by saturation for the higher transmit pressure (>400 kPa), were observed. The onset of subharmonic signal for 1.2 μm filtered bubbles started 10

dB above that of 2 μm filtered and native populations. At 40 MHz, the subharmonic energy does not vary significantly for the altered bubble populations. The onset of subharmonic signal is the same for all three populations. There is an increase in the subharmonic energy with the transmit pressure. The saturation does not happen within the transmit pressure range.

The normalized ratios of subharmonic to fundamental of each bubble population are presented in Figure 3-14, which expresses the amount of subharmonic energy relative to the fundamental. The 1.2 μm filtered bubbles generate the greatest subharmonic to fundamental ratio at both 20 MHz and 40 MHz.

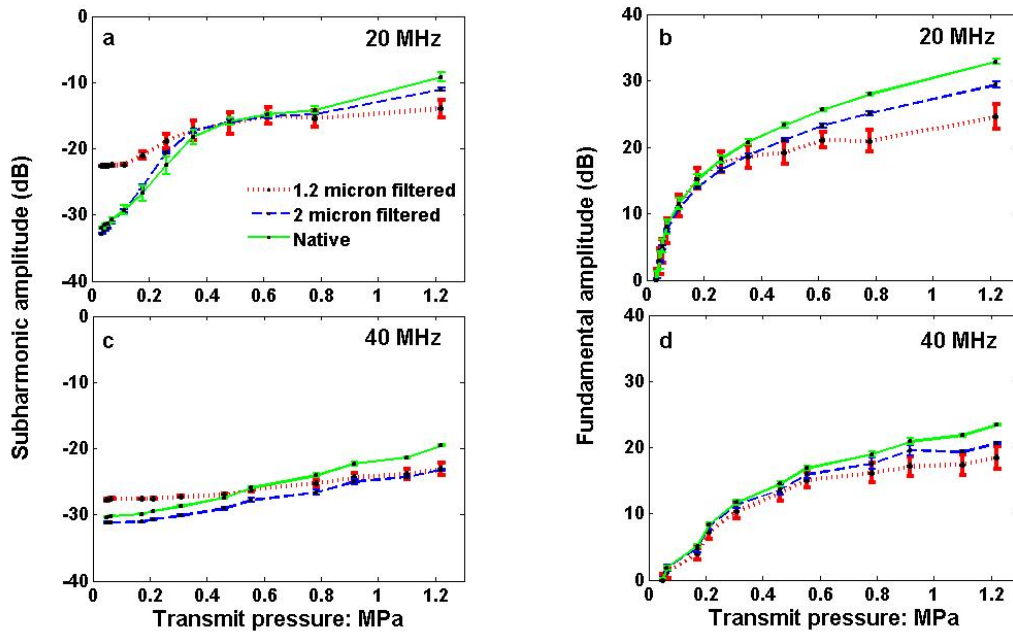


Figure 3-13 The absolute values of subharmonic and fundamental energies at 20 MHz and 40 MHz normalized to the lowest fundamental amplitude of each bubble population.

At 20 MHz, the 1.2 μm filtered bubbles have the greatest normalized subharmonic to fundamental ratio, approximately 34 dB between 400 and 600 kPa. Over the same pressure range, the subharmonic amplitude for 2 μm filtered and native populations were 16 dB and 15 dB, respectively. At 20 MHz, this ratio saturates and drops gradually for the three bubble populations with higher transmit pressures.

Unlike the result at 20 MHz, there is a smooth growth in the subharmonic to fundamental ratio of the three bubble populations at 40 MHz. The 1.2 μm

filtered bubbles generate the greatest subharmonic to fundamental ratio at 20 MHz and 40 MHz. At 40 MHz, this ratio is increased by 15 dB for 2 μm filtered and native populations, compared with their ratio at 20 MHz.

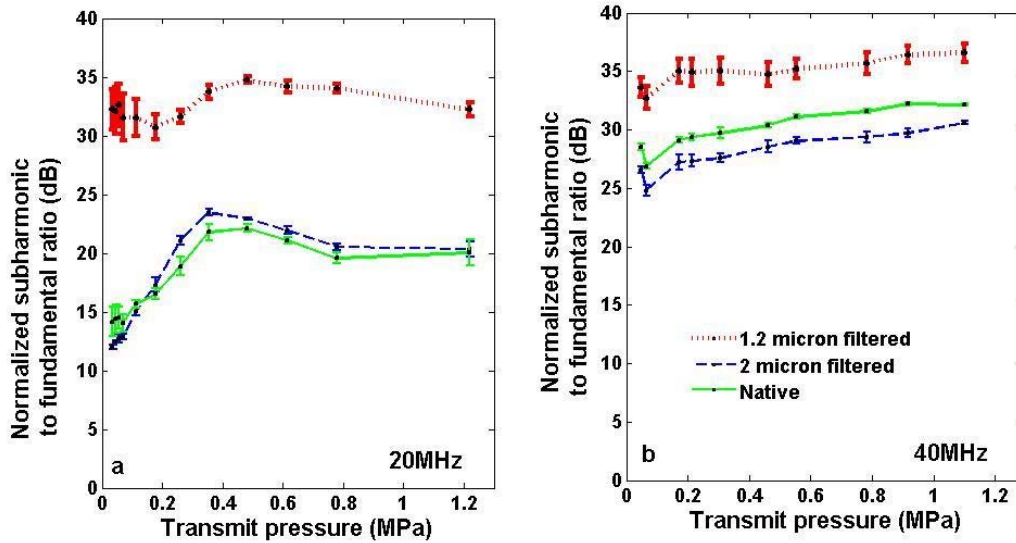


Figure 3-14 The normalized ratios of subharmonic to fundamental for each bubble populations at a) 20 MHz and b) 40 MHz.

3.4 Discussion of Results

It should be noted that the possibility of the bubble disruption and pressure-dependent attenuation were not examined in this work. However, a transmit pressure of only 40 kPa, corresponding to a very low mechanical index

(0.005 to 0.012 at 60 and 10 MHz, respectively), was used for the attenuation measurements in order to prevent these effects (Goertz et al. 2007). No signs of bubble disruption for Definity™ have been previously reported below the pressure level of 0.9 MPa at 20 MHz (Needles et al. 2005). With another lipid shell agent, BG2423™ (Bracco Research), the bubble destruction occurred above 1.5 MPa using 30 MHz pulses of 5% bandwidth (Goertz et al. 2006a). The significant destruction of Definity™ microbubbles has not been observed until the pressure level higher than 5 MPa at 20 MHz (Goertz 2002, Goertz et al. 2005 and Kruse et al. 2002). Therefore, a stable (non-destructive) regime of the subharmonic generation is expected within the low transmit pressures (<1.2 MPa) used in the backscatter measurements of the present work. In addition, the effects of the duty cycle and the bandwidth of the transmit pulses on subharmonic generation have not been considered in this work. Cheung et al. showed that increasing the number of cycles (more than 5 cycles) in transmit pulses did not affect the subharmonic to fundamental ratio at high frequencies (Cheung et al. 2008).

3.4.1 Attenuation Coefficient Measurements

The attenuation measurements in section 3.3.2 have shown the significant levels of attenuation at high frequencies due to the resonant oscillation of

Definity™ microbubbles of various size distributions. The results in Figure 3-10 were consistent with the published data (Goertz et al. 2007). By isolating the subpopulation of bubbles below 1.2 μm and 2 μm through filtration process (Figure 3-9), there is a trend of increasing the resonant frequency of bubble populations up until 50MHz. The nonlinear behaviour of Definity™ at high frequencies has been attributed to the resonant activity of submicron bubbles, which results in an increase in their frequency-dependent attenuation (Goertz et al. 2005 and 2006b; Cheung et al. 2005). 1.2 μm filtered bubbles exhibited a high attenuation coefficient over a wide range of frequencies, 10 MHz to 60 MHz, where it is believed the majority of these bubbles are resonant (Goertz et al. 2007). This suggests that they can be easily driven to nonlinear oscillations at high frequencies. Therefore, 1.2 μm filtered bubbles can be good candidates for high frequency subharmonic imaging. It should be noted that the attenuation coefficient is very sensitive to the concentration of bubble suspensions. For the attenuation measurements, the amount of agent extracted for each sample was very small (section 3.2.5) which makes it difficult to prepare identical samples. A new sample was prepared for each transducer in each trial. This can explain the disjointed data of Figure 3-10. A small increase in concentration of a bubble population results in a higher attenuation coefficient. The attenuation coefficient does not increase linearly with a high concentration of microbubbles (Goertz et al. 2007).

3.4.2 Backscatter Measurements

Experiments described in section 3.3.3 supported the hypothesis. An increase in the subharmonic to fundamental ratio was measured due to the bubble population alteration. The 1.2 μm filtered bubbles demonstrated the greatest subharmonic energy relative to the fundamental at 20 MHz (Figure 3-11). However, the numerical simulations of the Keller-Miksis model in Figure 2-8 showed that a 2 μm SINGLE bubble with a natural resonance frequency of 10MHz have a higher subharmonic signal than that of a 1.2 μm single bubble. When excited at 20 MHz, this model supports the theory of subharmonic generation due to the off-resonant oscillations of larger bubbles excited at twice their resonant frequency (described in section 1.9.3). If this theory was supported by the experimental results, one would expect the native population with the measured resonance frequency of 10 to 12 MHz (Figure 3-10) to produce the greatest subharmonic energy. This is because these bubbles were excited at 20 MHz, twice their resonance frequency. Therefore, these experimental results do not support the most commonly accepted theory of subharmonic generation. However, it should be again emphasized that the model has all the shortcomings listed in section 2.9 and is based on the response of a single bubble rather than that of a population used in these experiments. Moreover, an average diameter of 2 μm can not be assumed for the native population based on the 10 to 20 MHz peak measured in its attenuation coefficient. In fact, the size distribution

measurements of the various bubble populations can also support this statement (Figure 3.9).

Neither the theory of subharmonic generation from nonlinear oscillations of resonant bubbles excited at their resonant frequency (section 1.9.2) can be supported by the results; if this theory held for our system, the 2 μm filtered bubbles with a measured resonance frequency around 20 MHz (Figure 3-10) would generate the maximum subharmonic signal. In these experiments, however, the maximum subharmonic signal was obtained from the 1.2 μm filtered bubbles. Yet, the latter theory can not be ruled out, since there is likely a downshift in the resonance frequency of the bubble populations under high transmit pressures (MacDonald, Sboros et al. 2002). Therefore, it can be reasonably hypothesised that the resonance frequency of each bubble population could be reduced under the transmit pressure of 400 kPa (an order of magnitude higher than that used to measure the resonance frequency, 40 kPa). If the resonance frequency of the 1.2 μm bubbles decreased from around 30 MHz to 20 MHz, then the great amount of subharmonic observed from this population could be attributed to the oscillation of resonant bubbles excited at their resonance frequencies.

It should be noted that the effect of concentration of microbubbles on the backscattered signals has not been investigated in this work. However, an increase in the bubble concentration would result in a higher attenuation and potentially

multiple scattering, as described in section 1.5.4 and 1.5.5. This, in turn, can change the frequency content of the received signals depending on the size distribution and thus the resonance frequency of the bubble population. In order to minimize the attenuation and multiple scattering effects, the concentration of each bubble population (as indicated in section 3.2.6) was chosen based on the published data (Goertz et al. 2003).

3.4.3 Subharmonic as a function of transmit Frequency

In order to find the optimal transmit frequency for each bubble populations, the subharmonic to fundamental ratio was measured over a wide range of transmit frequencies, 12 to 60 MHz. The results in section 3.3.4 showed that the bubble population alteration improved the subharmonic to fundamental ratio.

The numerical simulations in section 2.8.3 showed the frequency range at which the maximum subharmonic to fundamental signal is expected. This frequency range is shifted up with decreasing the bubble size which in turn, increases the bubble resonant frequency. The experimental results (Figure 3-12) showed the same trend with the simulation, demonstrating an increase in the optimal transmit frequency as a result of bubble population alteration. The 1.2 μm filtered bubbles, with the measured resonance frequency of 30 to 40 MHz,

exhibited the greatest subharmonic to fundamental ratio around 20 MHz and maintain constant over a wide range of frequencies. However, the 2 μm filtered and native populations, with the measured resonance frequency of 12 MHz and 15 to 22 MHz respectively, have peaks around 12 MHz. Therefore, subharmonic generation is linked to the resonance size of bubbles.

The optimal transmit frequency of 20 MHz can be suggested for the altered bubble populations which is consistent with the published data (Cheung et al. 2007). At higher transmit frequencies, as described in section 3.4.4, the scattering strength of all the three populations was significantly reduced although the subharmonic to fundamental ratio remained high. The high ratio of subharmonic to fundamental at frequencies above 30 MHz can be potentially attributed to the resonant oscillation of submicron bubbles.

3.4.4 Subharmonic as a function of transmit Pressure at 20 MHz and 40 MHz

In order to characterize the subharmonic signal for 1.2 μm and 2 μm filtered and native populations, the transmit pressure was varied between 35 kPa and 1.2 MPa at 20 and 40MHz. The experimental results supported the hypothesis that the bubble population alteration can maximize the subharmonic signal from

Definity™. It was concluded by the observation of greater subharmonic to fundamental ratios from the 1.2 μm filtered bubble population (Figure 3-14).

The fundamental energy increased with the transmit pressure for various bubble size distributions. However, the subharmonic and fundamental signals scattered by bubbles at 40 MHz were less than those at 20 MHz (Figure 3-13). The result suggests that the bubble size distributions chosen for the present work are not efficient for scattering at higher frequencies (>40 MHz). This conclusion can be explained by the theory as described in section 2.2.7, the bubbles excited at their resonance frequency are the most efficient sound scatterers. When bubbles are excited above their resonance frequency ($\Omega \gg 1$), their scattering does not depend on the excitation frequency and it increases with R_0^2 . By increasing the transmit frequency potentially above 40 MHz, the majority of the bubbles are expected to oscillate off-resonance. This is the reason why the scattering energy of all the three bubble populations is reduced compared with the results at 20 MHz transmit frequency (comparing top, a) and b) with bottom rows, c) and d) of Figure 3-13). The largest scattering measured for the native population showed the size dependency of the off-resonant scattering (Figure 3-13).

The three stages of subharmonic generation: the onset, rapid growth and saturation (section 1.8.3) have been previously reported for the subharmonic signal at low frequencies (Shi, Forsberg et al. 1999). At high frequencies, the

onset of subharmonic signal has not been observed previously since the transmit pressure used in these studies was high (>130 kPa) (Goertz et al. 2006b and Cheung et al. 2007). The saturation is due to the slower growth of the subharmonic signal as the fundamental increases with the transmit pressure. In the present work, patterns resembling these three stages were observed at 20 MHz (Figure 3-13, a): the onset, below 100 kPa, the rapid growth, between 100 kPa and 400 kPa, and the saturation, above 400 kPa. The observation of the rapid growth and saturation regions is consistent with the previous study of Definity™ subharmonic response at high frequency (Cheung et al. 2007). The saturation region was not seen at 40 MHz since the growth rate of the fundamental is slower than that of the subharmonic.

The numerical simulations of Keller-Miksis model in section 2.8.4 showed that bubbles of any size can generate subharmonics if the pressure threshold is exceeded. This was supported experimentally by the observation of the subharmonic signals from all the three bubble populations (Figure 3-13 and 3-14). The model predicts a minimum pressure threshold for the subharmonic generation of a single bubble excited at twice its resonant frequency. Based on this theory, at 20 MHz the highest subharmonic level was calculated for a 2 μm bubble with a resonance frequency of 10 MHz. Unlike the theory, the experimental results (Figure 3-14) showed that the greatest subharmonic to fundamental ratio was achieved by 1.2 μm filtered bubbles. With the same reasoning as described in

section 3.4.2, it can be speculated that the observation of the greatest subharmonic ratio for the 1.2 μm filtered bubble population is due to the resonant oscillations of these bubbles excited at their resonance frequency.

The optimal pressure range for all the three bubble populations can be defined within the saturation region between 400 kPa to 600 kPa. This range is still below the pressure threshold for the bubble destruction (Needles et al. 2005). The result for the optimal pressure range is consistent with the published data (Cheung et al. 2007).

3.5 Summary

The experimental results supported the hypothesis that the bubble population alteration can improve the subharmonic generation from Definity™ microbubbles. The resonant behaviour of various bubble populations was investigated over a wide range of high frequencies. Due to their resonance activity, smaller bubbles exhibited a peak in their attenuation coefficient at higher frequencies and therefore, a potential for nonlinear oscillations within the high frequency range. The subharmonic signal showed a dependency on the transmit parameters and the bubble size distribution. The optimal transmit pressures and

frequencies could be deducted from the experiments for each bubble population. The greatest subharmonic to fundamental ratio was produced by bubbles smaller than 1.2 μm in diameter and under transmit pressure of 400 to 600 kPa at 20 MHz. These bubbles are likely responsible for most of the nonlinear scattering and can be good candidates for subharmonic imaging at high frequencies.

Chapter 4

Discussion and Future Work

Subharmonic imaging can be used to suppress the surrounding tissue signal in order to detect the microvessels. Tissue suppression is done by increasing the contrast of the echoes from blood, carrying microbubbles, with respect to tissue. This is possible through the use of subharmonics which can only be produced by resonance of the bubbles; as opposed to harmonics that can also be created by nonlinear propagation in a medium. The subharmonic generation from microbubbles has been previously used to detect the microvasculature in the rabbit ear (Goertz et al. 2005a). In addition, the feasibility of flow imaging at high frequency using subharmonics has been verified *in vivo* (Goertz et al. 2005b, Needles et al. 2008).

While the efficiency of second harmonic imaging is blurred by the nonlinear propagation of sound in surrounding tissues and the frequency-dependent attenuation, subharmonic imaging seems to be a promising tool. The research is on going to optimize the subharmonic signal at high frequencies.

4.1 Optimization of Subharmonic Imaging

The nonlinear behaviour of Definity™ microbubbles has been attributed to the resonance oscillations of submicron bubbles at high frequencies (Goertz et al. 2003 and 2005a). Based on this finding, there have been some attempts to optimize high frequency nonlinear imaging by isolating submicron bubbles from native bubble population and by changing the transmit conditions (Goertz et al. 2001, 2003; Cheung et al. 2008).

The origin of subharmonic has not been well understood yet. Based on the present work, there is a correlation between the resonance frequency of the bubble population and the frequency at which the maximum subharmonic to fundamental ratio occurred. In addition, the greatest subharmonic to fundamental ratio was observed for microbubbles less than 1.2 μm in diameter. This suggests that the nonlinear oscillations of submicron bubbles, excited around their resonant frequency is likely responsible for the subharmonic generation at high frequencies.

Regardless of the origin of subharmonics, developing a high frequency subharmonic imaging system requires a knowledge of optimized transmit parameters and nonlinear behaviour of the current contrast agents at high frequencies. The high frequency transducers need to be designed with larger

bandwidth to be able to transmit at fundamental and receive at subharmonic. Analog transmit and receive filters are required to modify the current commercial high frequency imaging system, such as the Vevo 770™, for the purpose of subharmonic imaging.

4.2 Future Contrast Agent

The current contrast agents have not been designed for use in imaging at high frequencies. Unlike contrast agents for other imaging modalities, ultrasound contrast agents can be modified according to the technique used to image them. Submicron lipid shelled bubbles are suitable candidates for the nonlinear imaging at high frequencies. The resonance behaviour of these bubbles has been hypothesized to produce strong nonlinear scattering at high frequencies (Goertz et al. 2001, Goertz et al. 2005a and Cheung et al. 2008).

Definity™ has a significant number of bubbles with diameters of 1 to 2 μm and below. However, the volume fraction of the subpopulation of submicron bubbles is small. Therefore, the majority of bubbles oscillate off their resonance frequency and do not contribute efficiently for high frequency imaging (Goertz, Frijlink et al. 2004). It emphasizes the need to gain quantitative insights into an

appropriate bubble size distribution with a resonant behaviour at high frequencies and also to develop the appropriate scattering models to incorporate the effects which the present models can not take into account. This knowledge leads to developing new contrast agents for nonlinear imaging at high frequencies.

Using smaller bubbles, assuming a given volume fraction of gas, means having a larger number of bubbles per unit volume. Thereby, a higher bubble number density can be achieved in the blood vessels. This is an important factor when volume of blood within the sample volume decreases according to the scale of microvasculature and high frequency ultrasound beam. Therefore, a higher bubble number density within the agent increases the probability of the presence of bubbles within the sample volume (Goertz et al. 2006b and Goertz, Frijlink et al. 2004).

The results of the present work showed that for the subharmonic imaging at high frequency, the size of bubbles should be smaller than 1.2 μm in diameter. This is the size distribution by which a maximum subharmonic was detected over a wide range of transmit frequencies. However, manufacturing stable bubbles smaller than 1 μm in diameter is challenging. The increased surface area to volume ratio reduces the lifetime of bubbles. Moreover, the thickness of the shell limits the minimum achievable size of bubbles.

4.3 *In vivo* Subharmonic Imaging

It is important to discuss the differences in the behaviour and kinetics of microbubbles in *in vitro* and *in vivo* environments. After an intravenous injection of microbubbles, not all microbubbles entering the pulmonary circulation circulate. The lung capillaries with an average diameter of 7 μm filter the larger bubbles passively (Bouakaz et al. 1998). However, due to the rhythmic variation of diameter of the capillaries, the new altered size distribution of these bubbles can not simply be predicted by their average diameter. In addition, active filtration mechanisms such as proteolysis¹⁰ and intravascular phagocytosis¹¹ result in trapping and removal of microbubbles from the pulmonary circulation (Brain et al. 1977). Although, there is some evidence of deformation of lipid shell microbubbles (such as Definity™) during the transient entrapment which allows their safe passage through the capillaries (Lindner et al. 2002).

Other *in vivo* factors affecting the size distribution of microbubbles include the outward gas diffusion and ambient pressure which result in the bubble shrinkage and therefore, yielding a population of smaller bubbles. After passage

¹⁰ Proteolysis is the directed degradation of proteins by cellular enzymes or by intramolecular digestion.

¹¹ Phagocytosis is a cellular process of absorbing waste material or other foreign bodies in the bloodstream and tissues.

through the lungs, the agent travels through the left atrium and the left ventricle. The left ventricle forces the agent through the systolic circulation by exerting an almost 120 mmHg pressure on it. This ambient pressure, in turn, accelerates the rate of the bubble shrinkage (Bouakaz et al. 1998 and de Jong et al. 1993b).

The nonlinear behaviour of the bubbles, survived during the passage through the pulmonary circulation can be affected due to dampening of bubble oscillations in blood. The viscosity of blood is about 3.5×10^{-3} Pas at 36°C and 40% hematocrit, compared with 1×10^{-3} Pas for water at 20°C (Cobbold 2007). Therefore, higher transmit pressures and longer pulses may be required to initiate the subharmonic generation *in vivo* (Shankar et al. 1999). In addition, the passage of bubbles through small vessels can limit their large radial oscillations (Caskey, Dayton et al. 2005, Cheung et al. 2007).

4.4 Conclusion

The alteration of various bubble populations was investigated as a possible way to improve the subharmonic generation from Definity™ microbubbles. The simulations showed that the subharmonic generation from a single bubble can increase depending on the bubble size and the transmit parameters. Specifically, a decrease in the bubble diameter can improve subharmonic generation at high frequency. The filtration of native Definity™ provided a subpopulation of smaller

bubbles, resonating at high frequencies. The behaviour of each population was examined over 10 to 60 MHz. The altered population of smaller bubbles demonstrated resonance behaviour and thus, their potential for the nonlinear oscillations at higher frequencies. The transmit conditions including pressure and frequency were varied to maximize the subharmonic signal, generated by each population. For the transmit frequencies between 12 to 60 MHz, microbubbles less than 1.2 μm in diameter produced the greatest subharmonic to fundamental ratio, with a peak around 20 MHz. Over the transmit pressure range of 35 kPa to 1.2 MPa, the greatest ratio of subharmonic to fundamental was obtained by microbubbles less than 1.2 μm at 20 MHz and 40 MHz. An optimal transmit pressure range of 400 to 600 kPa was suggested for all the selected bubble populations. The nonlinear oscillations of resonant bubbles excited at their resonance frequency were proposed to be a feasible origin of subharmonic at high frequency.

In this work the subharmonic signal for Definity™ contrast agent was characterized at high frequencies. The alteration of Definity™ population improved the subharmonic generation *in vitro* at high frequency. The experimental results are in general agreement with the theoretical predictions.

Appendix A: Equations required for derivation of Keller-Miksis Model

Equations of motion for the liquid are derived based on the conservation of mass (equation of continuity), the conservation of momentum (Euler equation) and the equation of state for the liquid.

Equation of Continuity

A volume element of dV_1 is considered to be fixed within the fluid. The equation of continuity states that the fluid mass is neither created nor destroyed within dV_1 . The rate of change in mass (within this volume) is either due to the mass flux of fluid crossing the surface of the volume element or due to the local changes in density.

$$-\int_v \dot{\rho} dV = \oint_s \rho \vec{v} \cdot d\vec{S} \quad (\text{A.1})$$

where \vec{v} is the fluid particle velocity. According to Gauss' theorem:

$$\oint_s (\rho \vec{v}) \cdot d\vec{S} = \oint_v \vec{\nabla} \cdot (\rho \vec{v}) dV \quad (\text{A.2})$$

Equation A.2 can be rewritten as the equation of continuity:

$$\dot{\rho} + \vec{\nabla} \cdot (\rho \vec{v}) = 0 \quad (\text{A.3})$$

Equations of State

The equations of state, Equations (A.4), set a relation between changes in pressure p , density ρ and enthalpy h per unit mass of the liquid. Constant entropy is assumed. The process is considered to be adiabatic in the surrounding medium which is a common assumption in acoustics, shown by the index S (Hoff 2001):

$$\begin{aligned} \left(\frac{\partial \rho}{\partial p} \right)_s &= \frac{1}{c^2} \\ \left(\frac{\partial h}{\partial p} \right)_s &= \frac{1}{\rho} \end{aligned} \quad (\text{A.4})$$

Euler's Equation

Newton's Second Law states that the resulting rate of change in the momentum (the product of the body's mass, m , and velocity, \vec{v}) of a body as a force acts on the body is equal to the force. If the volume and the density of the body are considered constant, then the force is equal to the product of ρdV with the rate of change of \vec{v} , \vec{a} . If the volume element is moving with the flow, \vec{v}

changes as the liquid velocity changes not only with time at any given fixed position but also with position at any given fixed time. Applying Newton's Second Law under the assumption of ignoring viscous and thermal conduction effects (Leighton 1994):

$$\left(\rho\vec{g} - \vec{\nabla}p(\vec{r},t)\right)dV = \rho dV \cdot \vec{a} \quad (\text{A.5})$$

where \vec{g} is a vector of gravitational acceleration; $\left(-\vec{\nabla}p(\vec{r},t)\right)dV$ is the instantaneous force due to the unbalanced liquid pressure and \vec{a} is the acceleration of the body.

Considering gravity as the only body force potential energy per unit mass of liquid, ϕ_B which is equal to $g \cdot h$, the force per unit volume is given by:

$$-\vec{\nabla}p - \rho\vec{\nabla}\phi_B = \rho\vec{a} \quad (\text{A.6})$$

$$\vec{a} = \frac{\Delta(\vec{v}_t + \vec{v}_r)}{\Delta t} = \vec{\dot{v}} + (\vec{v} \cdot \vec{\nabla})\vec{v} \quad (\text{A.7})$$

where $\vec{\dot{v}} = \left(\partial\vec{v}/\partial t\right)_{\vec{r}}$. Replacing Equation (A.7) in Equation (A.6) gives Euler's equation:

$$-\vec{\nabla}p(\vec{r},t) = \rho\left(\vec{\dot{v}} + (\vec{v} \cdot \vec{\nabla})\vec{v} + \vec{\nabla}\phi_B\right) \quad (\text{A.8})$$

When the flow is irrotational, Φ can be defined as the velocity potential and $\vec{v} = \vec{\nabla}\Phi$. Integrating Euler equation from an arbitrary position r to infinity and

knowing that the velocity potential and the enthalpy are zero at $r=\infty$, Bernoulli equation can be obtained:

$$\frac{\partial\Phi}{\partial t} + \frac{1}{2}(\nabla\Phi)^2 + h(r) = 0 \quad (\text{A.9})$$

Appendix B: Output pressure characterization of the RMV-710B™ and RMV-708™

The RMV-710B and RMV-708 transducers were characterized by a 40-micron needle hydrophone (Precision Acoustics, Dorset, UK), calibrated up to 60 MHz by the NPL (National Physical Laboratories, Teddington, UK). Figure B-1 illustrates a simple schematic of the hydrophone measurements. The needle hydrophone measures the output pressure of the transducer at the focus. This hydrophone is attached to a submersible amplifier which buffers the signal. Power is provided by a DC coupler to the submersible preamplifier. It also acts as an acoustic signal coupler between the preamplifier and the user's measurements system. The signal is further amplified by the hydrophone booster amplifier which can be shown and recorded by using the oscilloscope. The narrowband output peak negative pressure of the transducers was measured from 35 kPa up to 1.2 MPa for a frequency range of 10 to 60 MHz as shown in Figure B-2 and B-3.

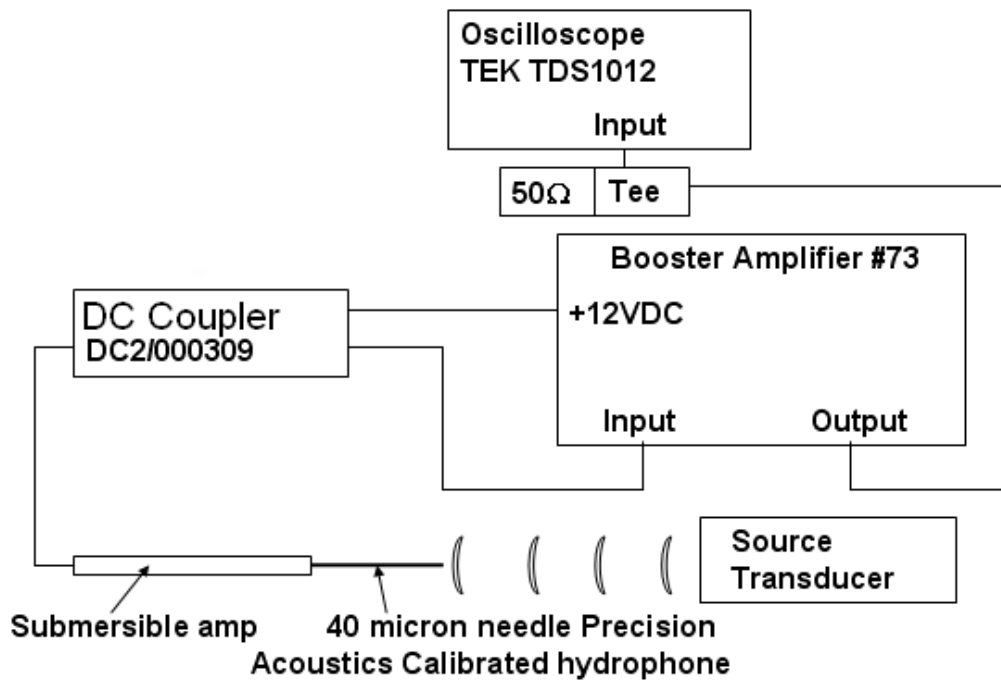


Figure B-1 A schematic of the hydrophone measurements in order to characterize the Vevo 770™ transducers. The 40 micron needle hydrophone measures the output pressure at the focus of each transducer.

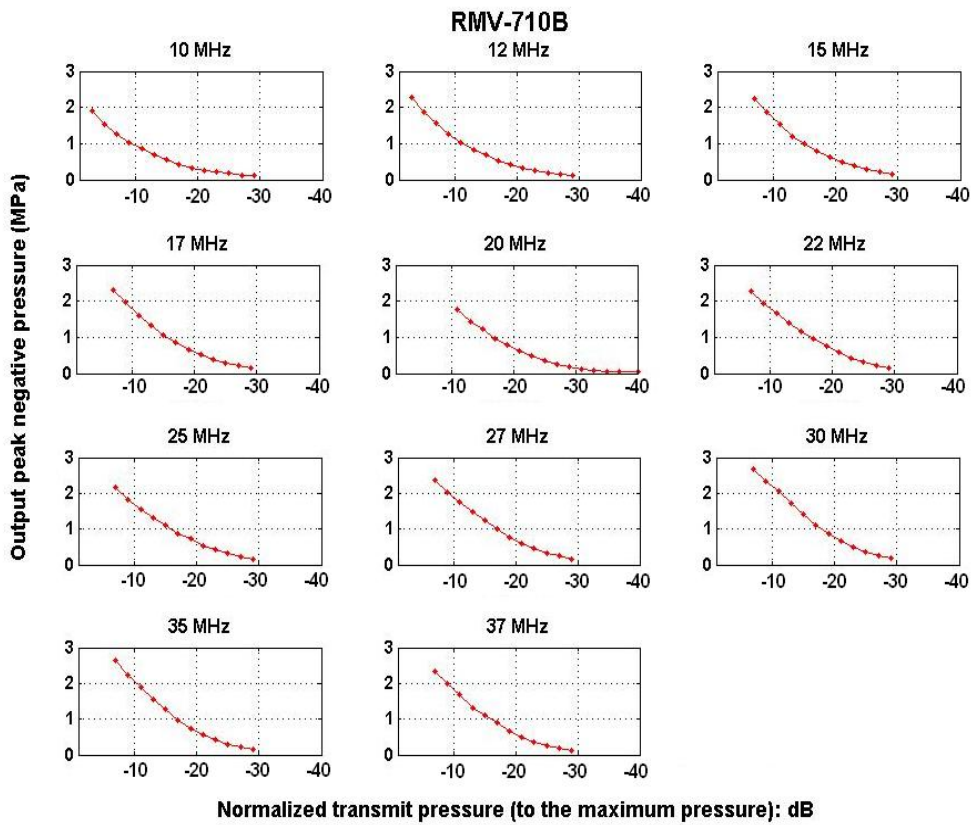


Figure B-2 The hydrophone measurements of RMV-710B for a 20-cycle rectangular pulse at different frequencies. The output peak negative pressure is shown as a function of normalized transmit pressures.

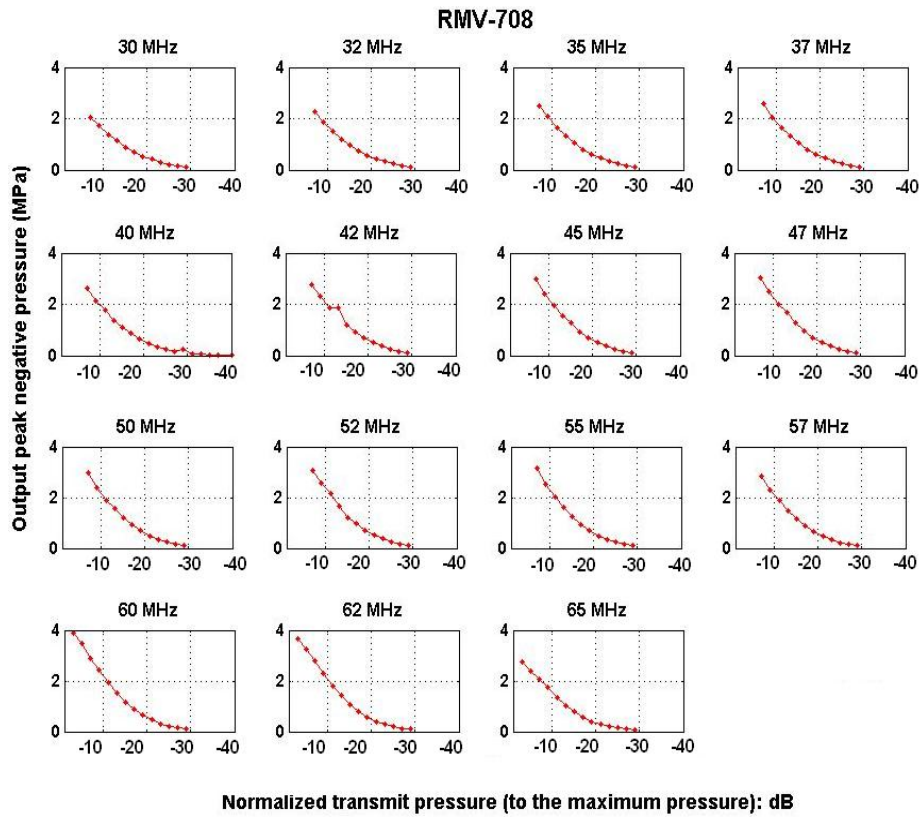


Figure B-3 The hydrophone measurements of RMV-708 for a 20-cycle rectangular pulse at different frequencies. The output peak negative pressure is shown as a function of normalized transmit pressures.

Bibliography

- Angelsen, B. A. J., Johansen, T. F., & Hoff, L. (1999). Simulation of gas bubble scattering for large mach-numbers., *Ultrasonic symposium, Proceedings IEEE*, 1, 505-508.
- Averkiou, M. A., Roundhill, D. N., & Powers, J. E. (1997). New imaging technique based on the nonlinear properties of tissues., *Ultrasonic symposium, Proceedings IEEE*, 2, 1561-1566.
- Becher, H., & Burns, P. N. (2000). Contrast agents for echocardiography: Principles and instrumentation. *Handbook of Contrast Echocardiography*, 184.
- Biagi, E., Breschi, L., Vannacci, E., & Masotti, L. (2007). Stable and transient subharmonic emissions from isolated contrast agent microbubbles. *IEEE Transactions on Ultrasonics, Ferroelectrics, and Frequency Control*, 54(3), 480-497.
- Bohn, L. (1957). Acoustic pressure variation and the spectrum in oscillatory cavitation. *Acustica*, 7, 201-216.

- Bom, N., Ten Hoff, H., Lancee, C. T., Gussenhoven, W. J., & Bosch, J. G. (1989). Early and recent intraluminal ultrasound devices. *International Journal of Cardiac Imaging*, 4(2-4), 79-88.
- Bouakaz, A., De Jong, N., Cachard, C., & Jouini, K. (1998). On the effect of lung filtering and cardiac pressure on the standard properties of ultrasound contrast agent. *Ultrasonics*, 36(1-5), 703-708.
- Brain, J. D. (1977). Anesthesia and respiratory defense mechanisms. *International Anesthesiology Clinics*, 15(2), 169-198.
- Brayman, A. A., Azadniv, M., Miller, M. W., & Meltzer, R. S. (1996). Effect of static pressure on acoustic transmittance of albutex® microbubble suspensions. *Journal of the Acoustical Society of America*, 99(4 I), 2403-2408.
- Carroll, B. A., Turner, R. J., & Tickner, E. G. (1980). Gelatin encapsulated nitrogen microbubbles as ultrasonic contrast agents. *Investigative Radiology*, 15(3), 260-266.
- Caskey, C. F., Kruse, D. E., Dayton, P. A., & Ferrara, K. W. (2005). On the oscillations of microbubbles in tubes with diameters as small as 12 microns. *Ultrasonic symposium IEEE*, 2, 854-857.

- Chang, P. H., Shung, K. K., Wu, S., & Levene, H. B. (1995). Second harmonic imaging and harmonic doppler measurements with albunex. *IEEE Transactions on Ultrasonics, Ferroelectrics, and Frequency Control*, 42(6), 1020-1027.
- Chen, J., & Zhu, Z. (2006). Ultrasound attenuation in encapsulated microbubble suspensions: The multiple scattering effects. *Ultrasound in Medicine and Biology*, 32(6), 961-969.
- Cheung, A. M. Y., Brown, A. S., Cucevic, V., Roy, M., Needles, A., Yang, V., et al. (2007). Detecting vascular changes in tumour xenografts using micro-ultrasound and micro-CT following treatment with VEGFR-2 blocking antibodies. *Ultrasound in Medicine and Biology*, 33(8), 1259-1268.
- Cheung, K., Couture, O., Bevan, P. D., Cherin, E., Williams, R., Burns, P. N., et al. (2008). In vitro characterization of the subharmonic ultrasound signal from Definity microbubbles at high frequencies. *Physics in Medicine and Biology*, 53(5), 1209-1223.
- Chin, C.T. (2001). Modeling the behavior of microbubble contrast agents for diagnostic ultrasound, PhD thesis, University of Toronto, Toronto, Canada.

- Chômas, J. E., Dayton, P., Alien, J., Morgan, K., & Ferrara, K. W. (2001). Mechanisms of contrast agent destruction. *IEEE Transactions on Ultrasonics, Ferroelectrics, and Frequency Control*, 48(1), 232-248.
- Church, C. C. (1995). The effects of an elastic solid surface layer on the radial pulsations of gas bubbles. *Journal of the Acoustical Society of America*, 97(3), 1510-1521.
- Church, C. C., & Yang, X. (2006). A theoretical study of gas bubble dynamics in tissue. *Innovations in Nonlinear Acoustics: ISNA17, AIP Conference Proceedings*, 838 217-224.
- Cobbold, R. S. C. (2007). *Foundations of biomedical ultrasound*. Toronto: Oxford University Press.
- Commander, K. W., & Prosperetti, A. (1989). Linear pressure waves in bubbly liquids: Comparison between theory and experiments. *J. Acoust. Soc. Am.*, 85(2), 732-746.
- Cosgrove, D. O., Blomley, M. J. K., Jayaram, V., & Nihoyannopoulos, P. (1998). Echo-enhancing (contrast) agents. *Ultrasound Quarterly*, 14(2), 66-75.
- Cuccia, D. J., Bevilacqua, F., Durkin, A. J., Merritt, S., Tromberg, B. J., Gulsen, G., et al. (2003). In vivo quantification of optical contrast agent dynamics in

- rat tumours by use of diffuse optical spectroscopy with magnetic resonance imaging coregistration. *Applied Optics*, 42(16), 2940-2950.
- De Jong, N. (1993). Acoustic properties of ultrasound contrast agents, PhD thesis, Erasmus University, Rotterdam.
- De Jong, N., Bouakaz, A., & Frinking, P. (2002). Basic acoustic properties of microbubbles. *Echocardiography*, 19(3), 229-240.
- De Jong, N., Cornet, R., & Lancée, C. T. (1994). Higher harmonics of vibrating gas-filled microspheres. part one: Simulations. *Ultrasonics*, 32(6), 447-453.
- De Jong, N., Hoff, L. (1993a). Ultrasound scattering properties of Alunex microspheres. *Ultrasonics*, 31(3), 175-181.
- De Jong, N., Hoff, L., Skotland, T., & Bom, N. (1992). Absorption and scatter of encapsulated gas filled microspheres: Theoretical considerations and some measurements. *Ultrasonics*, 30(2), 95-103.
- De Jong, N., Ten Cate, F. J., Vletter, W. B., & Roelandt, J. R. T. C. (1993b). Quantification of transpulmonary echocontrast effects. *Ultrasound in Medicine and Biology*, 19(4), 279-288.
- De Kroon, M. G. M., Slager, C. J., Gussenhoven, W. J., Serruys, P. W., Roelandt, J. R. T. C., & Bom, N. (1991). Cyclic changes of blood echogenicity in high-frequency ultrasound. *Ultrasound in Medicine and Biology*, 17(7), 723-728.

- Devin, C. (1959). Survey of thermal, radiation, and viscous damping of pulsating air bubbles in water. *J. Acoust. Soc. Am.*, 31(12), 1654-1667.
- Duck, F. A. (2002). Nonlinear acoustics in diagnostic ultrasound. *Ultrasound in Medicine and Biology*, 28(1), 1-18.
- Ellegala, D. B., Leong-Poi, H., Carpenter, J. E., Klibanov, A. L., Kaul, S., Shaffrey, M. E., et al. (2003). Imaging tumour angiogenesis with contrast ultrasound and microbubbles targeted to $\alpha_v\beta_3$. *Circulation*, 108(3), 336-341.
- Eller A., & Flynn H.G. (1969). Generation of subharmonics of order one-half by bubbles in a sound field. *Journal of the Acoustical Society of America*, 46(3 pt 2), 722-727.
- Eller, A. I. (1970). Damping constants of pulsating bubbles. *J. Acoust. Soc. Am.*, 47, 1469-1470.
- Emmer, M., van Wamel, A., Goertz, D. E., & de Jong, N. (2007). The onset of microbubble vibration. *Ultrasound in Medicine and Biology*, 33(6), 941-949.
- Esche, R. (1952). Untersuchung der schwingungskavitation in flüssigkeiten. *Acustica*, 2(AB), 208-218.
- Falou, O., (2006). Finite-element modeling of acoustic wave scattering from rigid, fluid and elastic spheres., MSc. Thesis, Ryerson University, Toronto.

- Faraday, M. (1831). On the forms and states assumed by fluids in contact with vibrating elastic surfaces. *Philos. Trans. R. Soc. London*, 121, 319-340.
- Feinstein, S. B., Shah, P. M., & Bing, R. J. (1984). Microbubble dynamics visualized in the intact capillary circulation. *Journal of the American College of Cardiology*, 4(3), 595-600.
- Feng, Z. C., & Leal, L. G. (1997). Nonlinear bubble dynamics, *Annual Review of Fluid Mechanics*, 29, 201-243
- Folkman, J. (1971). Tumor angiogenesis: Therapeutic implications. *New England Journal of Medicine*, 285(21), 1182-1186.
- Fontaine I. and Cloutier G. (2003). Modeling the frequency dependence (5–120 MHz) of ultrasound backscattering by red cell aggregates in shear flow at a normal hematocrit. *The Journal of the Acoustical Society of America*, 113 (5), 2893-2900.
- Foster, F. S., Pavlin, C. J., Harasiewicz, K. A., Christopher, D. A., & Turnbull, D. H. (2000). Advances in ultrasound biomicroscopy. *Ultrasound in Medicine and Biology*, 26(1), 1-27.
- Frijlink, M. E., Goertz, D. E., Bouakaz, A., & van der Steen, A. F. W. (2006). Intravascular ultrasound tissue harmonic imaging: A simulation study. *Ultrasonics*, 44(SUPPL.), e185-e188.

- Frijlink, M. E., Goertz, D. E., Foster, F. S., & Van Der Steen, A. F. W. (2003). High frequency harmonic imaging in presence of intravascular stents., *Ultrasonic IEEE Symposium*, 1, 208-211.
- Frinking, P. J. A., Bouakaz, A., Kirkhorn, J., Ten Cate, F. J., & De Jong, N. (2000). Ultrasound contrast imaging: Current and new potential methods. *Ultrasound in Medicine and Biology*, 26(6), 965-975.
- Frinking, P. J. A., & De Jong, N. (1998). Acoustic modeling of shell-encapsulated gas bubbles. *Ultrasound in Medicine and Biology*, 24(4), 523-533.
- Fung, Y. C. (1997). *Biomechanics: Circulation* (2nd ed.). New York: Springer.
- Goertz, D. E. (2002). High frequency ultrasound imaging of the microcirculation, PhD thesis, University of Toronto, Toronto, Canada.
- Goertz, D. E., Cherin, E., Needles, A., Karshafian, R., Brown, A. S., Burns, P. N., et al. (2005a). High frequency nonlinear B-scan imaging of microbubble contrast agents. *IEEE Transactions on Ultrasonics, Ferroelectrics, and Frequency Control*, 52(1), 65-79.
- Goertz, D. E., Christopher, D. A., Yu, J. L., Kerbel, R. S., Burns, P. N., & Foster, F. S. (2000). High-frequency color flow imaging of the microcirculation. *Ultrasound in Medicine and Biology*, 26(1), 63-71.

- Goertz, D. E., de Jong, N., & van der Steen, A. F. W. (2007). Attenuation and size distribution measurements of Definity™ and manipulated Definity™ populations. *Ultrasound in Medicine and Biology*, 33(9), 1376-1388.
- Goertz, D. E., Frijlink, M., Bouakaz, A., Chin, C. T., De Jong, N., & Van Der Steen, A. W. F. (2003). The effect of bubble size on nonlinear scattering from microbubbles at high frequencies. *Ultrasonic IEEE Symposium*, 2, 1503-1506.
- Goertz, D. E., Frijlink, M. E., De Jong, N., & Van Der Steen, A. (2004). High frequency nonlinear scattering and imaging of a submicron contrast agent. *Ultrasonic IEEE Symposium*, 2, 986-989.
- Goertz, D. E., Frijlink, M. E., De Jong, N., & Van Der Steen, A. (2006a). High frequency nonlinear scattering and imaging of a micrometer to submicrometer sized lipid encapsulated contrast agent. *Ultrasound in Medicine & Biology*, 32(4), 569-577.
- Goertz, D. E., Frijlink, M. E., Tempel, D., Van Damme, L. C. A., Krams, R., Schaar, J. A., et al. (2006b). Contrast harmonic intravascular ultrasound: A feasibility study for vasa vasorum imaging. *Investigative Radiology*, 41(8), 631-638.

- Goertz, D. E., Needles, A., Burns, P. N., & Foster, F. S. (2005b). High-frequency, nonlinear flow imaging of microbubble contrast agents. *IEEE Transactions on Ultrasonics*, 52(3), 495-502.
- Goertz, D. E., Wong, S. W. S., Cherin, E., Chin, C. T., Burns, P. N., & Foster, F. S. (2001). Non-Linear Scattering Properties of Microbubble Contrast Agents at High Frequencies, *Ultrasonic Symposium IEEE*, 2, 1747-1750.
- Gramiak, R., & Shah, P. M. (1968). Echocardiography of the aortic root. *Investigative Radiology*, 3(5), 356-366.
- Greenblatt, M., & Shubi, P. (1968). Tumor angiogenesis: Transfilter diffusion studies in the hamster by the transparent chamber technique. *Journal of the National Cancer Institute*, 41(1), 111-124.
- Hlatky, L., Hahnfeldt, P., & Folkman, J. (2002). Clinical application of antiangiogenic therapy: Microvessel density, what it does and doesn't tell us. *Journal of the National Cancer Institute*, 94(12), 883-893.
- Hoff, L. (2001). *Acoustic Characterization of Contrast Agents for Medical Ultrasound Imaging*. Dordrecht, The Netherlands, Kluwer Academic Publishers.

- Hoff, L., Sontum, P. C., & Hoff, B. (1996). Acoustic properties of shell-encapsulated, gas-filled ultrasound contrast agents. *Ultrasonic IEEE Symposium*, 2 1441-1444.
- Hoffmann, K., El Gammal, S., Matthes, U., & Altmeyer, P. (1989). Digital 20 MHz ultrasonography of the skin as a tool in preoperative diagnostics. *H & G: Zeitschrift Fur Hautkrankheiten*, 64(10), 851-858.
- Hoffmann, K., El-Gammal, S., & Altmeyer, P. (1990). B-scan-sonography in dermatology. *Hautarzt*, 41(9), W7-W16.
- Huang, D., Swanson, E.A., Lin, C.P., Schuman, J.S., Stinson, W.G., Chang, W., Hee, M.R., Flotte, T., Gregory, K., Puliafito, C.A., (1991). Optical Coherence Tomography, *Science*, 254, 1178-1181, 1991.
- Jain, R. K. (1988). Determinants of tumor blood flow: A review. *Cancer Research*, 48(10), 2641-2658.
- Karchakdjian, R. (2001). Modelling the structure of the tumour vasculature and its effect on Doppler ultrasound signals, University of Toronto, Toronto, Canada, 2001.
- Kargl, S. G. (2002). Effective medium approach to linear acoustics in bubbly liquids. *Journal of the Acoustical Society of America*, 111(1 I), 168-173.

- Keller, J. B., & Kolodner, I. I. (1956). Damping of underwater explosion bubble oscillations. *Journal of Applied Physics*, 27(10), 1152-1161.
- Keller, J. B., & Miksis, M. (1980). Bubble oscillations of large amplitude. *Journal of the Acoustical Society of America*, 68(2), 628-633.
- Kerbel, R. S. (2000). Tumor angiogenesis: Past, present and the near future. *Carcinogenesis*, 21(3), 505-515.
- Kincaid, D., & Cheney, W. (1996). *Numerical Analysis*, Second edition.
- Kincaid, D. (2002). In Cheney E. W. (Ed.), *Numerical analysis: Mathematics of scientific computing* (3rd ed.). Pacific Grove, Calif.: Brooks/Cole.
- Kinsler, L. E., Frey, A. R., Coppens, A. B., & Sanders, J. V. (1982). *Fundamentals of acoustics*. Third edition.
- Kruse, D. E., & Ferrara, K. W. (2002). A new high resolution color flow system using an Eigen decomposition-based adaptive filter for clutter rejection. *IEEE Transactions on Ultrasonics, Ferroelectrics, and Frequency Control*, 49(10), 1384-1399.
- Kruse, D. E., Lim, M. C., Redline, D. E., Eisele, P. H., & Ferrara, K. W. (2002). High frequency ultrasound with an eigen-decomposition filter to assess the

- effect of laser cyclophotocoagulation treatment on blood flow. *IEEE Ultrasonic Symposium*, 2, 1485-1489.
- Lanza, G. M., Trousil, R. L., Wallace, K. D., Rose, J. H., Hall, C. S., Scott, M. J., et al. (1998). In vitro characterization of a novel, tissue-targeted ultrasonic contrast system with acoustic microscopy. *Journal of the Acoustical Society of America*, 104(6), 3665-3672.
- Lanza, G. M., Wallace, K. D., Scott, M. J., Cacheris, W. P., Abendschein, D. R., Christy, D. H., et al. (1996). A novel site-targeted ultrasonic contrast agent with broad biomedical application. *Circulation*, 94(12), 3334-3340.
- Lauterborn, W. (1976). Numerical investigation of nonlinear oscillations of gas bubbles in liquids. *Journal of the Acoustical Society of America*, 59(2), 283-293.
- Lauterborn, W., & Cramer, E. (1981). Subharmonic route to chaos observed in acoustics. *Physical Review Letters*, 47(20), 1445-1448.
- Lauterborn, W., & Holzfuss, J. (1991). Acoustic chaos. *Int. J. Bifurcation and Chaos*, 1(1), 13-26.
- Lauterborn, W., Holzfuss, J., & Billo, A. (1994). Chaotic behaviour in acoustic cavitation. *Proceedings of the IEEE Ultrasonics Symposium*, 2, 801-810.

- Lauterborn, W., Kurz, T., & Parlitz, U. (1997). Experimental nonlinear physics. *Journal of the Franklin Institute*, 334(5-6), 865-907.
- Leighton, T. G. (1994). *The Acoustic Bubble*. Academic Press Ltd., London, UK, 1st edition.
- Leighton, T. G., Lingard, R. J., Walton, A. J., & Field, J. E. (1991). Acoustic bubble sizing by combination of subharmonic emissions with imaging frequency. *Ultrasonics*, 29(4), 319-323.
- Li, J. K. (2004). *Dynamics of the vascular system*. London: World Scientific Pub. Co.
- Lindner, J. R., Song, J., Jayaweera, A. R., Sklenar, J., & Kaul, S. (2002). Microvascular rheology of Definity microbubbles after intra-arterial and intravenous administration. *Journal of the American Society of Echocardiography*, 15(5), 396-403.
- Lockwood, G. R., Ryan, L. K., Gotlieb, A. I., Lonn, E., Hunt, J. W., Liu, P., et al. (1992). In vitro high resolution intravascular imaging in muscular and elastic arteries. *Journal of the American College of Cardiology*, 20(1), 153-160.
- Lotsberg, O., Hovem, J. M., & Aksum, B. (1996). Experimental observation of subharmonic oscillations in infuson bubbles. *Journal of the Acoustical Society of America*, 99(3), 1366-1369.

- McDonald, D. M., & Choyke, P. L. (2003). Imaging of angiogenesis: From microscope to clinic. *Nature Medicine*, 9(6), 713-725.
- Medwin, H. (1977). Counting bubbles acoustically: A review. *Ultrasonics*, 15(1), 7-13.
- Meyer, C. R., Chiang, E. H., Fechner, K. P., Fitting, D. W., Williams, D. M., & Buda, A. J. (1988). Feasibility of high-resolution, intravascular ultrasonic imaging catheters. *Radiology*, 168(1), 113-116.
- Miles, K. A. (1999). Tumour angiogenesis and its relation to contrast enhancement on computed tomography: A review. *European Journal of Radiology*, 30(3), 198-205.
- Miller, J. C., Pien, H. H., Sahani, D., Sorensen, A. G., & Thrall, J. H. (2005). Imaging angiogenesis: Application and potential for drug development. *Journal of the National Cancer Institute*, 97(3), 172-187.
- Minnaert, M. (1933). On musical air-bubbles and the sounds of running water. *Philos. Mag.*, 16, 235-248.
- Muir, T. G., & Carstensen, E. L. (1980). Prediction of nonlinear acoustic effects at biomedical frequencies and intensities. *Ultrasound in Medicine and Biology*, 6(4), 345-357.

- Needles, A., Brown, A. S., Karshafian, R.; Burns, P. N., Foster, F.S., Goertz, D. E., (2005) High frequency subharmonic pulsed-wave doppler and color flow imaging of microbubble contrast agents, *Proceedings - IEEE Ultrasonics Symposium*, 1, 629-632.
- Needles, A., Goertz, D. E., Karshafian, R., Cherin, E., Brown, S. A., Burns, P. N. and Foster F. S., (2008), High frequency subharmonic pulsed-wave Doppler and color flow imaging of microbubble contrast agents, *Ultrasound in Medicine and Biology*, 2008, 34, 7, 1139-1151.
- Neppiras E. A. (1969). Subharmonic and other low-frequency emission from bubbles in sound-irradiated liquids. *Journal of the Acoustical Society of America*, 46(3 pt 2), 587-601.
- Neppiras, E. A. (1980). Acoustic cavitation. *Physics Reports*, 61(3), 159-251.
- Neppiras, E. A., & Noltingk, B. E. (1951). Cavitation produced by ultrasonics: Theoretical conditions for the onset of cavitation. *Proceedings of the Physical Society. Section B*, 64(12), 1032-1038.
- Niemczewski, B. (1980). A comparison of ultrasonic cavitation intensity in liquids. *Ultrasonics*, 18(3), 107-110.
- Nissen, S. E., Grines, C. L., Gurley, J. C., Sublett, K., Haynie, D., Diaz, C., et al. (1990). Application of a new phased-array ultrasound imaging catheter in the

- assessment of vascular dimensions. in vivo comparison to cineangiography. *Circulation*, 81(2), 660-666.
- Noltingk, B. E., & Neppiras, E. A. (1950). Cavitation produced by ultrasonics. *Proceedings of the Physical Society. Section B*, 63(9), 674-685.
- Ntziachristos, V., Yodh, A. G., Schnall, M., & Chance, B. (2000). Concurrent MRI and diffuse optical tomography of breast after indocyanine green enhancement. *Proceedings of the National Academy of Sciences of the United States of America*, 97(6), 2767-2772.
- Parlitz, U., Englisch, V., Scheffczyk, C., & Lauterborn, W. (1990). Bifurcation structure of bubble oscillators. *Journal of the Acoustical Society of America*, 88(2), 1061-1077.
- Pavlin, C. J., Sherar, M. D., & Foster, F. S. (1990). Subsurface ultrasound microscopic imaging of the intact eye. *Ophthalmology*, 97(2), 244-250.
- Phelps, A. D., & Leighton, T. G. (1997). The subharmonic oscillations and combination-frequency subharmonic emissions from a resonant bubble: Their properties and generation mechanisms. *Acustica*, 83(1), 59-66.
- Plesset, M. S. (1949). The dynamics of cavitation bubbles. *J. Appl. Mech.*, 16, 277-282.

- Poritsky, H. (1952). The collapse or growth of a spherical bubble or cavity in a viscous fluid. *Proc First US Natl Congr Appl Mech*, 813-821.
- Prinking, P. J. A., De Jong, N., & Ignacio Céspedes, E. (1999). Scattering properties of encapsulated gas bubbles at high ultrasound pressures. *Journal of the Acoustical Society of America*, 105(3), 1989-1996.
- Rayleigh, L. (1945). *The Theory of Sound*, New York, USA, 2nd edition.
- Rayleigh, L. (1917). On the pressure developed in a liquid during the collapse of a spherical cavity. *Phil. Mag.*, 34(200), 94-98.
- Rohren, E. M., Turkington, T. G., & Coleman, R. E. (2004). Clinical applications of PET in oncology. *Radiology*, 231(2), 305-332.
- Schrope, B. A., & Newhouse, V. L. (1993). Second harmonic ultrasonic blood perfusion measurement. *Ultrasound in Medicine and Biology*, 19(7), 567-579.
- Shankar, P. M., Krishna, P. D., & Newhouse, V. L. (1998). Advantages of subharmonic over second harmonic backscatter for contrast- to-tissue echo enhancement. *Ultrasound in Medicine and Biology*, 24(3), 395-399.
- Shankar, P. M., Krishna, P. D., & Newhouse, V. L. (1999). Subharmonic backscattering from ultrasound contrast agents. *Journal of the Acoustical Society of America*, 106(4 I), 2104-2110.

- Shapiro, J. R., Reisner, S. A., Lichtenberg, G. S., & Meltzer, R. S. (1990). Intravenous contrast echocardiography with use of sonicated albumin in humans: Systolic disappearance of left ventricular contrast after transpulmonary transmission. *Journal of the American College of Cardiology*, 16(7), 1603-1607.
- Sherar, M. D., Starkoski, B. G., Taylor, W. B., & Foster, F. S. (1989). A 100 MHz B-scan ultrasound backscatter microscope. *Ultrasonic Imaging*, 11(2), 95-105.
- Shi, W. T., Forsberg, F., & Goldberg, B. B. (1997). Subharmonic imaging with gas-filled microbubbles. *J. Acoust. Soc. Am*, 101, 3139.
- Shi, W. T., Forsberg, F., Raichlen, J. S., Needleman, L., & Goldberg, B. B. (1999). Pressure dependence of subharmonic signals from contrast microbubbles. *Ultrasound in Medicine & Biology*, 25(2), 275-283.
- Shi, W. T., Forsberg, F., Raichlen, J. S., Needleman, L., & Goldberg, B. B. (1999). Pressure dependence of subharmonic signals from contrast microbubbles. *Ultrasound in Medicine and Biology*, 25(2), 275-283.
- Shi, W. T., Forsberg, F., Tornes, A., Østensen, J., & Goldberg, B. B. (2000). Destruction of contrast microbubbles and the association with inertial cavitation. *Ultrasound in Medicine and Biology*, 26(6), 1009-1019.

- Shung, K. K., Yuan, Y. W., Fei, D. Y., & Tarbell, J. M. (1984). Effect of flow disturbance on ultrasonic backscatter from blood. *Journal of the Acoustical Society of America*, 75(4), 1265-1272.
- Shung K. K., Thieme G. A. (1993). Ultrasonic scattering in biological tissues. Boca Raton: CRC Press.
- Sigel, B., Machi, J., & Beitler, J. C. (1982). Variable ultrasound echogenicity in flowing blood. *Science*, 218(4579), 1321-1323.
- Simpson, D. H. (2001). Detecting and imaging microbubble contrast agent with ultrasound, PhD thesis, University of Toronto, Toronto, Canada.
- Skalak, T. C. (2005). Angiogenesis and microvascular remodelling: A brief history and future roadmap. *Microcirculation*, 12(1), 47-58.
- Skalak, T. C. (2005). Angiogenesis and microvascular remodelling: A brief history and future roadmap. *Microcirculation*, 12(1), 47-58.
- Soetanto, K., & Chan, M. (2000). Fundamental studies on contrast images from different-sized microbubbles: Analytical and experimental studies. *Ultrasound in Medicine and Biology*, 26(1), 81-91.
- Sokolov, S. J. (1935). Ultrasonic oscillations and their applications. *Tech Phys USSR*, 2, 522-534.

- Strasberg, M. (1956). Gas bubbles as sources of sound in liquids. *J. Acoust. Soc. Am.*, 28(1), 20-26.
- Stride, E., & Saffari, N. (2005). Investigating the significance of multiple scattering in ultrasound contrast agent particle populations. *IEEE Transactions on Ultrasonics, Ferroelectrics, and Frequency Control*, 52(12), 2332-2345.
- Szabo, T. L. (2004). *Diagnostic ultrasound imaging: Inside out*. Boston: Elsevier/Academic Press.
- Szabo, T. L. (2004). *Diagnostic ultrasound imaging: Inside out*. Boston: Elsevier/Academic Press.
- Uhlendorf, V. (1994). Physics of ultrasound contrast imaging: Scattering in the linear range. *IEEE Transactions on Ultrasonics, Ferroelectrics, and Frequency Control*, 41(1), 70-79.
- Uhlendorf, V. (1994). Physics of ultrasound contrast imaging: Scattering in the linear range. *IEEE Transactions on Ultrasonics, Ferroelectrics, and Frequency Control*, 41(1), 70-79.
- Vaughan, P. W., & Leeman, S. (1986). Some comments on mechanisms of sonoluminescence. *Acustica*, 59(4), 279-281.

- Vos, H. J., Frijlink, M. E., Droog, E., Goertz, D. E. et al. (2004). A 20-40 MHz ultrasound transducer for intravascular harmonic imaging. *Ultrasonics Symposium, IEEE*, 3 1966-1969.
- Walton, A. J., & Reynolds, G. T. (1984). SONOLUMINESCENCE. *Advances in Physics*, 33(6), 595-660.
- Wang, S. H., Lin, Y. H., & Shung, K. K. (1997). In vivo measurements of ultrasonic backscatter from blood., *Proceedings of the IEEE Ultrasonics Symposium*, 2, 1161-1164.
- Wheatley, M. A., Forsberg, F., Oum, K., Ro, R., & El-Sherif, D. (2006). Comparison of in vitro and in vivo acoustic response of a novel 50:50 PLGA contrast agent. *Ultrasonics*, 44(4), 360-367.
- Yock, P. G., Linker, D. T., & Angelsen, B. A. (1989). Two-dimensional intravascular ultrasound: Technical development and initial clinical experience. *Journal of the American Society of Echocardiography : Official Publication of the American Society of Echocardiography*, 2(4), 296-304.